A search for the electric dipole moment of the electron using thorium monoxide

A Dissertation
Presented to the Faculty of the Graduate School
of
Yale University
in Candidacy for the Degree of
Doctor of Philosophy

by
Amar Chandra Vutha

Dissertation Director: David DeMille

December 2011

Contents

List of Figures

List of Tables

Acknowledgments

I have been fortunate to work with, and learn from, many colleagues and collaborators over the years. I thank them for all the good times. In the end, physics is a human endeavor, whatever it is. I would like to express my deep gratitude to the people who made it fun:

Dave DeMille, mentor, friend and more, who opened my eyes to a world full of wonders.

Jessie Petricka, David Glenn and Paul Hamilton, who tolerated my bumbling startup transients, endured many stupid questions and shared their wisdom freely.

Atomz & Edmz. You all made it interesting.

Jan Ragusa and Daphne Klemme, for making the transitions between New Haven and Cambridge easy.

Dave Johnson, Stan Cotreau, Steve Sansone and Jim MacArthur, who taught me much and built many things to drive the rods that turned the knobs that worked the thingummybobs.

The Goons and other goons, for all the occasions of insanity that stopped me from going mad.

Various Kanpuriyas, ADN, D_H and CS, freonds who made the journey meaningful. "For the best that we find in our travels is an honest friend, and he is a fortunate voyager who finds many." This is for you.

Abstract

A search for the electric dipole moment of the electron using thorium monoxide

Amar Chandra Vutha

2011

This thesis is concerned with the conception, design and construction of an experiment to search for the permanent electric dipole moment of the electron (d_e) with improved sensitivity. This dipole moment, d_e, is a hypothesized quantity whose detection, or (in the absence of detection) an improved constraint on its size, would shed some light on the part played by discrete symmetries of space-time in the evolution of our universe. A non-zero d_e is evidence of parity and time-reversal violation in fundamental physical processes, and provides an experimental test of many proposed extensions to the Standard Model of particle physics. The experiment takes advantage of the enhanced sensitivity of the H state in the thorium monoxide (ThO) molecule to d_e. The precession of the spins of the valence electrons in the internal electric field of the molecule is measured using a molecular beam apparatus. This experiment has the potential to improve the experimental limit on d_e to $\sim 10^{-30}$ e cm, an improvement by a factor of 10^3 over the current experimental limit. I will describe the analysis that led to the identification of ThO as a favorable system for such an experiment, details of the design and construction of the experimental apparatus, and measurements of various properties of ThO which guide estimates of the statistical sensitivity and the size of potential systematic errors in the experiment. A method of analysis of geometric phase effects in terms of off-resonant energy level shifts, which was developed in order to understand potential systematic errors in this experiment, is also described.

Chapter 1

Introduction

T-violation, electric dipole moments and ThO

> We have sailed many weeks, we have sailed many days,
> (Seven days to the week I allow),
> But a Snark, on the which we might lovingly gaze,
> We have never beheld till now !
>
> The Bellman's Speech, *The Hunting of the Snark*

The universe, thankfully, provides a constant source of mysteries to keep us entertained and bewildered. At the present time, despite the success of the Standard Models of particle physics and cosmology, there are huge and humbling gaps in our understanding of the way our universe works. The nature of dark energy and dark matter, which together make up 96% of stuff in the universe, remains a complete mystery. Yet there is a perplexing puzzle even within the 4% of the universe that we do claim to understand. This is the puzzle about where all the anti-matter has gone, for we know that equal amounts of matter and anti-matter were initially created out of energy after the Big Bang, but anti-matter in any substantial quantity does not seem to be naturally present anywhere in the universe [DK03]. One plausible solution to this puzzle invokes T-violation[1] in physics in the early phase of the universe, the idea being that certain processes that turn anti-matter into matter occurred at very slightly faster rates compared to the reverse processes that turn matter into anti-matter [Sak67]. But this solution does not quite work, because the known level of T-violation in particle physics is insufficient to explain the observed size of the

[1] The discrete symmetry operation T maps a process into its motion-reversed version. See [Sak64, Sak85] for discussions of the action of the discrete symmetry operators P and T.

asymmetry between matter and anti-matter [GHO+94]. This leads us to believe that other sources of T-violation exist out there, in physics that is unknown as of now. It is in the search for such new sources of T-violation that the permanent electric dipole moment of the electron might play a part [FSB03].

In any quantum mechanical system in an eigenstate of angular momentum, a permanent electric dipole moment (EDM) can only exist if T is violated (along with parity P).[2] Therefore the discovery of an EDM, or an improved experimental limit on its size, provides information about new sources of T-violation. In 1950, Purcell and Ramsey [PR50] pointed out that the question of the existence of permanent electric dipole moments of fundamental particles could only be decided experimentally, rather than by appealing to aesthetic notions of symmetry. Since then, EDMs of the neutron, the electron, the muon and the proton have been the focus of ever more sensitive searches,[3] although no EDM has ever been detected. The present limit on the neutron's EDM is one of the important elements of the puzzle known as the strong CP problem in the Standard Model. The limit on the EDM of the electron (eEDM) has already excluded a significant section of the parameter space of supersymmetry [OPRS05], a theoretical extension to the Standard Model that is often believed to be true.

The plausible existence of more than one Higgs doublet, or the postulated existence of a multitude of supersymmetric particles [OPRS05, GR06], would each make a number of new T-violating phases available, which could then result in T-violation in the lepton sector of the Standard Model. T-violation within the framework of the Standard Model (a consequence of flavor mixing in the quark sector) has been observed in the decays of K0 and B0 mesons [YoPDG06], but the observed amount has been found inadequate to explain the observed matter-antimatter asymmetry [GHO+94]. If the additional T-violation required to explain matter-antimatter asymmetry is present in the lepton sector, it is expected to show up as an observable eEDM. Electro-weak baryogenesis (EWBG) is one of the most plausible models for generating the cosmological matter-antimatter asymmetry. The limit on the EDMs of the Tl atom and the neutron set the most stringent constraints on the parameter space of EWBG. It is expected that a null result from an eEDM search, with a limit that is lower than the current experimental limit ($d_e \leq 10^{-27} e$ cm) by 2 orders of

[2] See Section A.1 for a discussion of this property.

[3] EDMs are usually introduced as postulated properties of elementary particles, but they can also arise through P and T violating interactions between the constituents of a composite system, like an atom or a nucleus.

magnitude, would constrain the parameter space of EWBG severely enough to render this model implausible [PR09]. Achieving a sensitivity that can rule out EWBG is, arguably, the most concrete goal of any improved eEDM experiment.

1.1 eEDM experiments with atoms and molecules

A considerable body of literature exists concerning the measurement of nuclear EDMs using free neutrons or diamagnetic atoms and molecules, as well as concerning efforts to measure the EDM of the muon. A comprehensive review of EDM efforts can be found in the books by Khriplovich and Lamoreaux [KL97] and Roberts and Marciano [RM09]. Here I discuss eEDM measurements using atoms and molecules.

The relativistic Hamiltonian for the interaction of the EDMs of electrons in an atom or molecule with electric fields is

$$H_{EDM} = -\sum_i d_e \, \beta \, \vec{\Sigma}_i \cdot \vec{\mathcal{E}}_i \tag{1.1}$$

where $\beta = \begin{pmatrix} \mathbf{1} & 0 \\ 0 & -\mathbf{1} \end{pmatrix}$ is a 4x4 Dirac matrix,[4] $\vec{\Sigma} = \begin{pmatrix} \vec{\sigma} & 0 \\ 0 & \vec{\sigma} \end{pmatrix}$ and $\vec{\sigma}$ is the Pauli spin vector [Sal58]. The summation is carried out over the electrons in the system. The ith electron has a spin vector $\vec{\Sigma}_i$, and $\vec{\mathcal{E}}_i$ is the total electric field acting on it. Close to the nucleus, $\vec{\mathcal{E}}_i$ is dominated by the electric field from the the nucleus, so here

$$\vec{\mathcal{E}}_i \approx \Big(\frac{1}{4\pi\epsilon_0}\Big)\frac{Ze\vec{r}_i}{r_i^2}. \tag{1.2}$$

In a non-relativistic system consisting of point particles held together by electrostatic forces, the expectation value of H_{EDM} is always zero – this is the content of Schiff's theorem [PR50, Sch63]. It was pointed out by Salpeter [Sal58] that in atomic states where the electrons approach the nucleus closely enough to experience relativistic effects, H_{EDM} can have a non-zero expectation value. Sandars [San65, San66, San67, San68a, San68b] pointed out that it can also become much larger than $\sim d_e\mathcal{E}_{lab}$ in appropriately chosen situations. The expectation value of H_{EDM} in a state of an atom, with a four-component wavefunction $|\psi\rangle$ and an angu-

[4] $\mathbf{1}$ denotes the 2x2 identity matrix.

lar momentum J, can be parametrized as[5]

$$\langle\psi|H_{EDM}|\psi\rangle \equiv -d_e\langle\psi|\vec{J}|\psi\rangle \cdot \vec{\mathcal{E}}_{atom}. \tag{1.3}$$

The quantity $\vec{\mathcal{E}}_{atom}$ is the "internal electric field" in the atom. Its direction is parallel to $\vec{\mathcal{E}}_{lab}$, and its magnitude depends on the degree of polarization of the atom in the electric field $\vec{\mathcal{E}}_{lab}$ [KL97]. Its magnitude also depends on the amplitude of the wavefunction of the electrons in the state $|\psi\rangle$ at the nucleus, which is where the electrons are accelerated to relativistic speeds and the Sandars effect is most pronounced. This in turn leads to the effect being strongest for electrons in s orbitals, and a scaling of $\mathcal{E}_{atom}$ with the atomic number Z as $\sim Z^3$ [San68b, KL97].

The polarizability of an atom is $\sim \frac{1}{4\pi\epsilon_0}a_0^3$ [Pur84].[6] Even in the largest lab fields therefore, the polarization of the atom (and the internal electric field $\mathcal{E}_{atom}$) are linear in the polarizing electric field $\vec{\mathcal{E}}_{lab}$. In atoms, therefore, (1.3) can be alternatively parametrized as

$$\langle\psi|H_{EDM}|\psi\rangle \equiv -\vec{D}_a \cdot \vec{\mathcal{E}}_{lab} \equiv -Rd_e\frac{\vec{J}}{|J|} \cdot \vec{\mathcal{E}}_{lab}, \tag{1.4}$$

in terms of the permanent atomic EDM D_a induced by the eEDM, or in terms of the "enhancement factor" $R = D_a/d_e$. This parametrization is commonly used in the literature on atom-based eEDM experiments. The enhancement factor is obtained by relativistic atomic structure calculations, and has been tabulated for the alkali atoms (Li, Na, K, Rb, Cs, Fr) and other paramagnetic atoms of interest (Tl, Gd, metastable Xe) [CD09]. Following the suggestion by Sandars, a number of experiments improved the bounds on the size of the eEDM using atomic beam spectroscopy. A recent example is the experiment with an atomic beam of thallium that obtained a limit $|d_e| \leq 1.6 \times 10^{-27}$ e cm [RCSD02]. Ongoing experiments with atoms include those using Cs and Rb trapped in an optical lattice [WFC03], and experiments with bulk solid-state samples containing rare-earth atoms such as Gd,Eu [Lam02, BDS02].

Polar diatomic molecules can be polarized more easily than atoms. The reason for this can be understood in terms of a simple picture. Consider a polar molecule such

[5]Unless explicitly mentioned, we will use units where $\hbar = 1$ everywhere in this thesis.

[6]States of opposite parity are spaced apart by $\Delta \sim 2\pi\times$ 100s of THz in energy, and typical dipole matrix elements between atomic states are $D \sim ea_0 = 2\pi\times$ 1 MHz/(V/cm). From the discussion in Section A.2, it can be seen that even for the largest electric field strengths achievable in the lab ($\mathcal{E}_{lab} \sim 50$ kV/cm), typical atomic states are only weakly polarized.

as thorium monoxide (ThO), where the heavy Th^{2+} ion is bound to the O^{2-} oxide ion, and consider the situation in the molecule-fixed frame where the atomic cores are not rotating about their center of mass. The presence of $\sim 2e$ units of charge, located only a small distance $\sim a_0$ away on the O^{2-} ion, leads to an electric field $\mathcal{E}_{mol} \sim (1/4\pi\epsilon_0)\ 2e/a_0^2 \sim 10$ GV/cm that polarizes the Th^{2+} ion. In the lab frame, where the whole collection of particles – atomic nuclei, core electrons and valence electrons – is in an eigenstate of the total angular momentum, the polarization of the Th atom by the O atom averages out and the expectation value of the static polarization vanishes. When a lab field $\vec{\mathcal{E}}_{lab}$ is applied, energy eigenstates of the molecule have polarization oriented along/against $\vec{\mathcal{E}}_{lab}$. When this happens, the polarization of the Th atom that existed in the molecule-fixed frame (or some fraction of it, depending on how strongly the molecule is oriented) gets oriented along/against the lab electric field too. The only function of the lab electric field is to orient the molecule-fixed dipole, while the strong electric interaction between the two ions takes care of polarizing the Th atom.

More formally, the large polarizability can be understood as arising from the presence of closely spaced states of opposite parity in polar molecules – states of opposite parity can be spaced by $\sim 2\pi\times$ 10s of GHz (rotational states) or even as low as $\sim 2\pi\times$ 10s of kHz (Ω-doublets[7]) – even though the dipole matrix elements between these states are still on the order of an atomic unit, $D \sim ea_0$. The larger polarization in a lab scale electric field leads to a larger internal electric field. It also means that $\vec{\mathcal{E}}_{mol}$, the analog of $\vec{\mathcal{E}}_{atom}$ for a molecule, is no longer linearly proportional to the lab electric field $\vec{\mathcal{E}}_{lab}$ when the molecule is strongly polarized. Therefore the parametrization in terms of the enhancement factor R is insufficient, and we describe the enhancement due to the Sandars effect in terms of the internal field.

In heavy molecules, where the relativistic effects that lead to large internal electric fields are important, spin-orbit effects (which also arise due to relativity) tightly couple the spin $\vec{S}$ of the valence electrons with their orbital angular momentum $\vec{L}$ to form the total electronic angular momentum $\vec{J}_e = \vec{L} + \vec{S}$. Hence in such a system, the eEDM $\vec{d}_e$ lies along $\vec{J}_e$ on average. The total angular momentum of the molecule $\vec{J} = \vec{J}_e + \vec{R}$ is the sum of the electronic angular momentum $\vec{J}_e$ and the nuclear rotation $\vec{R}$. Electronic states in a molecule that are described by Hund's case (c)[8]

[7]See Section A.4 for a brief introduction to Ω-doublets, and references.

[8]The various Hund's cases are a collection of angular momentum coupling schemes, analogous to the jj-coupling and LS-coupling schemes in atoms. Different Hund's cases correspond to different "good" quantum numbers. See [SZ74, Hou01, BC03] for a discussion of Hund's cases in molecules.

are eigenstates of the operator $\hat{\Omega}$, which is the projection of $\vec{J_e}$ onto the internuclear axis of the molecule, $\hat{n}$.

$$\hat{\Omega} \equiv \vec{J_e} \cdot \hat{n}. \tag{1.5}$$

In the lab frame the expectation value $\langle\psi|\hat{\Omega}|\psi\rangle = 0$ in any eigenstate of the parity inversion operator or the squared total angular momentum J^2.

In a molecular state described by a 4-component relativistic wavefunction $|\psi\rangle$, the expectation value of the relativistic eEDM Hamiltonian H_{EDM} is parametrized in the following form [MBD06], in analogy with (1.3):

$$\langle\psi|H_{EDM}|\psi\rangle \equiv -d_e\langle\psi|\vec{J_e}|\psi\rangle \cdot \vec{\mathcal{E}}_{mol} = -d_e\mathcal{E}_{mol}\ \Omega. \tag{1.6}$$

Here $\Omega = \langle\psi|\hat{\Omega}|\psi\rangle$ is determined by the extent to which the state $|\psi\rangle$ is polarized by the lab electric field $\vec{\mathcal{E}}_{lab}$. The internal electric field $\vec{\mathcal{E}}_{mol} = \hat{n}\mathcal{E}_{mol}$ is directed along the internuclear axis of the molecule.[9] $\mathcal{E}_{mol}$ is a property of a specific molecular state, and is calculated using relativistic atomic and molecular theory [Nat09, Mey10]. However, some heuristics have been developed for guessing at whether a given molecular state might have a large value of $\mathcal{E}_{mol}$ [MBD06]. In particular, it is essential that at least one of the valence electrons in the molecule should inhabit a σ molecular orbital derived from an s atomic orbital on the heavy atom in the molecule, in order to obtain the relativistic Sandars effect [KL97, CJD07, CD09]. YbF, a polar molecule with an unpaired valence electron, has been the focus of molecular beam experiments to measure the eEDM [KE94, HKS$^+$11], leading up to a recent improvement of the limit on the eEDM to $d_e \leq 1 \times 10^{-27}$ e cm. Polar molecules are also the ingredients of the

[9] There are a few different versions of this internal electric field used in the literature. It is also referred to as the effective electric field. A summary of these different versions is included here for reference:
The quantity W_d is defined in [CD09, KD02] as:

$$W_d \equiv \frac{\langle\psi|H_{EDM}|\psi\rangle}{d_e\Omega}. \tag{1.7}$$

The effective electric field $\mathcal{E}_{\text{eff}}$ is defined in [CD09] as:

$$\mathcal{E}_{\text{eff}} \equiv W_d\Omega = \frac{\langle\psi|H_{EDM}|\psi\rangle}{d_e}. \tag{1.8}$$

This differs by a minus sign from F_{eff} defined in [MBD06]:

$$F_{\text{eff}} \equiv -W_d\Omega = -\frac{\langle\psi|H_{EDM}|\psi\rangle}{d_e}. \tag{1.9}$$

PbO experiment at Yale, which has a projected sensitivity of $\sim 10^{-28}$ e cm [DBB$^+$00, KBB$^+$04, Ham10]. Other eEDM experiments currently using polar molecules are the HfF+/ThF+ [LBL$^+$10], WC [LMP$^+$09] and PbF [SR06] experiments.

1.1.1 Measuring the eEDM-induced energy shift in a molecule

Consider a pair of states in a molecule, $|a\rangle$ and $|b\rangle$, wherein the expectation value of $\hat{\Omega}$ is oppositely directed and has a magnitude Ω_0:

$$\langle a|\hat{\Omega}|a\rangle = -\langle b|\hat{\Omega}|b\rangle = \Omega_0. \tag{1.10}$$

As mentioned above, $\Omega_0 = 0$ if $|a\rangle, |b\rangle$ are eigenstates of parity. However, if these are states in a molecule that has been polarized by an external electric field, then Ω_0 can be non-zero. The energy difference between these states due to an eEDM can be calculated using (1.6). It corresponds to an angular frequency ω_{EDM} given by

$$\omega_{EDM} = 2\ d_e \mathcal{E}_{mol} \Omega_0. \tag{1.11}$$

This frequency can be measured experimentally, and constitutes the basic signal of any eEDM experiment with a polar molecule. For a given signal-to-noise ratio SNR, the fundamental limit to the statistical uncertainty of the measurement of ω_{EDM} is given by

$$\delta\omega \ = \ \frac{1/\tau}{\mathrm{SNR}}. \tag{1.12}$$

Here τ is the coherence time, the duration for which the wavefunctions of the states $|a\rangle$ and $|b\rangle$ evolve in phase. The SNR in turn has a fundamental limit, $\mathrm{SNR} = \sqrt{N}$ for measurements made on an ensemble of N independent molecules.[10] Using (1.6), the uncertainty in the measurement of ω, $\delta\omega$, can be related to the uncertainty in the eEDM, δd_e:

$$\delta d_e \ = \ \frac{1/\tau}{2\mathcal{E}_{mol}\Omega_0\ \sqrt{N}}. \tag{1.13}$$

δd_e is the principal figure of merit for the statistical sensitivity of any eEDM experiment.

[10] This dependence on N is derived in Section 2.3.1 after the measurement scheme has been discussed.

1.1.2 The choice of ThO for an eEDM experiment

The primary goal of the work presented in this thesis was to design an experiment that could improve the limit on the eEDM by a significant factor compared to the above experimental approaches. Initially, the work was aimed at improving the design of the PbO experiment. However, around that time, important advances in the techniques of generating intense cold molecular beams were made at Harvard in the Doyle group [PD07]. In this approach, molecules in the gas phase are produced by pulsed laser ablation of a solid precursor target, inside a copper cell cooled to 4 K that contains a buffer gas of helium. Collisions with helium gas cool the hot molecules produced in ablation. An aperture in the side of the cell causes hydrodynamic flow of helium gas out of the cell and into the molecular beam region. This hydrodynamic flow can efficiently entrain most of the cold molecules produced inside the cell and extract them out into a molecular beam. But to take advantage of the high phase space density available using buffer gas cooled beams, a molecule with a long-lived EDM-sensitive state is required, sufficiently long that time of flight-limited spin precession can be observed in a ~ 30 cm scale molecular beam apparatus.[11] With typical forward velocities of about 200 m/s obtained with hydrodynamically extracted buffer gas cooled beams, this translates to a state lifetime that has to be comparable to $\sim$ 2 ms. PbO was therefore not a viable candidate as its EDM-sensitive $a(1)$ state has a lifetime that is ~ 80 μs, and a new molecule was sought that was best suited to a molecular beam eEDM experiment with a buffer gas cooled beam.

First, here is a wish-list of the desirable features of an eEDM-sensitive molecule.

$\mathcal{E}_{mol}$ scales as Z^3 with the atomic number Z of the positive ion in the molecule, so the positive ion in the molecule has to be derived from a heavy relativistic atom in order to obtain the eEDM enhancement. Further, as mentioned above, the molecular orbital of the positive ion that contributes to the eEDM enhancement has to be derived from an atomic s orbital. Atomic s orbitals, when strongly mixed with p states by the electric field from the negative ion, are mapped onto σ molecular orbitals. A valence ns σ orbital is a necessary feature of an eEDM-sensitive molecular state.

Electronic states in a Hund's case (c) diatomic molecule with $\Omega \geq 1$ have closely spaced levels of opposite parity (Ω-doublets), often separated in energy by < 1 MHz, which can be polarized in laboratory electric fields $\lesssim 10$ V/cm. A simple picture of

[11] This length scale is set by mundane/real-world constraints, such as the length of the region where a uniform $\mathcal{E}$-field can be obtained, the volume that can be magnetically shielded, etc.

these doublet states is provided in Section A.4, and more detailed calculations can be found in [LL81, BC03]. As these levels can be very easily polarized, a molecule with Ω-doubling in the eEDM-sensitive state is desirable for taking full advantage of $\mathcal{E}_{mol}$.

The spin coherence time τ is ultimately limited by the radiative lifetime of the state in which the measurement is performed. Therefore one of the constraints is that the molecular state that is used be sufficiently long-lived. The coherence time has some effect on the choice of the measurement scheme. For example, molecular states with a value of τ in the range of 10 ms-1 s are well-suited for experiments with trapped molecules/molecular ions, where the technical limit to the achievable coherence time is on the order of a few seconds. Molecular beam experiments, where the technical limit on the coherence time is set by the time of flight of molecules through a reasonably-sized apparatus, are best suited to states with coherence times in the range of 100 μs to 10 ms (with some dependence on the choice of beam source).[12]

The number of molecules interrogated during the measurement, N, can be written as $N = \dot{N}T$, where $\dot{N}$ is the count rate and T is the integration time of the experiment. Choosing a molecular species that can be produced in numbers large enough to yield good SNR is an important requirement, as is ensuring that the interrogation technique samples a large fraction of the molecules that are produced.

However, statistical sensitivity is not the only relevant metric. The measurement scheme, details of the way the apparatus is constructed and the choice of atomic/molecular system will also affect the ability of the experiment to reject sources of systematic errors. It can be argued that the main purpose of having a high statistical sensitivity in the eEDM experiment is to allow the characterization and testing of potential systematics without requiring an unduly long integration time. The potential systematics will be examined in detail in Chapter 3, but as far as the choice of molecule is concerned, the following features are desirable:

- **Ω-doublets**: The first advantage of a molecule with Ω-doublets is due to their large electric polarizability. In addition to enhancing the effect of an electron EDM, a large polarizability (especially if the induced dipole moment is saturated) ensures that the internal electric field experienced by the electron is immune to fluctuations in the magnitude of the lab electric field. Many

[12] A longer time (e.g. use of a ground state) does not hurt, but these shorter times are not a real disadvantage when working with beams.

systematic effects, on the other hand, should scale in some way with the lab $\mathcal{E}$-field. Third, a large tensor Stark shift[13] in the EDM sensitive state ensures that the effect of motional magnetic ($\vec{v} \times \vec{\mathcal{E}}/c^2$) and motional electric fields ($\vec{v} \times \vec{\mathcal{B}}$), which are transverse to the main $\vec{\mathcal{E}}, \vec{\mathcal{B}}$ lab fields, is suppressed [PS70]. The existence of a tensor Stark shift does not require Ω-doubling, but Ω-doubling results in a large tensor Stark shift being obtained with modest electric fields. Fourth, a large polarizability implies the use of small electric fields applied in the lab, which further mitigates the effect of $\vec{\mathcal{E}}$-correlated magnetic fields produced by leakage currents.

The principal advantage of Ω-doublets for systematic error rejection arises from the fact that the eEDM-induced energy shift in the molecule, $\propto \mathcal{E}_{mol}\Omega$, can be reversed by making the measurement using pairs of states in different components of the doublet. This is explained in detail in Section 2.2.1. This feature allows the eEDM-induced energy shift to be reversed purely spectroscopically, without reversing any laboratory $\vec{\mathcal{E}}, \vec{\mathcal{B}}$ fields. Thus it provides a powerful filter for systematic effects. Such a comparison between the components of an Ω-doublet also turns out to be capable of rejecting systematic errors from troublesome geometric phases, as shown in Section B.8. So far, this is the only method known to us that can reliably reject systematic errors picked up due to geometric phases.

The requirement that the molecule have both Ω-doublets (which require non-zero orbital angular momentum about the internuclear axis) and s-derived σ orbitals (to obtain relativistic enhancement) naturally leads to the choice of a molecular state that has 2 valence electrons occupying $\sigma\sigma^*$ (or $\sigma\pi, \sigma\delta, ...$)-type molecular orbitals arising from the corresponding s^2 (or $sp, sd, ...$)-orbitals of the heavy atom. One of the valence electrons undergoes the relativistic eEDM enhancement, while the other valence electron orbits far away from the nucleus and leads to the Ω-doubling/polarizability of the molecule. Finally, these two electrons need their spins to be in a triplet state so that the state as a whole has a non-zero electronic spin (and therefore a non-zero eEDM).

[13] Any system with $J \geq 1$ exhibits a tensor Stark shift, where the energy shift of a state $|J, m_J\rangle$ in an electric field $\mathcal{E}$ is

$$W(m_J) = -\frac{1}{2}\alpha_t \frac{3m_J^2 - J(J+1)}{J(2J-1)}\mathcal{E}^2 + \mathcal{O}(\mathcal{E}^4). \tag{1.14}$$

Here α_t is referred to as the *tensor polarizability*.

- $^3\Delta_1$ **electronic state**: In addition to closely spaced Ω-doublets, a molecule in a $^3\Delta_1$ electronic state has a very small magnetic moment [Cra34]. In a $^3\Delta_1$ state, the spin and orbital angular momentum projections on the internuclear axis point in opposite directions, resulting in a net angular momentum projection of $1\hbar$. But as the electron's spin gyromagnetic ratio is twice as large as the orbital gyromagnetic ratio, the magnetic moments of the spin and orbital degrees of freedom cancel each other out to a large extent. Such a state has the advantage of suppressing systematic errors due to residual $\mathcal{B}$-fields. The effects of Johnson magnetic noise from nearby conductors are also suppressed, which is advantageous for obtaining a small statistical uncertainty in the measurement. The advantages of $^3\Delta_1$ states for eEDM experiments were first explained in [MBD06].

- **Convenient optical transitions**: As will be described in Chapter 2, all the mechanics of populating an eEDM-sensitive state, spin preparation, detection by laser-induced fluorescence etc. involve lasers tuned to various optical transitions in the molecule. Hence a molecule which has transitions that permit these tasks (for example, by providing favorable pathways for one-way state transfer, spin-orbit-mixed intermediate states that allow singlet-triplet coupling, etc.), and has them at wavelengths that are accessible using easily available laser sources, is greatly desirable. This might appear to be entirely motivated by cost or experimental ease, but the choice of laser wavelengths can have important effects on the duty cycle of the experiment. Therefore, one of the factors influencing the choice of a molecule was the availability of diode lasers at the wavelengths of all the relevant transitions.

To summarize, a suitable molecule for the experiment was required to have the following properties:

- $^3\Delta_1$ molecular state, derived from *sd* orbitals of the heavy atom.

- Large atomic number Z of the heavy atom, to obtain relativistic enhancement of the eEDM.

- Ground, or long-lived metastable, $^3\Delta_1$ state to ensure a coherence time $\tau \gtrsim 2$ ms.

- Laser diode accessible optical transitions, with convenient state preparation and detection transitions.

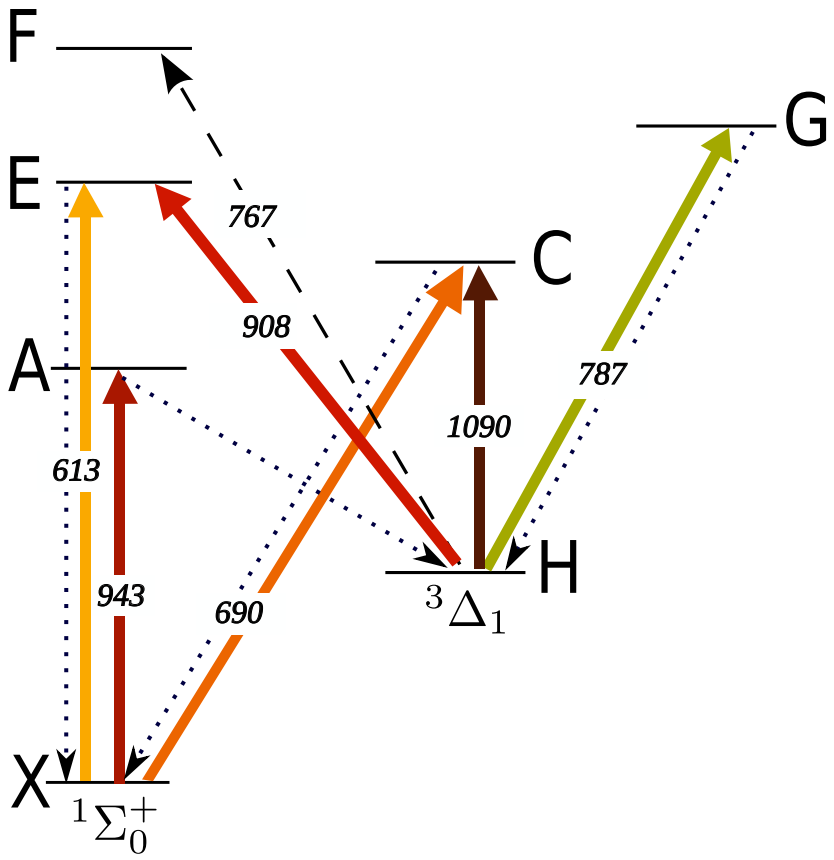

Figure 1.1: Electronic states in the ThO molecule, shown schematically (based on [EL84]). The metastable H $^3\Delta_1$ state is the one in which the valence electrons experience a strong EDM-enhancing internal field $\mathcal{E}_{mol}$. Bold arrows indicate transitions that have been observed using laser absorption or used to induce fluorescence. Dotted lines indicate transitions where spontaneous decay has been detected by laser-induced fluorescence or inferred from optical pumping effects. Numbers on the arrows indicate their wavelengths in nm.

- Amenable to production in large numbers in a buffer gas cooled-beam, from a solid/stable precursor.

The starting point of the search for a candidate molecule was the observation that TiO has a $^3\Delta_1$ ground state (although Z(Ti) is too small to be useful). Therefore, molecules iso-electronic with TiO were examined systematically and the choice was narrowed down to the following: ZrO, YF, ScF, HfO, LaF, ThO. All of these have either ground or low-lying metastable $^3\Delta_1$ states. Of these, the latter three are the only ones with large enough Z to obtain a significant relativistic enhancement. Further, LaF was ruled out because the dominant stable isotope (^{139}La, 99.9%) has a large nuclear spin ($I = 7/2$), which would significantly dilute the available

population of molecules. Of the remaining two, HfO has the disadvantages that the principal strong transition for monitoring the ground state lies at the inconvenient (for diode lasers) wavelength of 613 nm ($X\ ^1\Sigma \rightarrow b\ ^3\Pi_0^+$), and the guesstimated radiative lifetime of the metastable $a\ ^3\Delta_1$ state is < 1 ms, too short to provide a useful coherence time. Fortunately, ThO has *all* the above desired features, in addition to containing the heaviest atom that is (almost) not radioactive.

The structure of the electronic states in ThO is shown in Fig.1.1 [EL84]. The metastable $H\ ^3\Delta_1$ state in ThO arises from an atomic $6d7s$ configuration in the Th atom [MWGP87, KDSP94] and has the expected large relativistic EDM enhancement. The size of the internal field ($\mathcal{E}_{mol} = 104$ GV/cm) has been verified by theoretical calculations [MB08]. Being an $\Omega = 1$ state, the H state also has closely spaced Ω-doublets that can be easily polarized. Radiative decay of the H state to the ground state is suppressed because of their small energy separation (it is only ~ 5300 cm^{-1} above the ground $X\ ^1\Sigma$ state), and because the radiative transition requires a spin flip to go from the paramagnetic H state to the diamagnetic ground state. The measurements described in Section 4.2 indicate that the lifetime of the H state is $\tau_H = 1.8$ ms. The multitude of electronic states with various degrees of spin-orbit mixing means that there are very convenient pathways for one-way optical pumping/coherent state transfer into the H state, and detection of fluorescence from the H state that is blue-shifted compared to the pump laser (a huge convenience for suppressing background from laser light scatter). Further, these transitions are all located at wavelengths accessible using diode lasers (another convenience due to their low cost and easy maintainability). Finally, it is not an insignificant advantage that the spectroscopy of the ThO molecule has been thoroughly studied both theoretically and experimentally, and the constants for the molecular states are known precisely [MWGP87, EL84, GHKH05, WM97, HH79, PNH02].

This thesis is structured as follows. The features of the measurement scheme with the ThO molecule are described in Chapter 2, along with an analysis of the expected statistical sensitivity. Chapter 3 contains some estimates of potential systematic errors that could affect the measurement. Some measurements made on the ThO molecule, which feed into these analyses, are described in Chapter 4. Chapter 5 contains a description of some of the parts and subsystems of the experimental apparatus for the eEDM measurement that I designed and constructed. Appendix A contains some miscellaneous results for reference. Appendix B describes the method of calculating geometric phases in terms of energy shifts, with examples leading up

to the calculation of geometric phases for Ω-doublet states in a polar molecule.

Chapter 2

Overview of the experiment

All my means are sane, my motive and my object mad.

Moby Dick

The various pieces of the experiment, namely the hardware that constitutes the apparatus and the pieces of the measurement scheme, are reviewed in this chapter. After the measurement scheme has been described, the factors that affect the statistical uncertainty of the measurement are discussed, followed by an estimate of the expected statistical sensitivity of the experiment to an eEDM.

2.1 Overview of the apparatus

A schematic of the eEDM apparatus is shown in Figure 2.1. The coordinate system that is used with reference to the experiment is as follows: $\hat{x}$ is the direction of propagation of the molecular beam, and defines the beamline. It is horizontal in the lab. $\hat{y}$ is the vertical direction in the lab. $\hat{z}$ is the direction of the main $\mathcal{E}$ and $\mathcal{B}$-fields in the experiment. It is horizontal in the lab. The parts of the experiment that are shown in the schematic are the following.[1]

[1]People who were involved in developing the various parts of the apparatus are listed here: Beam source (Hutzler, Parsons, Petrik, Vutha, Campbell), Lasers (Gurevich/Spaun/Hess), Laser lock system (Gurevich/Spaun/Hess,Vutha), Magnetic shielding (Vutha, Kirilov), $\mathcal{B}$-field coils (Kirilov, Vutha), Interaction chamber (Vutha, Spaun), $\mathcal{E}$-field assembly (Vutha, Kozyryev), Collection optics (Hutzler, Vutha), Control electronics (Hess/Spaun/Gurevich).

Where this information was available to me, people are listed in decreasing order of involvement (comma-separated list). I apologize for any inadvertent omissions or errors in these credits.

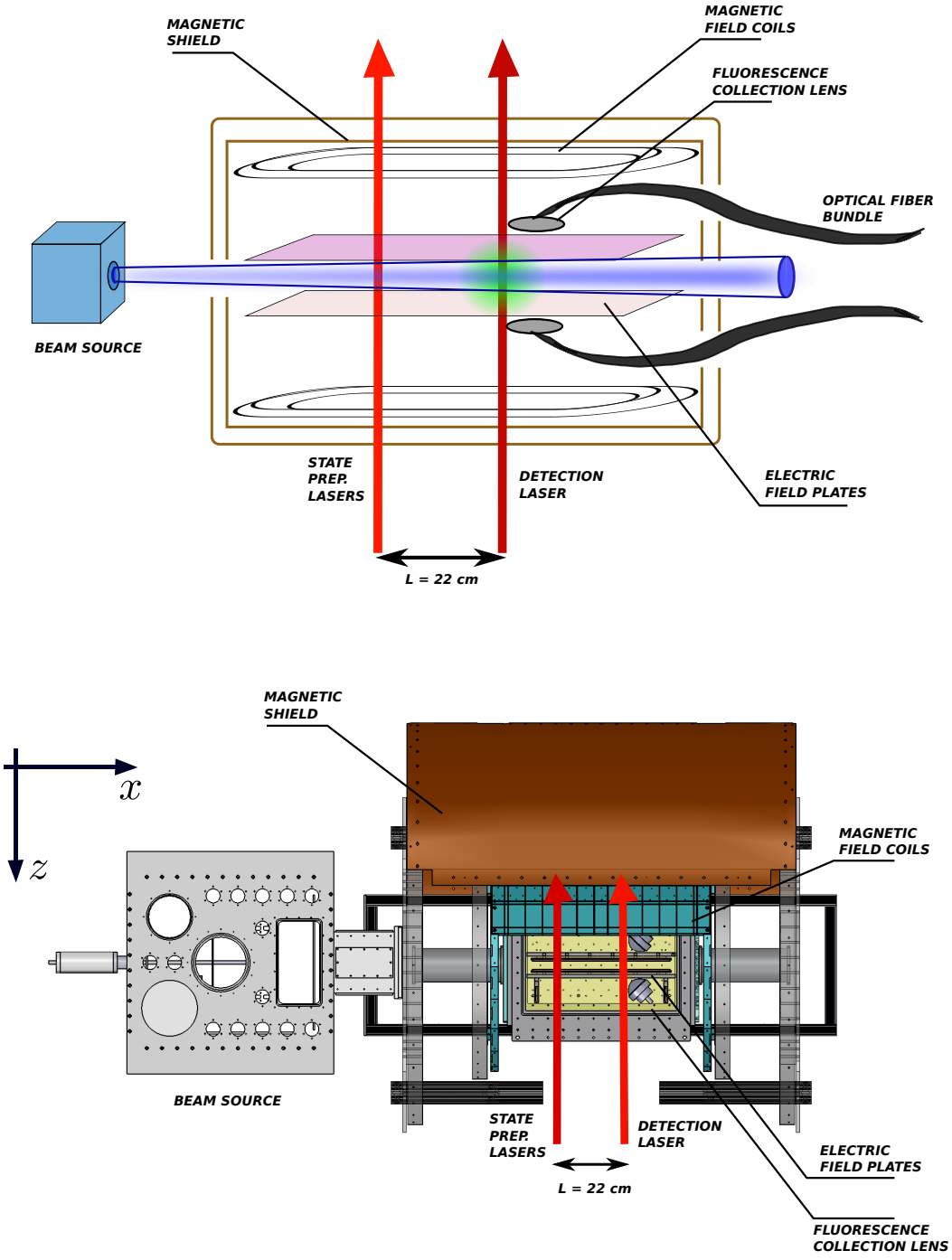

Figure 2.1: Two overviews of the experimental apparatus. The upper view is a schematic, and the lower shows a view of a CAD assembly of the experiment.

- **Beam source**

  In the molecular beam source, ThO molecules are produced by laser ablation of a ThO_2 precursor, using a pulsed Nd:YAG laser at 532 nm. The ThO molecules are thermalized to the temperature of the production cell, which is cooled by a pulse tube refrigerator (PT415, Cryomech), by means of neon buffer gas. A hole in the wall of the cell results in a directed jet of neon gas, which entrains the ThO molecules into its flow as it exits the buffer gas cell. Due to the mismatch in mass between the Ne atoms and ThO molecules, the ThO molecules emerge with a smaller angular divergence compared to the Ne atoms. The beam is skimmed in order to contain within the source chamber those Ne atoms that are outside the solid angle occupied by usable ThO molecules. These Ne atoms are cryo-pumped inside the source chamber. The skimmed beam is collimated and aimed into the interaction region vacuum chamber. This beam source and the characteristics of the molecular beam produced by it are described in detail in [HPG+11].

- **Lasers**

  There are a number of different lasers used in the experiment. These are the $X \rightarrow C$ laser for probing the population in the ground state (690 nm), the $X \rightarrow A$ optical pumping laser (943 nm), the $H \rightarrow C$ laser (1090 nm) for preparing and (possibly for detecting) the spin superposition in the H state, and the $H \rightarrow E$ laser (908 nm) for detecting the state precession. These lasers are commercial or home-built external cavity diode lasers (ECDLs). When more than $\sim$ 100 mW is required out of the diode lasers, they are amplified using either tapered amplifiers or fiber amplifiers. The frequency of these lasers is stabilized by locking them to an optical cavity, which in turn is stabilized using a reference laser (either a He:Ne laser or an I_2-stabilized YAG laser). Multiple lasers are locked to the same cavity, and combined (separated) using off-the-shelf edge-pass optical filters on the input (output) of the cavity. The transmission of each laser through the cavity is separately monitored using amplified photodiodes (PDA-36A, Thorlabs). The output of the photodiodes is digitized with an analog-to-digital converter and the control system for the frequency stabilization is implemented in software.

- **Magnetic shielding**

  Magnetic shielding, in the form of 5 nested mu-metal cylinders, encloses the in-

teraction region. Its purpose is to reduce the influence of low-frequency $\mathcal{B}$-field fluctuations over the volume sampled by the molecules during their precession in the H state. The design and construction of the magnetic shields is described in Chapter 5.

- **$\mathcal{B}$-field coils**
  This is a set of coils wound on a cylindrical form that is 30 in. in diameter and 32 in. long. The coils are enclosed by the magnetic shields. The purpose of the coils is to provide a uniform $\mathcal{B}$-field over the volume sampled by the ThO molecules during their precession. There are 2 main coils and 4 auxiliary shim coils to reduce the fringing of the $\mathcal{B}$-field from the main coils. There are also a set of gradient coils directly mounted onto the interaction vacuum chamber to artificially apply $\mathcal{B}$-field gradients over the measurement volume to check for systematics.

- **Interaction chamber**
  The spin precession measurement is performed on the ThO molecules in this vacuum chamber. As described later in this chapter, lasers are used to pump the molecules into the H state, prepare their spin and measure the angle of spin precession after a free flight path, $L = 22$ cm. The chamber is contained within the magnetic shields and the $\mathcal{B}$-field coil. It encloses the electric field plate assembly and the light collection optics. It is described in Chapter 5.

- **$\mathcal{E}$-field assembly**
  A pair of parallel plates, 9 in. (y) x 17 in. (x) and positioned parallel to the xy-plane, provide a uniform $\hat{z}$-directed $\mathcal{E}$-field over the volume sampled by the molecules during their precession. These plates are made out of borofloat glass, and coated with a transparent conducting indium tin oxide layer on the surfaces facing the molecular beam. They are transparent to allow the optical pumping, state preparation and detection lasers to be sent along the direction of the $\mathcal{E}$-field, and to allow fluorescence from the molecules to be collected at the end of their precession path. They are described in detail in Chapter 5.

- **Collection optics**
  The precession of the spin of the molecules in the H state is detected at the end of their 22 cm long flight path in the interaction region. Laser-induced fluorescence, with an intensity depending on the angle between the molecule's

spin and the laser's polarization, is obtained from the molecules in the H state. The photons emitted by the molecules are the main signal in the experiment. These photons are collected by a set of compound 2 in. lenses located ~ 3 in. away from the molecules. There are 8 such lenses, 4 on either side of the electric field plates. These lenses focus the light into 10 mm diameter optical fiber bundles, which are flexible and can be used to convey the photons from the fluorescence emission region to the downstream end of the interaction vacuum chamber. The fiber bundles then transfer the photons into quartz lightpipes that feed through the vacuum system and penetrate the magnetic shields. Outside the magnetic shields, the photons from the lightpipes are detected by large-area (23.5 mm x 23.5 mm) photomultiplier tubes (R8900-20, Hamamatsu).

2.2 Measurement scheme

We focus on the $H\ ^3\Delta_1$ state in ThO, which has a large eEDM enhancement and is favorable for the reasons explained in the Introduction. ThO molecules in the cold beam source are produced in the $X^1\Sigma^+, v = 0$ state with a rotational temperature of ~ 3 K. At this temperature, 95% of the molecules are produced in states with $J \leq 3$. After leaving the cryogenic beam source, the molecules fly ballistically through the rest of the vacuum apparatus. The molecular beam is collimated before it enters the magnetically shielded interaction region. In this interaction region, the states in the molecule are perturbed by $\mathcal{E}$ and $\mathcal{B}$-fields. So the structure of the relevant molecular states, when they are in the interaction region, is discussed first.

2.2.1 Effect of $\mathcal{E}$ and $\mathcal{B}$ fields on the molecule

The $\mathcal{B}$-field applied over the interaction volume is $\mathcal{B}_z \sim 10$ mG, as will be described later. It only has a weak effect on the states of the molecule, corresponding to a $\sim$ 20 kHz Zeeman shift for typical paramagnetic states in the molecule (with magnetic moment $\sim 1\ \mu_B$) and a ~ 200 Hz Zeeman shift in the magnetically insensitive H state.[2] The $\mathcal{E}$-field that is used during the measurement, $\mathcal{E}_z \sim 100$ V/cm, has a stronger effect on the molecules.

[2]The magnetic moment of the H state is $\mu_H = 8.5(5) \times 10^{-3}\mu_B$. See Chapter 4 for the details of this measurement.

In the absence of an electric field, states in the molecule are eigenstates of the squared angular momentum operator J^2, its projection along the $\hat{z}$-axis in the lab J_z (without loss of generality), and the parity operator P. The eigenvalues of the P operator are $p = \pm 1$. In an $\mathcal{E}$-field, quantum states are no longer eigenstates of J^2 or P, since both inversion symmetry and isotropy are broken by the interaction with the electric field, described by the Hamiltonian $H_{\mathcal{E}} = -\vec{D} \cdot \vec{\mathcal{E}}$. States continue to be eigenstates of J_z, since azimuthal symmetry around the axis of the $\mathcal{E}$-field is maintained.

In a given electronic state in ThO (where all the electronic states can be described in the Hund's case (c) basis), the rovibrational states can be written as

$$|\psi\rangle = |J^p, m_J, \Omega\rangle |\Omega; \Gamma\rangle \tag{2.1}$$

where m_J is the eigenvalue of the J_z operator and Ω is the eigenvalue of the operator $\hat{\Omega} \equiv \vec{J}_e \cdot \hat{n}$ introduced before. The first ket in the product describes the transformation properties of the state under rotations and is described by spherical top functions, while the second ket describes the state in the molecule-fixed frame (see Section A.3 and [Hou01]). Γ is a placeholder for quantum numbers of the state in the molecule-fixed frame, such as the vibrational quantum number v and others.

In electronic states with no Ω-doubling (i.e. $\Omega = 0$ states), such as the X, E, A states, the parity of a rotational state $|J\ m_J\rangle$ is $p = (-1)^J$ (similar to the usual spherical harmonic wavefunctions). Therefore the nearest opposite parity state to a given rotational state is the next rotational state $|J \pm 1\ m_J\rangle$. The typical rotational constant in these electronic levels is $B \sim 2\pi \times 10$ GHz,[3] which means that the energy separating opposite parity states is $\Delta_{pq} \sim (J+2)B$. In comparison, a typical electric dipole matrix element between these states is $D_{pq} \sim 2\pi \times$ 1 MHz/(V/cm), which means that this system is in the weakly polarized regime described by (A.9). The amount of mixing between the wavefunctions of neighboring rotational states in such $\Omega = 0$ electronic states is $\leq 10^{-2}$ (in amplitude) for the electric fields, $\mathcal{E} \approx 100$ V/cm, that are present in the interaction region.

The situation is different in electronic levels that have $\Omega > 0$ (the C, H, G states). As a result of Ω-doubling, opposite parity states can be spaced apart in energy by an amount Δ_{pq} that is small or comparable to $D_{pq}\mathcal{E} \approx 2\pi \times$ 100 MHz. Particularly

[3] The energy of a rotational state $|J\ m_J\ \Omega\rangle$ is $E(J, m_J) = B\ J(J+1)$, where B is the rotational constant of the electronic and vibrational level in which the rotational level is located. Recall that we are using units where $\hbar = 1$.

for the low-lying rotational states in the H and G electronic states,[4] $\Delta_{pq} \ll D_{pq}\mathcal{E}$ and the rotational levels are in the strongly polarized regime described by (A.10).

We restrict our attention now to the $H, v = 0, J = 1$ states, which is where the eEDM measurement sequence occurs. The structure of the $H, v = 0, J = 1$ manifold is shown in Figure 2.2. In the absence of an electric field, the states are well described by the labels $|J^p, m_J\rangle$. The electric field in the interaction region is large enough to strongly polarize the $|1^{\pm}, |m_J| = 1\rangle$ states (via mixing with the $|1^{\mp}, |m_J| = 1\rangle$ states), but only weakly polarizes the $|1^{\pm}, m_J = 0\rangle$ states (via mixing between the distant $|2^{\mp}, m_J = 0\rangle$ states).[5] In the strongly polarized regime, the $m_J = \pm 1$ states are fully mixed with their opposite parity twins; when fully mixed, they become eigenstates of $\hat{\Omega}$ with an eigenvalue $|\Omega| = 1$. Note that these states, with $\langle\psi|\hat{\Omega}|\psi\rangle \neq 0$, are exactly the kind where the eEDM Hamiltonian has a non-zero expectation value. (Recall that $\langle H_{EDM}\rangle \propto \mathcal{E}_{mol}\Omega$.) The $m_J = 0$ states are approximate eigenstates of parity. Therefore the $m_J = 0$ states continue to be described by $|J^p, m_J\rangle$ labels, whereas the $m_J = \pm 1$ states are described by the labels $|J, m_J, \Omega\rangle$ (or equivalently, by the labels $|J, m_J, \mathcal{N} = m_J\Omega\rangle$). For definiteness the $m_J = \pm 1$ states, when strongly mixed by an $\mathcal{E}$-field, will henceforth always be described using the $|J, m_J, \mathcal{N} = m_J\Omega\rangle$ labels.

Also note that labeling these states by the quantum number J is a convenient fiction. In reality, the states in the $J = 1$ manifold are also mixed with opposite parity states in the $J = 2$ manifold by the electric field. This amplitude mixing between $J = 1$ and $J = 2$ states is at the $\sim 10^{-2}$ level, similar to that in $\Omega = 0$ electronic states in the weakly polarized regime. Nevertheless, this can lead to important systematic effects, such as the dependence of the g-factors of the polarized Ω-doublet states linearly on the lab $\mathcal{E}$-field [BHJD09, Ham10]. In the following, we will continue to label states using the quantum number J, with the caveat that in an $\mathcal{E}$-field the states are no longer eigenstates of the squared total angular momentum operator J^2.

The two states with $\mathcal{N} = +1$ are lowered in energy in the $\mathcal{E}$-field. The states with $\mathcal{N} = -1$ are raised in energy. An easy way to remember which way these states are shifted in energy by an $\mathcal{E}$-field is to notice that the expectation value of the dipole

[4] These states correspond to ${}^{2\Sigma+1}\Lambda_\Omega \approx {}^3\Delta_1$ and ${}^3\Phi_2$ configurations in the Hund's case (a) basis respectively. As described in Section A.4, the source of Ω-doubling is the projection of the orbital angular momentum about the internuclear axis, Λ. The H and G states have $\Lambda > 1$ and therefore have a small zero-field Ω-doublet splitting, $\Delta_{pq} \lesssim 2\pi\times$ 1 MHz. The C state is derived from a ${}^1\Pi_1 + {}^3\Pi_1$ configuration (i.e. $\Lambda = 1$) and therefore has a larger Ω-doublet splitting, $\Delta_{pq} \sim 2\pi\times$ 50 MHz.

[5] The mixing between the $|J, m_J = 0\rangle$ states in the same J manifold is parity-allowed, but forbidden due to angular momentum conservation. This can be verified using (A.16) in Section A.3.

moment[6] in these polarized states, $\langle\psi|D|\psi\rangle \propto \langle\psi|\frac{\mathcal{N}}{J(J+1)}|\psi\rangle$.[7] Since the Hamiltonian for the electric dipole interaction is $H_{\mathcal{E}} = -\vec{D}\cdot\vec{\mathcal{E}}$, states which are lowered (raised) in energy correspond to $\mathcal{N} = 1$ ($\mathcal{N} = -1$). The states with $\mathcal{N} = \pm 1$ are shifted in energy from their zero-field positions by an amount that is referred to as the "tensor Stark shift" Δ_{st}. Note that, for the pair of states with a given value of $\mathcal{N}$ (say $\mathcal{N} = +1$), since they have oppositely signed values of m_J they also have oppositely signed values of Ω. Therefore this pair of states is exactly of the form useful for measuring the eEDM as described in (1.11) (with $\Omega_0 = 1$).

2.2.2 State preparation and detection

Now back to the story of the molecules along the beamline. Inside the interaction chamber, in the volume where the $\mathcal{E}$ and $\mathcal{B}$-fields are uniform, the molecules are optically pumped into the H state. This is done by driving the weakly allowed $X^1\Sigma^+, v = 0 \to A^3\Pi_0^+, v = 0$ transition at 943 nm. The A state can spontaneously decay back only to X or into the H state. The Franck-Condon factor for decay from $A, v = 0 \rightsquigarrow H, v = 0$ is 0.98.[8] Thus, optical pumping from $X \to A \rightsquigarrow H$ is a convenient way to obtain almost one-way population transfer into the $H, v = 0$ state. The spontaneous decay from the A state produces a mixed state consisting of the rotational sublevels of $H, J = 1$.[9] For the $\mathcal{E}$-fields used in the experiment, the $A, J = 0^+$ state is well described as a parity eigenstate. The $H, |J^p = 1^-, m_J = 0\rangle$ states are weakly polarized and are approximate eigenstates of parity, as discussed above. In the H state, $|J = 1, m_J = \pm 1\rangle$ are fully polarized. Therefore, spontaneous decay from the $A, J = 0^+$ state mainly populates the states $|1^-, 0\rangle, |1, \pm 1, \mathcal{N} = \pm 1\rangle$ in the $H, v = 0, J = 1$ manifold shown in Figure 2.2. This is the situation by the time the molecules are past the optical pumping laser.

Next, the quantum state used for the measurement of the eEDM is prepared. This state is derived from the $|J, m_J, \mathcal{N}\rangle = |1, \pm 1, \pm 1\rangle$ states. The state of the

[6] This is the induced electric dipole moment $e\vec{r}$, corresponding to the electric polarization of the molecule. It arises due to the spatial displacement of the charges in the molecule. This is not the same as the eEDM, which is related to the spin degree of freedom of the electrons.

[7] This expression can be obtained using (A.16) from the Appendix.

[8] The $A - H$ Franck-Condon factors were not evaluated in [WS72]. This value was calculated using the overlap of simple harmonic oscillator wavefunctions, with the constants in [EL84]. The code used to calculate the $A - H$ Franck-Condon factors was tested against the calculated FCFs for other ThO transitions listed in [WS72].

[9] When the states in the $H, J = 1$ manifold are strongly polarized, the branching probabilities for decay into the final states in the $H, J = 1$ manifold are proportional to the following: $|J = 1^-, m_J = 0\rangle \equiv 1/3$, $|J = 1, m_J = \pm 1, \mathcal{N} = \pm 1\rangle \equiv 1/6$. These can be calculated using (A.16).

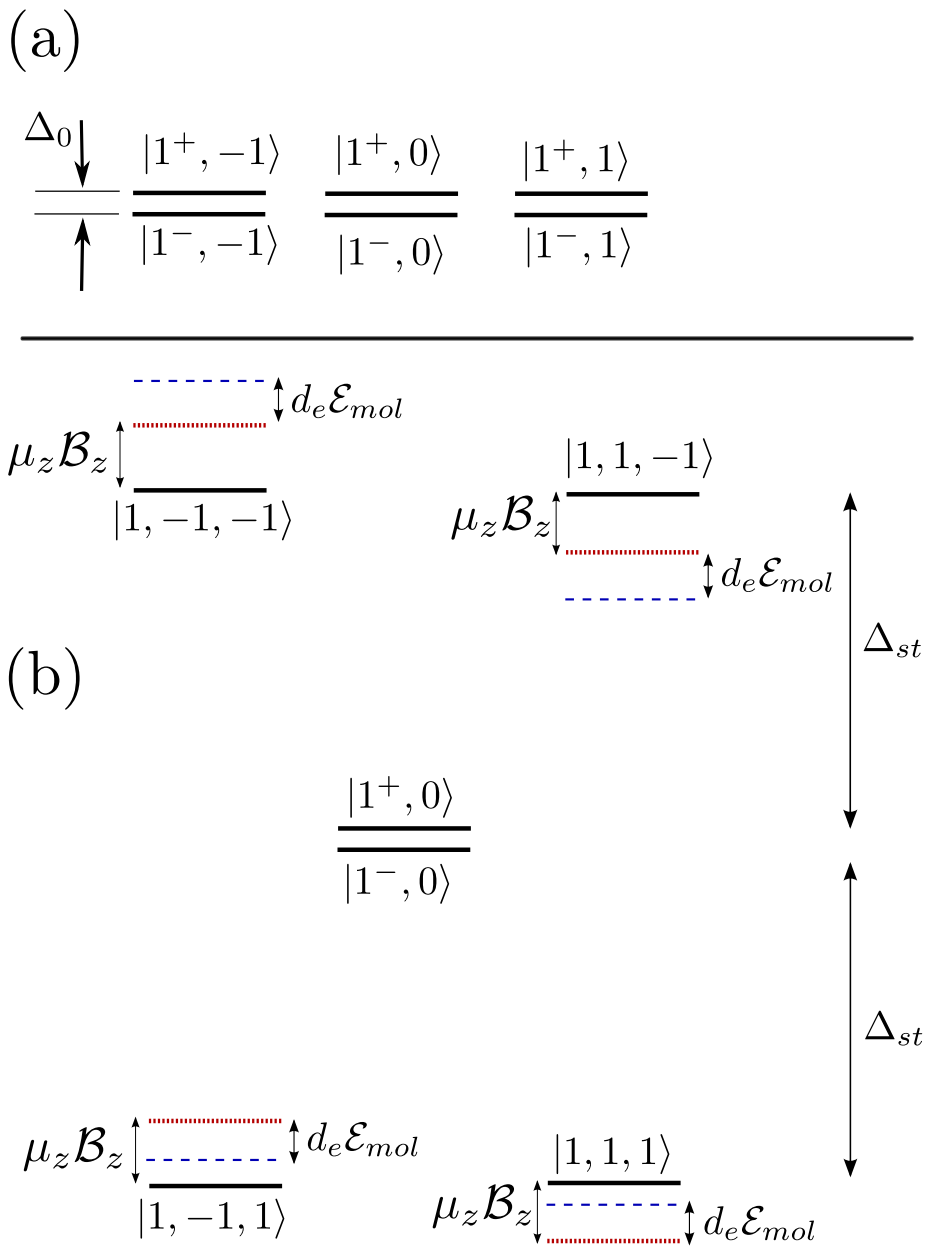

Figure 2.2: a) The structure of the $J = 1$ Ω-doublet in the H state when $\mathcal{E} = 0$, $\mathcal{B} = 0$. States are labeled as $|J^p, m_J\rangle$. b) The states in non-zero $\hat{z}$-directed $\mathcal{E}, \mathcal{B}$ fields. The tensor Stark shift Δ_{st}, Zeeman shift $\mu_z\mathcal{B}_z$ and the eEDM-induced shift $d_e\mathcal{E}_{mol}\Omega$ are shown (not to scale). The $m_J = 0$ states are not perturbed (or only weakly polarized by mixing with $J = 2$ levels), and continue to be denoted by $|J^p, m_J\rangle$ labels. The $m_J = \pm 1$ states are shown in the strongly electrically polarized regime, and are labeled $|J, m_J, \mathcal{N} = m_J\Omega\rangle$. The particular way in which the eEDM energy shift $d_e\mathcal{E}_{mol}\Omega$ behaves in these states makes it evident why such an Ω-doublet is useful for an eEDM measurement.

molecules is coupled to the polarization of the strong state preparation laser driving the $H, |J=1, m_J, \mathcal{N}\rangle \rightarrow C, |J=1^-, 0\rangle$ transition. As a result, the molecule is initially prepared by depleting the coherent superposition of $|m_J = \pm 1, \mathcal{N}\rangle$ that couples to the laser polarization $\vec{\epsilon}_{sp}$, leaving behind a dark state. This depletion process is effective because the excited state (C) has a number of decay pathways into other electronic states (X,H,Q) and various rovibrational states within those electronic states. With the laser polarization $\vec{\epsilon}_{sp} = \hat{y}$ for example, the initial state of the molecules is set to be

$$|\psi_i^{\mathcal{N}}\rangle = \frac{|m_J = +1, \mathcal{N}\rangle + |m_J = -1, \mathcal{N}\rangle}{\sqrt{2}}. \tag{2.2}$$

The label $\mathcal{N} = +1$ ($\mathcal{N} = -1$) corresponds to the lower (upper) Ω-doublet component. The tensor Stark shift Δ_{st} is large enough that levels with different values of $\mathcal{N}$ are spectrally resolved by the state preparation and detection lasers. Hence a particular value of $\mathcal{N}$ is chosen by appropriate tuning of the laser frequency.

The molecules in the beam then travel through the interaction region, where the relative phase of the two states in the superposition is shifted by the interaction of the magnetic moment $\vec{\mu}_{\mathcal{N}}$ with $\vec{\mathcal{B}}$, and the eEDM $\vec{d}_e$ with $\vec{\mathcal{E}}_{mol}$. In addition to this phase shift, there can be additional phase shifts picked up due to off-resonant energy shifts. The magnetic moment is written with a explicit $\mathcal{N}$ subscript to remind one that the magnetic moments are not identical in states with opposite values of $\mathcal{N}$ [BHJD09, Ham10].

After free evolution during flight over a distance L, the final wavefunction of the molecules is

$$|\psi_f^{\mathcal{N}}\rangle = \frac{e^{i\phi}|m_J = +1, \mathcal{N}\rangle + e^{-i\phi}|m_J = -1, \mathcal{N}\rangle}{\sqrt{2}}. \tag{2.3}$$

For a molecule with velocity v_x along the beam axis, the precession phase ϕ can be expressed as

$$\phi = \phi_r + \int_{x=0}^{x=L} \left(\mu_{\mathcal{N}}\mathcal{B} + d_e\mathcal{E}_{mol}\right) \frac{dx}{v_x} \equiv \phi_r + \phi_{\mathcal{B}} + \phi_{\mathcal{E}}. \tag{2.4}$$

$\phi_{\mathcal{E}}$ arises due to the eEDM and is small by assumption. $\phi_{\mathcal{B}}$ is the phase added by the static $\mathcal{B}$-field in the experiment. ϕ_r is (an assumed small) phase error, which models the phase shifts picked up due to off-resonant energy shifts and other interactions.

The phase ϕ is detected by projecting the final state $|\psi_f\rangle$ onto the detection state

$$|\psi_d^{\mathcal{N}}(\chi)\rangle = \frac{e^{i\chi}|m_J = +1, \mathcal{N}\rangle - e^{-i\chi}|m_J = -1, \mathcal{N}\rangle}{\sqrt{2}}. \tag{2.5}$$

This is done by illuminating the molecules with a detection laser (with polarization $\vec{\epsilon}_d$) tuned to the $H, v = 0, J = 1 \rightarrow E, v = 0, J = 0$ transition, and monitoring the laser-induced fluorescence emitted in the spontaneous decay from $E \rightsquigarrow X$.[10] The detection state $\left|\psi_d^{\mathcal{N}}\right\rangle$ is the "bright state" – the superposition of $H\ |J = 1, m_J = \pm 1, \mathcal{N}\rangle$ that is coupled to the excited electronic E state by the detection laser – and is set by the polarization of the detection laser, $\vec{\epsilon}_d$. χ is the angle between the laser polarizations $\vec{\epsilon}_{sp}$ and $\vec{\epsilon}_d$.[11].

The wavefunction of the E state has a small amount of ${}^3\Pi_0$ content ($\sim 1.5\%$), sufficient that the $H\ {}^3\Delta_1 \rightarrow E$ transition can be driven with a strong laser, and a large amount of ${}^1\Sigma$ content ($\sim 50\%$) so that the decay from $E \rightarrow X\ {}^1\Sigma$ has a large branching ratio [KDSP94]. Excitation of laser-induced fluorescence with such a transition allows for efficient rejection of scattered light from the detection laser, since the emitted fluorescence photons are at a much bluer wavelength than the laser. This means that the laser scatter can be efficiently filtered, without contamination of the signal by effects such as re-fluorescence of the filter.

The fluorescence photons from the E state are emitted isotropically. A fraction of them are collected by the light collection optics and detected by photodetectors.[12]

The detection sequence is as follows: the molecular state $|\psi_f\rangle$ is projected onto

[10] At the time of writing, the choice of the detection transition was not completely resolved. The choices are the $H \rightarrow C$ transition (1090 nm), $H \rightarrow E$ transition (908 nm) or potentially, the $H \rightarrow F$ transition (767 nm). Each transition has its pros and cons, in terms of the laser intensity required to saturate the transition, spatial distribution of the emitted fluorescence, susceptibility to light shifts etc. In the rest of this thesis, the discussion will assume that the $H \rightarrow E$ transition is used. The results and discussion in this following section are general and can be carried over to the other detection transitions, with appropriate modifications to the relative phase between $|m_J = \pm 1, \mathcal{N}\rangle$ in $|\psi_d\rangle$ to account for polarization-dependent matrix elements between the H and excited states.

[11] This is analogous to the RF offset phase between separated oscillatory field regions used in the Ramsey technique [Ram85]. It corresponds to rotating the detection basis with respect to the state preparation basis. Only the relative angle between the state preparation and detection bases is physically meaningful.

[12] The photodetectors could be photomultiplier tubes, which have a large noiseless internal gain, or silicon/avalanche photodiodes, which are used with external amplifying circuitry. Regardless of the actual device, the signal is obtained as a current out of the detector that is proportional to the photon detection rate.

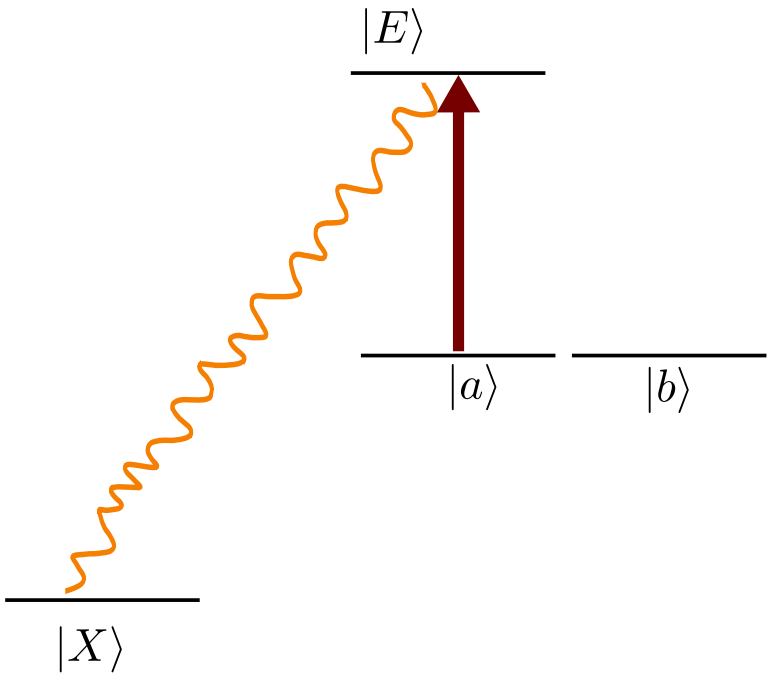

Figure 2.3: The states $|a\rangle, |b\rangle$ are degenerate, and respectively represent the bright and dark superpositions of $|m_J = \pm 1\rangle$. A strong drive laser couples only $|a\rangle$ to an excited state $|E\rangle$, which spontaneously decays to the ground state $|X\rangle$ emitting a photon. Consider the general superposition state $|\psi\rangle = \alpha|a\rangle + \beta|b\rangle$. In terms of dressed states (combined states of the molecule-radiation field) of the form $|\Psi\rangle = |\text{molecule}\rangle|\text{photon}\rangle$, the wavefunction at time t is

$$|\Psi(t)\rangle = \alpha\Big(\frac{|a\rangle|1\rangle + |E\rangle|0\rangle}{\sqrt{2}} + e^{-i\Omega_R t}\ \frac{|a\rangle|1\rangle - |E\rangle|0\rangle}{\sqrt{2}}\Big) + \beta|b\rangle|1\rangle. \tag{2.6}$$

Fluorescence is given off when E decays to X. The fluorescence emission rate Γ_{EX} is given by Fermi's Golden Rule:

$$\begin{aligned}
\Gamma_{EX} &\propto |\langle X|D|\psi\rangle|^2 \\
&\propto |\langle X|D|E\rangle\langle E|\psi\rangle|^2 \\
&\propto D_{XE}^2|\sqrt{2}\alpha\ \sin\big(\frac{\Omega_R t}{2}\big)|^2 \\
&\propto D_{XE}^2|\alpha|^2.
\end{aligned} \tag{2.7}$$

The last step is due to the time-average over $\sin^2\big(\frac{\Omega_R t}{2}\big)$. The fluorescence emission probability is proportional to $|\langle a|\psi\rangle|^2$. The projective part of the measurement is due to spontaneous emission.

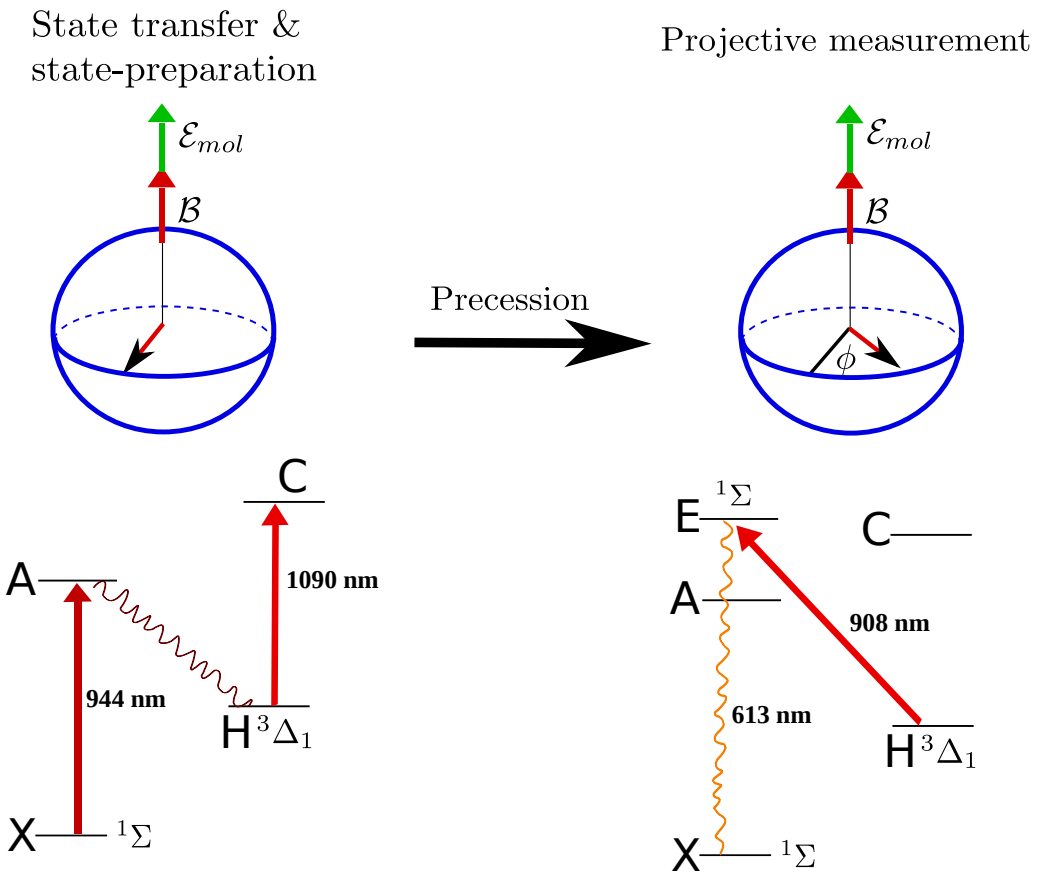

Figure 2.4: The measurement can be pictorially represented on the Bloch sphere formed by the two states $|m_J = \pm 1, \mathcal{N}\rangle$. In this subspace, the pseudo-spin vector precesses around the $\mathcal{B}$-field (due to the magnetic moment $\mu_{\mathcal{N}}$) and the internal $\mathcal{E}$-field $\mathcal{E}_{mol}$ (due to the eEDM). The angle by which the pseudo-spin vector precesses around the z-axis of the Bloch sphere is ϕ, where ϕ is defined in (2.4).

one of the orthogonal states $|X_{\mathcal{N}}\rangle, |Y_{\mathcal{N}}\rangle$, defined as follows.

$$\begin{aligned} |X_{\mathcal{N}}\rangle &= \left|\psi_d^{\mathcal{N}}(\chi=0)\right\rangle, |Y_{\mathcal{N}}\rangle = \left|\psi_d^{\mathcal{N}}(\chi=-\pi/2)\right\rangle \\ P_X &= |\langle X_{\mathcal{N}}|\psi_f\rangle|^2 = \sin^2\phi, P_Y = |\langle Y_{\mathcal{N}}|\psi_f\rangle|^2 = \cos^2\phi \end{aligned} \tag{2.8}$$

If the populations (P_X, P_Y) in both these basis states is measured in rapid succession, before a packet of molecules leave the volume illuminated by the detection laser, then the precession phase can be measured using the asymmetry, $\mathcal{A}$, defined as

$$\mathcal{A} \equiv \frac{P_Y - P_X}{P_Y + P_X} = \cos 2\phi. \tag{2.9}$$

This method, of measuring both P_X and P_Y on the same pulse of molecules, normalizes against fluctuations in the intensity of the molecular beam.

Effect of the velocity distribution

The analysis was carried out up to this point assuming that all the molecules in the beam have the same velocity $\vec{v}$. The effect of the velocity distribution is considered now. In the experiment, the molecules are produced from the beam source with a distribution of forward (along the beamline, the x-axis) and transverse velocities (along the y, z-axes). These distributions can be considered as independent.

The distribution of the transverse velocity component $f(v_z)$ affects the interaction of molecules with the state preparation and detection lasers due to the Doppler effect.[13] The distribution $f(v_y)$ could potentially affect the interaction of the molecules with the lasers, as molecules with different v_y spatially separate and sample different parts of the wavefront of the laser beams. It is assumed that the $\mathcal{E}$- and $\mathcal{B}$-fields are sufficiently uniform over the volume sampled by the ensemble. Note that the transverse velocity does not affect the transit time through the experiment. The measurement can be made insensitive to the distribution of $v_{y,z}$ components of the molecular velocities by a) first collimating the molecular beam to obtain a small spread of $v_{y,z}$, b) expanding the wavefronts of the state preparation and detection lasers to ensure that the wavefronts are uniform over the region sampled by the collimated molecular beam along the y-direction, and c) having sufficiently large intensities in the laser beams in order to saturate the state preparation and detection

[13] Note that the lasers propagate along the $\hat{z}$ direction

transitions,[14] so that the excitation is insensitive to the Doppler effect.

The forward velocity distribution $f(v_x)$ affects the transit time through the interaction region, and therefore the phase that is picked up by different molecules in the ensemble. This is considered now. The forward velocity is separated into its mean and deviations about the mean: $v_x = \overline{v}_x + \widetilde{v}_x$. The deviations $\widetilde{v}_x$ are normally distributed with a standard deviation $\Delta\widetilde{v}_x$. This is due to the following physics: in a buffer gas cooled beam, the molecules undergo collisions with the buffer gas in the production cell and during the expansion out of the cell, which thermalizes them to a temperature T_{beam}.[15] The distribution of one velocity component of a gas at thermal equilibrium is described by the Maxwell-Boltzmann distribution, which is a normal distribution.

The phase shifts $\phi_{\mathcal{E}}, \phi_r$ are small compared to $\phi_{\mathcal{B}}$ by assumption, and so they can be ignored in the following analysis. The precession phase in (2.4) is

$$\begin{aligned}
\phi &\approx \mu_{\mathcal{N}} \int_{x=0}^{x=L} \mathcal{B}\, \frac{dx}{v_x} \\
&= \left[1 - \frac{\widetilde{v}_x}{\overline{v}_x} + \left(\frac{\widetilde{v}_x}{\overline{v}_x}\right)^2 + \dots\right] \int_{x=0}^{x=L} dx\, \frac{\mu_{\mathcal{N}}\overline{\mathcal{B}}}{\overline{v}_x} \\
&\approx \left[1 - \frac{\widetilde{v}_x}{\overline{v}_x}\right] \int_{x=0}^{x=L} dx\, \frac{\mu_{\mathcal{N}}\overline{\mathcal{B}}}{\overline{v}_x}
\end{aligned} \tag{2.10}$$

The last step is justified because in buffer gas cooled beams, $\overline{v}_x \approx 170$ m/s, and the standard deviation of $\widetilde{v}_x$, $\Delta\widetilde{v}_x \approx 20$ m/s [HPG$^+$11]. Therefore, the second order and higher terms in $\widetilde{v}_x/\overline{v}_x$ only have a small effect and we can write $\Delta\phi = \phi\frac{\Delta\widetilde{v}_x}{\overline{v}}$ for the standard deviation of the phase due to the velocity distribution.

Equation (2.9) for the count rate can be averaged over the ensemble of velocities by combining the definition $\cos x = (e^{ix} + e^{-ix})/2$, with the following standard result from probability theory:

If X is a random variable, then $\langle \exp(isX)\rangle \equiv M_X(s)$ where $M_X(s)$ is the characteristic function *of the probability distribution of X. If X is normally distributed,*

[14] See [BKD08] for a discussion of optical saturation in a two-level system.

[15] T_{beam} is set by the expansion dynamics. In an effusive molecular beam, this temperature is equal to the temperature of the buffer gas in the production cell. In fully supersonic beams, this temperature can be calculated from the standard formulae for isentropic expansion [LL87]. For hydrodynamically extracted buffer gas beams, numerical/analytical methods can be used to calculate the temperature [HPG$^+$11, BSD11].

with mean $\langle X\rangle$ and standard deviation ΔX, the characteristic function is

$$M_X(s) = \exp(is\langle X\rangle)\ \exp\Big(-\frac{s^2\Delta X^2}{2}\Big). \tag{2.11}$$

Therefore we find that

$$\langle\cos 2\phi\rangle \quad = \quad \exp(-2\Delta\phi^2)\ \cos(2\phi) \tag{2.12}$$

and (2.9) becomes

$$\langle\mathcal{A}\rangle \quad = \quad \exp(-2\Delta\phi^2)\cos 2\phi = \mathcal{C}\cos 2\phi. \tag{2.13}$$

Here the contrast $\mathcal{C}$ has been defined. The effect of the contrast is to modify P_X from $\sin^2\phi$ into

$$P_X = \frac{1-\mathcal{C}}{2} + \mathcal{C}\sin^2\phi. \tag{2.14}$$

This makes it evident why $\mathcal{C}$ is called the contrast.[16]

For the buffer gas cooled beam reported in [HPG+11], the contrast due to the finite spread of velocities is predicted to be $\mathcal{C} = 0.98$ for $\phi \approx \pi/4$. For small precession phases, therefore, the effect of the velocity spread should be negligible, though this remains to be verified experimentally.

2.3 Phase noise

Some sources of phase noise, that contribute to the uncertainty in the measurement of the precession phase ϕ, are examined in this section.

2.3.1 Projection noise

Consider a beam of exactly N particles that are emitted by a source. Let the state space of the particles have 2 orthogonal basis states $|a\rangle, |b\rangle$. Assume that the particles are (independently) projected onto $|a\rangle$ by some means and that the number that are projected, N_a, is measured. Assume that each particle in the beam is in a

[16] Other contributions to a reduction of contrast include: elliptical polarization in the state preparation/detection lasers (e.g. in the detection laser, this would result in the excitation of $|Y_{\mathcal{N}}\rangle$ when $\vec{\epsilon}_d$ is set to nominally excite $|X_{\mathcal{N}}\rangle$), and incomplete depletion of the bright superposition during the state preparation stage (which would add a background of unpolarized molecular spins).

state, $|\psi\rangle = \frac{|a\rangle+|b\rangle}{\sqrt{2}}$. When the particles are projectively measured, each particle is projected onto $|a\rangle$ with a probability 1/2 or onto $|b\rangle$ with a probability 1/2. Due to this probabilistic process, described by a binomial distribution, there are deviations in the value measured for N_a every time the experiment is repeated. The mean value measured is $\overline{N_a} = N/2$ as expected, but N_a now has a non-zero standard deviation $\Delta N_a = \sqrt{N/4}$ determined by the binomial distribution. This is termed quantum projection noise (QPN) [IBB+93]. It arises even if there are absolutely no fluctuations in the number of particles emitted by the beam source.

We now estimate the phase noise due to QPN for a general state $|\psi\rangle = \cos\phi\,|a\rangle + \sin\phi\,|b\rangle$.[17] The mean value measured for N_a is $\overline{N_a} = N\cos^2\phi$. The standard deviation is $\Delta N_a = \sqrt{N\cos^2\phi\,\sin^2\phi}$, for this process governed by the binomial distribution. This leads to an uncertainty in the measurement of the phase that can be calculated as follows.

$$\begin{aligned} \Delta N_a &= 2N\cos\phi\,\sin\phi\,\Delta\phi \equiv \sqrt{N\cos^2\phi\,\sin^2\phi} \\ \Rightarrow \Delta\phi &= \frac{1}{2\sqrt{N}}. \end{aligned} \tag{2.15}$$

This represents the quantum mechanical limit to the measurement of the precession phase using N independent particles. Note that this projection noise contribution is independent of the value of the precession phase angle, ϕ.

If, due to averaging over the velocity distribution, the mean value measured for N_a is $\overline{N_a} = N\mathcal{C}\cos^2\phi + N\frac{(1-\mathcal{C})}{2}$, then the uncertainty in the phase measurement is

$$\Delta\phi = \frac{1}{2\,\mathcal{C}\sqrt{N}}. \tag{2.16}$$

2.3.2 Effect of finite detection efficiency

Consider the process described in the previous section, but now including a finite efficiency for detecting the molecules. Assume that, when the state $|\psi\rangle = \cos\phi\,|a\rangle + \sin\phi\,|b\rangle$ is projectively measured by interrogating the population in $|a\rangle$, photons emitted in the process are detected with an efficiency p_d.[18] In such an experiment,

[17] Here, if $|\psi\rangle$ represents $|\psi_f\rangle$, then $|b\rangle$ ($|a\rangle$) represents the detection basis state $|X_{\mathcal{N}}\rangle$ ($|Y_{\mathcal{N}}\rangle$).

[18] This efficiency factor includes effects such as the e.g. the finite acceptance of the light collection optics, the loss of photons in the light pipes and fiber bundles, and the finite quantum efficiency of the detector. For the first-generation ThO experiment, this efficiency is $p_d \sim 1\%$.

the probability of measuring a photon is $p_\gamma = p_d \cos^2\phi$.[19] The detection of photons from the molecules is governed by a binomial process, with probability p_γ. Therefore, when N molecules are independently interrogated, the mean value measured for N_a is $\overline{N_a} = Np_\gamma = Np_d \cos^2\phi$, and the standard deviation in N_a is $\sqrt{Np_\gamma(1-p_\gamma)}$. We estimate the phase noise due to this binomial process as above.

$$\begin{aligned} \Delta N_a &= 2Np_d \cos\phi \sin\phi \Delta\phi \equiv \sqrt{Np_d \cos^2\phi (1 - p_d \cos^2\phi)} \\ \Rightarrow \Delta\phi &= \frac{1}{2\sqrt{N}} \sqrt{\frac{1 - p_d \cos^2\phi}{p_d \sin^2\phi}}. \end{aligned} \tag{2.17}$$

In general, the phase noise now depends on the value of the precession phase angle.

In the case when $\phi \approx \pi/4$ ($\cos^2\phi = \sin^2\phi = 1/2$), as is relevant for the eEDM experiment when biased to be sensitive to the eEDM-induced phase, this expression becomes

$$\Delta\phi = \frac{1}{2\sqrt{N}} \sqrt{\frac{2 - p_d}{p_d}}. \tag{2.18}$$

In the limit of small detection efficiency ($p_d \ll 1$), this becomes

$$\Delta\phi \approx \frac{1}{2\sqrt{Np_d/2}} = \frac{1}{2\sqrt{N_a}}. \tag{2.19}$$

As intuitively expected, this is equal to the contribution from shot noise on N_a detected molecules.

In the limit of ideal detection ($p_d = 1$), regardless of the value of ϕ, (2.17) becomes

$$\Delta\phi = \frac{1}{2\sqrt{N}} \tag{2.20}$$

as expected from the discussion in Section 2.3.1. For non-zero but finite detection efficiencies, (2.17) can be used to estimate the phase noise contribution from projection noise.

[19] The probabilities of the various outcomes of the experiment are as follows: (a) $\mathcal{P}$(molecule projected on to $|a\rangle$, and photon is detected) $= p_\gamma = p_d \cos^2\phi$; (b) $\mathcal{P}$(molecule projected on to $|a\rangle$, but photon is not detected) $= (1 - p_d)\cos^2\phi$; (c) $\mathcal{P}$(molecule projected on to $|b\rangle$, so no photon is emitted) $= \sin^2\phi$. These probabilities add up to 1.

2.3.3 Magnetic noise

We examine the effect of phase fluctuations arising from fluctuations in the magnetic field. We restrict our attention in this section to fluctuations in $\mathcal{B}_z$.[20]

We separate the magnetic field into its mean value, plus fluctuations from the mean

$$\mathcal{B} \;=\; \overline{\mathcal{B}} + \widetilde{\mathcal{B}} \tag{2.21}$$

and find that the resultant fluctuations in the precession phase (2.4) are given by

$$\widetilde{\phi}_{\mathcal{B}} = \mu_{\mathcal{N}} \overline{\mathcal{B}} \tau \times \Big(\frac{1}{\tau} \int_0^\tau dt \; \widetilde{\mathcal{B}} \Big). \tag{2.22}$$

Here $\tau = L/\overline{v}_x$ is the time of flight of molecules with a velocity $\overline{v}_x$ in the interaction region, between the state preparation and detection lasers.[21] An important point to note is that magnetic field fluctuations, $\widetilde{\mathcal{B}}$, are averaged over the time of flight through the interaction region. In the frequency domain, this corresponds to a low-pass filtering of the noise spectrum of the magnetic field, and means that only spectral components within a bandwidth $\Delta f \sim 1/\tau$ around DC contribute to the magnetic field fluctuations.

$\widetilde{\mathcal{B}}$ is a random variable that fluctuates in time.[22] It can be considered to consist of two components. The first is white Gaussian noise, $\widetilde{\mathcal{B}}_{WGN}$, in which every frequency component of the noise has a zero-mean Gaussian distribution of amplitudes, and the variance is identical for every frequency component. Thermal noise (magnetic Johnson noise) is well described by such a distribution. The second is colored noise $\mathcal{B}_{CN}$, which typically tends to dominate over white noise at low frequencies.[23] Its moments are harder to calculate *a priori*. Since the phase measurement low-pass

[20] Due to the tensor Stark shift, fluctuating components of the magnetic field along the x and $y-$ axes lead to common-mode shifts in the energies of $|J = 1, m_J = \pm 1\rangle$ states, and so these do not contribute to the phase difference that is measured. There can be shifts due to fluctuating transverse $\mathcal{E}$ and $\mathcal{B}$-field components which are not common-mode - these are treated in Chapter 3 in relation to systematic errors.

[21] With $L = 22$ cm, and $\overline{v}_x = 170$ m/s, $\tau = 1.3$ ms.

[22] Spatial variations of $\mathcal{B}$ along the path of the molecules are effectively converted into temporal fluctuations in the rest frame of the molecules. However, since all the spatial variations are between $x = 0$ and $x = L$, and since the phase is an integral over the path of the molecules, the spatial variations are all averaged out.

[23] This can arise from a number of technical, yet unavoidable, causes. For example, $1/f$ noise in the current supplies, relaxation of the grains in the magnetic shielding after demagnetization, motion of magnetic materials in the lab environment, and so on.

filters the magnetic noise, $\widetilde{\mathcal{B}}_{CN}$ tends to dominate the effects in the measurement. In the following we assume that $\widetilde{\mathcal{B}}$ can be described in terms of its rms value alone - we ignore higher moments than the second, which is equivalent to assuming that the spectral components of both white and colored noise are normally distributed.

We define $\widetilde{\mathcal{B}_\tau} = \frac{1}{\tau}\int_0^\tau dt\ \widetilde{\mathcal{B}}$ for convenience, and calculate its rms value now. The magnetic field noise in terms of its spectral components is

$$\widetilde{\mathcal{B}}(t) = \int_{-\infty}^{\infty} \widetilde{\mathcal{B}}(\nu)\ e^{-i2\pi\nu t}\ d\nu. \tag{2.23}$$

The integral $\widetilde{\mathcal{B}_\tau}$ can be rewritten as

$$\widetilde{\mathcal{B}_\tau} = \frac{1}{\tau}\int_0^\tau \widetilde{\mathcal{B}}(t)\ dt = \int_{-\infty}^{\infty} \widetilde{\mathcal{B}}(\nu)\ e^{-i\pi\nu\tau}\mathrm{sinc}(\nu\tau)\ d\nu. \tag{2.24}$$

The variance of $\widetilde{\mathcal{B}_\tau}$ is

$$(\Delta\widetilde{\mathcal{B}_\tau})^2 = \langle \int_{-\infty}^{\infty} \widetilde{\mathcal{B}}(\nu)\ e^{-i\pi\nu\tau}\mathrm{sinc}(\nu\tau)\ d\nu \int_{-\infty}^{\infty} \widetilde{\mathcal{B}}(\mu)\ e^{-i\pi\mu\tau}\mathrm{sinc}(\mu\tau)\ d\mu\rangle \tag{2.25}$$

where $\langle\ldots\rangle$ denotes an average over the distribution of amplitudes of the spectral components $\widetilde{\mathcal{B}}(\nu)$. Using the fact that different spectral components of the noise are uncorrelated, $\langle\widetilde{\mathcal{B}}(\nu)\widetilde{\mathcal{B}}(\nu)\rangle \equiv \widetilde{\mathcal{B}_\nu}^2\ \delta(\mu+\nu)$, we find that the rms value of $\widetilde{\mathcal{B}_\tau}$ is

$$\Delta\widetilde{\mathcal{B}_\tau} = \sqrt{\int_{-\infty}^{\infty} \widetilde{\mathcal{B}_\nu}^2\ \mathrm{sinc}^2(\nu\tau)\ d\nu}. \tag{2.26}$$

Here $\widetilde{\mathcal{B}_\nu}$ is the spectral density of the $\mathcal{B}$-field noise.[24] In the case of white Gaussian noise, the equation can be simplified to $\Delta\widetilde{\mathcal{B}_\tau} = \widetilde{\mathcal{B}_\nu}/\sqrt{\tau}$, where $\Delta\nu = 1/\tau = 770$ Hz, is the effective low-pass bandwidth discussed before.

Using the methods described in Section A.5, a conservative estimate of the spectral density of $\widetilde{\mathcal{B}}_{WGN}$ due to conductors around the molecules is $\widetilde{\mathcal{B}_\nu} \lesssim 300$ fT/$\sqrt{\mathrm{Hz}}$, leading to $\Delta\widetilde{\mathcal{B}_\tau} \lesssim 10$ pT. The resultant phase fluctuations have an rms value $\Delta\phi \lesssim 10^{-9}$ rad. We shall see that this is significantly smaller than targeted sensitivity of the experiment.

[24]The spectral density I_ν of a quantity I is defined here as the root mean square value of I measured in a bandwidth $\Delta\nu$ centered at a frequency ν, divided by $\sqrt{\Delta\nu}$. It has units of $[I]/\sqrt{\mathrm{Hz}}$.

2.4 eEDM sensitivity of the experiment

The eEDM-induced phase $\phi_{\mathcal{E}}$ can be separated from the precession phase as follows. We assume that the $\mathcal{B}$-field is set so that $\overline{\phi}_{\mathcal{B}} = \pm\pi/4$. This bias phase enhances the sensitivity of $\mathcal{A}$ to small phase offsets. (We assume that $\overline{\phi}_{\mathcal{B}}$ is set perfectly, lumping any errors in this bias phase from the magnetic field into the residual phase $\overline{\phi}_r$.) We then have from (2.9)

$$\begin{aligned} \mathcal{A} &= \mathcal{C}\cos 2(\overline{\phi}_{\mathcal{B}} + \phi_{\mathcal{E}} + \overline{\phi_r}) \\ &= -\mathcal{C}\ \mathrm{sgn}(\mathcal{B})\cdot\sin 2(\phi_{\mathcal{E}} + \overline{\phi_r}) \\ &\simeq -2\ \mathcal{C}\ \mathrm{sgn}(\mathcal{B})\cdot(d_e\mathcal{E}_{mol}\tau + \overline{\phi_r}). \end{aligned} \tag{2.27}$$

Recall that $\mathcal{E}_{mol} \propto \mathrm{sgn}(\mathcal{E}_{lab})\cdot\mathrm{sgn}(\mathcal{N})$. The eEDM contribution to the precession phase is extracted as the part that is odd under reversals of both $\mathcal{E}_{lab}$ and $\mathcal{N}$. Any components of the phase error $\overline{\phi}_r$ that are odd under these reversals will contribute to the systematic error - such effects are examined in Chapter 3.

Using (2.16) and (2.19) for the fundamental phase noise, the statistical uncertainty in the measurement of an eEDM can be written as

$$\Delta d_e = \frac{1}{2\,\mathcal{C}\,\mathcal{E}_{mol}\tau\sqrt{\dot{N}_d T}} \tag{2.28}$$

where T is the integration time of the measurement, and $\dot{N}_d T$ is the total number of photoelectrons detected (= molecules detected) during the projective measurement.

The statistical sensitivity achievable with an eEDM experiment using a beam of ThO molecules can now be estimated. Table 2.1 contains a list of the various parameters that enter the estimate of the statistical sensitivity. The model used for the molecular beam is that N_{beam} molecules, in a single quantum state, are emitted due to one pulse of laser ablation into a solid angle Ω_b by the molecular beam source. It is assumed that pulses of molecules are emitted from the source with a repetition rate R, set by the ablation laser. In estimating the sensitivity, it is assumed that R = 10 Hz, although higher repetition rates are technologically possible.

The molecules from the beam source traverse a length L_0 of the apparatus before they are pumped into the H state. This length L_0 reduces the number of molecules that survive the flight to the end of the apparatus. L_0 is set by the length of the vacuum fittings required to penetrate the magnetic shields, and by the vacuum hard-

ware needed in the region where the molecular beam is collimated and characterized. $L_0 = 60$ cm is an assumed value. It is assumed that the state-transfer (optical pumping) and state preparation lasers are located close to each other. The length L of the flight path between state preparation and detection lasers, over which the molecules precess in the $\mathcal{E}$ and $\mathcal{B}$-fields, has been introduced before. $L = 22$ cm is set by the design of the $\mathcal{B}$-field coils.

e_s, e_p are the efficiencies for state-transfer and state preparation respectively. e_s for the optical pumping scheme of transfer from $X \rightarrow A \rightsquigarrow H$ is measured to be $\sim 40\%$.[25] e_p is calculated from the rotational branching ratios for decay from $A, J = 0 \rightarrow H, J = 1$ sublevels in the $\mathcal{E}$-field, assuming that the dark state can be prepared with unity efficiency. e_g, e_q are respectively the geometric efficiency for collecting photons emitted from the molecules (set by the solid angle covered by the light collection optics), and the quantum efficiency of the detector. c_{EX} is the Franck-Condon factor for decay from $E, v = 0 \rightsquigarrow X, v = 0$, which yields photon at 613 nm (decays into other vibrational states yield photons that are at different wavelengths – I have assumed that only photons at 613 nm are detected).

Assuming that a 24 hr integration time is used for the experiment, the eEDM uncertainty that is achievable is estimated to be $\delta d_e = 3.3 \times 10^{-29}$ e cm. This corresponds to an uncertainty $\delta\phi_{\mathcal{E}} \approx 10$ μrad.

Improvements are foreseeable in some of parameters that enter this estimate, and these will be mentioned in Chapter 6.

[25] This was measured by Ben Spaun, by comparing the signal heights of laser-induced fluorescence from the ground state (using the $X, J = 1 \rightarrow C, J = 1$ transition), and from the H state (using the $H, J = 1 \rightarrow E, J = 0$ transition) after optical pumping on the $X, J = 1 \rightarrow A, J = 0 \rightsquigarrow H, J = 1$ transition.

Parameter	Estimate
[a]**Molecules/pulse in $X\|1,0\rangle$ state**, N_{beam}	5.6×10^{10}
[a]**Beam forward velocity**, $\overline{v}_x$	170 m/s
[a]**Beam divergence**, Ω_b	0.35 sr
Ablation laser repetition rate, R	10 Hz
Beam length before interaction region, L_0	60 cm
Flight length in interaction region, L	22 cm
Detected area of beam, A	1 cm^2
Detected solid angle of beam, Ω_d	1.9×10^{-4} sr
Coherence time, $\tau = L/\overline{v}_x$	1.3 ms
[b]Surviving H state fraction after flight, $f = e^{-\tau/\tau_H}$	0.49
State transfer efficiency, e_s	40 %
State preparation efficiency, e_p	16.6 %
[c]**Franck-Condon factor** $E, v = 0 \to X, v = 0$, c_{EX}	0.87
Geometric efficiency of fluorescence collection, e_g	10 %
[d]**Quantum efficiency of photon detection**, e_q	10.5 %
Photoelectron counts/s, $\dot{N}_d = N_{beam} R \frac{\Omega_d}{\Omega_b} f \; e_s e_p c_{EX} e_g e_q$	2.4×10^4/s
Contrast, $\mathcal{C}$	0.98
[e]**Internal field in ThO**, $\mathcal{E}_{mol}$	104 GV/cm
eEDM uncertainty ($T = 1$ s), Δd_e	9.6×10^{-27} e cm
eEDM uncertainty ($T = 24$ hr), Δd_e	3.3×10^{-29} e cm

Table 2.1: An estimate of the statistical uncertainty in the measurement of an eEDM, achievable with a ThO molecular beam experiment. This estimate uses currently verified numbers where available and conservative estimates otherwise. Parameters in bold are independent input parameters. Note that this estimate does not correspond to the sensitivity of the experiment at the time of writing.

[a] Based on parameters reported in [HPG+11].
[b] The lifetime of the H state, $\tau_H = 1.8$ ms (see Section 4.2).
[c] Value from [WS72], verified using overlap of simple harmonic oscillator wavefunctions for E, X with the constants in [EL84].
[d] Hamamatsu R8900-20 photomultiplier tube, at λ=613 nm.
[e] The value of $\mathcal{E}_{mol}$ for the H state in ThO is calculated in [MB08].

Chapter 3

Potential systematics

> The only way to rectify our reasonings is to make them as tangible as those of the Mathematicians, so that we can find our error at a glance, and when there are disputes among persons, we can simply say: Let us calculate.
>
> Gottfried Leibniz, *The Art of Discovery*

Some sources that lead to a phase offset $\overline{\phi_r}$, which could potentially mimic an eEDM signal, are examined in this chapter. This is not an exhaustive list, but merely some of the sources that were considered at the beginning of the experiment. Systematic errors have devious ways of sneaking into a measurement, and *a priori* estimates only reveal the limits of the experimenter's paranoia/imagination. Nevertheless, the size of systematic errors generated by any proposed mechanism can always be quantitatively calculated. We first consider some harmless sources of phase offsets, followed by a discussion of nefarious ways in which these effects can combine to result in an eEDM-like signal. In all the discussions in this chapter, the aim is to distinguish phase offsets $\overline{\phi_r}$ from the eEDM-phase $\phi_{\mathcal{E}} = d_e \mathcal{E}_{mol} \tau$, using the following properties of $\phi_{\mathcal{E}}$:[1]

- It reverses sign under $\mathcal{N}$ reversal.
- It reverses sign under reversal of the lab electric field, $\vec{\mathcal{E}}$.
- In the strongly electrically polarized regime, it is independent of the magnitude of $\vec{\mathcal{E}}$.

[1] These properties are due to (2.27).

- It is independent of the sign and strength of the $\mathcal{B}$ field.

Any component of $\overline{\phi_r}$ that mimics this behavior will lead to a systematic error. Also recall from Section 2.4 that the expected sensitivity of the first-generation ThO experiment is $\delta\phi_{\mathcal{E}} = 10^{-5}$ rad, corresponding to $\delta d_e = 3.3 \times 10^{-29}$ e cm. Allowing for improvements and with a general optimism about future advances in technology, we will assume that a statistical sensitivity $\delta\phi_{\mathcal{E}} \sim 10^{-6}$ rad can be achieved in some incarnation of the experiment with ThO. Any offset phases $\overline{\phi}_r$ that approach this value will be considered as potentially dangerous systematic errors.

An important note with regard to $\mathcal{E}$-linear effects: phase shifts that are quadratic in $\vec{\mathcal{E}}$ can lead to effects that seem linear in the part of $\vec{\mathcal{E}}$ that is under the experimenter's control, if there is a non-reversing electric field $\vec{\mathcal{E}}_{nr}$ along with the nominally reversing lab field $\vec{\mathcal{E}}_r$: $\mathcal{E}^2 = (\vec{\mathcal{E}}_r + \vec{\mathcal{E}}_{nr})^2 = \mathcal{E}_r^2 + \mathcal{E}_{nr}^2 + 2\vec{\mathcal{E}}_r \cdot \vec{\mathcal{E}}_{nr}$. The cross term $2\vec{\mathcal{E}}_r \cdot \vec{\mathcal{E}}_{nr}$ appears to be linear in the lab electric field.

3.1 Harmless components

3.1.1 Electric quadrupole shifts

A state of an atom or molecule with $J \geq 1$, such as the $H, J = 1$ state in ThO, can have non-zero matrix elements of the quadrupole moment operator between its sublevels. The Hamiltonian for the interaction of a quadrupole moment Q with an electric field gradient is

$$H_Q = -\sum_{i,j} Q_{ij} \nabla_i \mathcal{E}_j = -\sum_{\mu} Q_{2,\mu} (\nabla\mathcal{E})^*_{2,\mu} \tag{3.1}$$

where the second equation is written in the spherical tensor basis.

An electric field gradient can arise in the experiment due to imperfections or misalignments in the field plates. Since the field gradient is produced in these situations by the imperfect geometry of the electrodes, $\vec{\nabla}\vec{\mathcal{E}}$ scales linearly with the applied electric field $\vec{\mathcal{E}}$. As a result of this interaction, the components $Q_{2,\pm 2}$ of the electric quadrupole moment can potentially lead to a frequency shift between $|m_J = \pm 1\rangle$ that can appear to be linear in the lab electric field.

The matrix elements of the quadrupole moment between states in the $|J, m_J, \Omega\rangle$

basis are of the form

$$\langle J, m'_J, \Omega'; \Gamma | Q_{2,\mu} | J, m_J, \Omega; \Gamma \rangle = \langle J, m'_J | 2, \mu; J, m_J \rangle \, \langle J, \Omega' | 2, q; J, \Omega \rangle \; Q_{H,q} \tag{3.2}$$

using (A.16). $Q_{H,q}$ are spherical tensor components of the intrinsic quadrupole moment of the H state. First we consider the two states with $\mathcal{N} = +1$, i.e. the sublevels $|m_J = \pm 1, \Omega = \pm 1\rangle$.[2] The matrix elements of the quadrupole Hamiltonian can be restricted to this subspace, since all other off-diagonal matrix elements are suppressed greatly by the tensor Stark splitting. The Hamiltonian is

$$\begin{aligned} H &= H_Q + H_{Zeeman} + H_{EDM} \\ &= \begin{pmatrix} Q_\parallel & Q_\perp \\ Q_\perp & Q_\parallel \end{pmatrix} + \begin{pmatrix} \mu_\mathcal{N}\mathcal{B} & \\ & -\mu_\mathcal{N}\mathcal{B} \end{pmatrix} + \begin{pmatrix} d_e\mathcal{E}_{mol} & \\ & -d_e\mathcal{E}_{mol} \end{pmatrix} \\ &= Q_\parallel \, \mathbf{1} + Q_\perp \, \sigma_x + (\mu_\mathcal{N}\mathcal{B} + d_e\mathcal{E}_{mol}) \, \sigma_z \end{aligned} \tag{3.3}$$

in terms of the Pauli matrices. It can be immediately observed that the quadrupole interaction has two effects: first, it rotates the axis of the pseudo-magnetic field around which the two-state system's pseudo-spin precesses, leading to a loss of contrast; second, it increases the length of the pseudo-magnetic field, which adds phase offsets to the measurement.

The Zeeman splitting between $|m_J = \pm 1\rangle$ is $2\mu_\mathcal{N}\overline{\mathcal{B}}$ ($\sim 2\pi\times$ 200 Hz with a $\pi/2$ bias magnetic field). The matrix elements of the quadrupole Hamiltonian are

$$Q_\parallel = \frac{-1}{10} \, Q_{H,0} \, (\nabla\mathcal{E})_0, \;\; Q_\perp = \frac{-3}{5} \, Q_{H,2} \, (\nabla\mathcal{E})^*_2. \tag{3.4}$$

$Q_\parallel$ only leads to a common-mode shift and can be neglected. We will consider $Q_\perp$ to be the sole effect of the quadrupole interaction from now on. Note that $Q_\perp$ contains the component $(\nabla\mathcal{E})^*_2$, which is related to $\nabla_x\mathcal{E}_y$. Since the $\mathcal{E}_y$ component of the lab field itself arises due to geometrical imperfections from the main field $\mathcal{E}_z$, we expect this component of the field gradient to be very small. The quadrupole moment of the H state in ThO is unknown. An estimate of its size can be made using dimensional considerations as: $Q_H \sim ea_0^2 = 6.8$ mHz/(V/cm^2). Even with the large value $(\nabla\mathcal{E})^*_2$

[2]The quadrupole Hamiltonian for the states with $\mathcal{N} = -1$ is obtained by replacing $Q_{H,2}$ by $Q_{H,-2}$ in (3.4). The absolute values of these reduced matrix elements in the molecule-fixed frame are equal: $|Q_{H,2}|^2 = |Q_{H,-2}|^2$.

$= 1$ V/cm^2 therefore, the matrix element of the quadrupole Hamiltonian is $Q_\perp \approx 2\pi\times$ 4 mHz.

The initial state $|\psi_i\rangle$ is written in terms of the basis vectors as

$$\begin{pmatrix} c_1(0) \\ c_{-1}(0) \end{pmatrix} = \frac{1}{\sqrt{2}} \begin{pmatrix} 1 \\ 1 \end{pmatrix} \tag{3.5}$$

After precession for a duration τ, the state vector evolves into $|\psi_f\rangle$ given by:

$$\begin{pmatrix} c_1(\tau) \\ c_{-1}(\tau) \end{pmatrix} = U(\tau) \begin{pmatrix} c_1(0) \\ c_{-1}(0) \end{pmatrix} \tag{3.6}$$

Here

$$U(\tau) = V \begin{pmatrix} \exp(i\int_0^\tau \kappa\, dt) & \\ & \exp(-i\int_0^\tau \kappa\, dt) \end{pmatrix} V^\dagger \tag{3.7}$$

and we have defined

$$\begin{aligned} V &= \begin{pmatrix} \cos\theta/2 & -\sin\theta/2 \\ \sin\theta/2 & \cos\theta/2 \end{pmatrix} \\ \kappa &= \sqrt{Q_\perp^2 + (d_e\mathcal{E}_{int} + \mu_\mathcal{N}\mathcal{B})^2} \\ \tan\theta &= -\frac{Q_\perp}{d_e\mathcal{E}_{mol} + \mu_\mathcal{N}\mathcal{B}}. \end{aligned} \tag{3.8}$$

The amplitudes of $|\psi_f\rangle$ in the detection basis can be written as

$$\begin{pmatrix} c_X \\ c_Y \end{pmatrix} = \frac{1}{\sqrt{2}} \begin{pmatrix} 1 & 1 \\ 1 & -1 \end{pmatrix} \begin{pmatrix} c_1(\tau) \\ c_{-1}(\tau) \end{pmatrix} \tag{3.9}$$

and the asymmetry as

$$\mathcal{A} = \frac{|c_X|^2 - |c_Y|^2}{|c_X|^2 + |c_Y|^2}. \tag{3.10}$$

This can be evaluated to obtain

$$\mathcal{A} = \frac{Q_\perp^2}{Q_\perp^2 + (\mu_\mathcal{N}\mathcal{B} + d_e\mathcal{E}_{mol})^2} + \frac{(\mu_\mathcal{N}\mathcal{B} + d_e\mathcal{E}_{mol})^2}{Q_\perp^2 + (\mu_\mathcal{N}\mathcal{B} + d_e\mathcal{E}_{mol})^2} \cos(2\int_0^\tau \kappa\, dt). \tag{3.11}$$

The quadrupole interaction results in a (negligibly small) loss of contrast, by a factor smaller than $\sim 10^{-6}$ for the values of $Q_\perp$, $\mu_\mathcal{N}\mathcal{B}$ estimated above. Its effect on the precession phase $\phi = 2\int_0^\tau \kappa\, dt$ is what we will consider next. Since $Q_\perp \ll \mu_\mathcal{N}\mathcal{B}$, we can expand the square root in κ and write

$$\phi = 2\int_0^\tau dt\, \Big[\mu_\mathcal{N}\mathcal{B} + d_e\mathcal{E}_{mol} + \frac{Q_\perp^2}{2\mu_\mathcal{N}\mathcal{B}} + \mathcal{O}\Big(\frac{Q_\perp^4}{(\mu_\mathcal{N}\mathcal{B})^3}\Big)\Big]. \tag{3.12}$$

This expression can also be obtained using perturbation theory on the Hamiltonian in (3.3). Comparing this with (2.4), we find that the phase offset added due to the quadrupole interaction is

$$\overline{\phi}_{r,Q} = \frac{Q_\perp^2\tau}{\mu_\mathcal{N}\mathcal{B}}. \tag{3.13}$$

This phase offset is very small: $\overline{\phi}_{r,Q} \sim 1$ nrad. Further, it is quadratic in the field gradient $(\nabla\mathcal{E})_2$, and therefore does not result in an eEDM-like systematic. This can be intuitively understood using (3.3), where we see that the Zeeman shift term $\mu_\mathcal{N}\mathcal{B}$ appears along the diagonals of the Hamiltonian, and $Q_\perp$ appears in the off-diagonal terms. Therefore, in the limit when $Q_\perp \ll \mu_\mathcal{N}\mathcal{B}$, the quadrupole interaction affects the precession phase quadratically. In comparison, if the experiment was operated with $\mathcal{B} \leq 10$ μG, the axis on the Bloch sphere around which the superposition state $|\psi_i\rangle$ precesses would be dominated by the (local) axis of the electric field gradient. As the electric field gradient is not easy to measure in the apparatus, this could lead to worrisome effects. Therefore a small $\mathcal{B}$-field, in addition to being convenient for adding a bias phase, is also useful to suppress the effect of the quadrupole interaction.

3.1.2 Leakage currents

Compared to eEDM experiments with atoms and non-Ω-doublet molecules, the experiment with ThO has the advantage that small electric fields can be used to completely polarize the H state. This reduces the concern raised by the inevitable $\mathcal{E}$-correlated leakage currents and the $\mathcal{B}$-fields produced by them. In addition, the electric field plate assembly discussed in Section 5.2 is carefully designed to minimize leakage current paths. Here we estimate the size of the effect caused by leakage currents, for the sake of illustration.

From the geometry of the electric field plate assembly, the closest approach of a leakage current to the precession region is ~ 10 cm. At this distance, the $\mathcal{B}$-field produced by a leakage current is $\mathcal{B}_{leak} \sim 6$ fT/nA. The worst-case estimate, where

this $\mathcal{B}$-field acts over the entire precession path, leads to a phase offset $\overline{\phi_r} \approx 10$ nrad/nA that is linear in the $\mathcal{E}$-field. However, this phase offset is distinguishable from $\phi_{\mathcal{E}}$ since

1. It scales with the magnitude of the lab $\mathcal{E}$-field, unlike the phase due to the internal field $\mathcal{E}_{mol}$.[3]

2. It does not reverse sign under $\mathcal{N}$ reversal.

These features are sufficient to distinguish it from $\phi_{\mathcal{E}}$. Note also that, even with the large leakage current of 1 nA, the worst-case phase added by the leakage $\mathcal{B}$-field is still smaller than the targeted sensitivity of the experiment.

3.1.3 Stress-induced birefringence

Since the state preparation and detection lasers propagate through the glass $\mathcal{E}$-field plates, any birefringence in them that is linear in the $\mathcal{E}$-field could appear as a potential systematic. Mechanical stresses can cause the refractive indices of glass to be slightly different along one axis compared to a perpendicular axis. The stress-induced optical path difference δ through a glass slab of thickness d under a normal stress σ is approximately given by

$$\delta = K\ d\ \sigma \tag{3.14}$$

where a typical value of K is $\sim 2 \times 10^{-12}$ Pa^{-1} (Schott Catalog, SF-7 glass). The thickness of the $\mathcal{E}$-field plates is $d = 1.25$ cm. Stresses that are correlated with the $\mathcal{E}$-field can arise due to the coupling of stress-induced birefringence and the electrostatic stress between the electrodes applying the $\mathcal{E}$-field.

The normal stress due to electrostatic attraction between the plates is

$$\sigma = -\frac{1}{2}\epsilon_0 \mathcal{E}^2 \tag{3.15}$$

The stress is negative (i.e. it tends to draw the plates closer) and quadratic in $\mathcal{E}$. For any birefringence to be linear in $\mathcal{E}$ therefore, there has to be some effect involving non-reversing components.

[3] If the leakage current is ohmic, it scales linearly with $\mathcal{E}$. If it is (as is often the case) non-ohmic, then it scales with a polynomial dependence on $\mathcal{E}$. In either case, these have a different scaling with $\mathcal{E}$ compared to $\mathcal{E}_{mol}$.

As an upper bound to the $\mathcal{E}$-linear phase offset due to birefringence, the full contribution due to birefringence is evaluated. With $\mathcal{E} = 100$ V/cm, we find $\sigma \simeq 5 \times 10^{-4}$ Pa. The path difference is therefore $\delta \simeq 1 \times 10^{-15}$ cm from each of the field plates. At $\lambda = 900$ nm, this corresponds to an optical phase difference $2\pi\delta/\lambda = 7 \times 10^{-11}$ rad between the fast and slow axes. The actual systematic effect is smaller than this, and is therefore negligibly small in comparison with the targeted sensitivity of the experiment.

3.1.4 g-factor difference between Ω-doublets

It has been shown in [BHJD09, Ham10] that the magnetic moments of the $\mathcal{N} = \pm 1$ components of an Ω-doublet in an $\mathcal{E}$-field can be different from each other, with a difference that is linear in the $\mathcal{E}$-field applied to polarize the system. In the H state in ThO, it arises due to mixing between the $J = 1$ and $J = 2$ rotational levels. Using equation [3.43] from [Ham10] the fractional difference between the magnetic moments $\mu_{\mathcal{N}=+1}$ and $\mu_{\mathcal{N}=-1}$ in the H state is

$$\frac{\Delta\mu_{\mathcal{N}}}{\mu_{\mathcal{N}}} \approx \frac{3D_H|\mathcal{E}|}{10B} \approx 6 \times 10^{-3}, \tag{3.16}$$

where D_H is the molecule-fixed electric dipole moment of the H state and B is the rotational constant of the H state. The values $D_H = 2\pi\times$ 2.13 MHz/(V/cm), $\mathcal{E} =$ 100 V/cm, $B = 2\pi\times$ 10 GHz have been used in the above equation. This effect does not directly lead to any systematic effects, since the difference in magnetic moments is independent of the sign of the $\mathcal{E}$-field.

3.1.5 Motional fields

The $\vec{\mathcal{E}}, \vec{\mathcal{B}}$ fields applied in the lab frame are seen by molecules moving with a velocity $\vec{v}$, in the non-relativistic limit appropriate for the experiment, as the fields

$$\begin{aligned} \vec{\mathcal{B}}' &= \vec{\mathcal{B}} - \vec{v} \times \vec{\mathcal{E}}/c^2 = \vec{\mathcal{B}} + \vec{\mathcal{B}}_{mot} \\ \vec{\mathcal{E}}' &= \vec{\mathcal{E}} + \vec{v} \times \vec{\mathcal{B}} \quad = \vec{\mathcal{E}} + \vec{\mathcal{E}}_{mot}. \end{aligned} \tag{3.17}$$

Note some of their properties.

- The motional fields $\vec{\mathcal{E}}_{mot}\,(\vec{\mathcal{B}}_{mot})$ is non-reversing when $\vec{\mathcal{E}}\,(\vec{\mathcal{B}})$ is reversed.

- Due to the geometry of the experiment, $\vec{\mathcal{E}}_{mot}, \vec{\mathcal{B}}_{mot}$ are perpendicular to $\vec{\mathcal{E}}, \vec{\mathcal{B}}$ respectively. Since the main $\mathcal{E}, \mathcal{B}$-fields are $\hat{z}$-directed, these motional fields appear in the xy plane.

- For nominal values of parameters in the ThO experiment, $\vec{\mathcal{E}} = 100$ V/cm $\hat{z}$, $\vec{\mathcal{B}} = 25$ mG $\hat{z}$, $\overline{v}_x = 170$ m/s, we find that $\vec{\mathcal{E}}_{mot} \approx 4 \times 10^{-6}$ V/cm $\hat{y}$, $\vec{\mathcal{B}}_{mot} \approx -200$ nG $\hat{y}$. These are very small fields indeed.

Due to the fact that the perturbing fields are transverse, direct interactions between $H, J = 1$ $|m_J = \pm 1\rangle$ states due to these fields are strongly suppressed by the tensor Stark shift Δ_{st}. For example, a motional magnetic field $\vec{\mathcal{B}}_{mot} = \mathcal{B}_\perp \hat{x}$ leads to a an off-diagonal Zeeman shift between $|m_J = \pm 1\rangle$ which appears in 4th order of perturbation theory:

$$\Delta E^{\mathcal{N}}_{\pm 1} \sim \frac{(\mu_{\mathcal{N}} \mathcal{B}_\perp)^4}{\Delta^3_{st}} \sim 2\pi \times 10^{-35} \text{ Hz}, \tag{3.18}$$

using the parameters for the H state. This is a vanishingly small effect.

3.2 Dangerous combinations

In the real world, perverse combinations of harmless building blocks can lead to dangerous systematic errors. In this section, we attempt to combine some of the ingredients discussed so far to construct a systematic error that mimics the behavior of $\phi_{\mathcal{E}}$.

3.2.1 Polarization rotations and light shifts

Since the state preparation and detection bases are set by the polarization of the respective lasers, polarization rotations can add phase offsets. There are different kinds of rotations: rotations in the xy plane, and rotations in the xz, yz planes. The latter two can be analyzed as equivalent effects.

- **Rotations in the xy-plane**: We have already examined stress-induced birefringence effects that can cause such rotations. These rotations can arise for technical reasons, as uncontrolled offsets in the angle χ between the state preparation and detection lasers. If these are proportional to the sign of the $\mathcal{E}$-field, they can potentially appear as systematics. However, as long as the polarization control of the lasers and the control electronics for the $\mathcal{E}$-field are decoupled,

it is difficult to imagine ways in which the electric field influences the polarization of the lasers in a way that is proportional to the sign of $\mathcal{E}$ but not the magnitude.

- **Rotations in the xz-plane**: Consider a laser beam with an amplitude $\mathcal{E}_{L,0}$ and a polarization that has been set to be nominally along the $\hat{x}$ axis. Assume that the $\hat{k}$-vector of the laser is tipped from the $\hat{z}$-axis by an angle θ in the xz-plane, and therefore is not exactly perpendicular to the xy-plane (where the $\hat{z}$-axis is defined by the $\mathcal{E}$-field). Such rotations can arise either due to misalignment, or due to fundamental cross-polarization effects. Cross-polarization is a result of the vector nature of electromagnetic waves – a simple derivation is presented in Section A.6, where it is shown that the angle θ due to this effect is $\theta \sim x_0\lambda/w^2$ (x_0 is the x-width of the laser beam, w the beam waist and λ the wavelength of the laser).

In the coordinate frame corresponding to the molecule's quantization axis (which is set by the $\mathcal{E}$-field), the xz rotation makes the laser's electric field vector $\vec{\mathcal{E}}_L$ have the following components

$$\vec{\mathcal{E}}_L = \mathcal{E}_{L,0}\cos\theta\hat{x} + \mathcal{E}_{L,0}\sin\theta\hat{z}. \tag{3.19}$$

The first term corresponds to a reduced amplitude of the laser's $\mathcal{E}$-field that couples to the $H, J = 1, |m_J = \pm 1\rangle$ states. However, due to its dependence on $\cos\theta$, it only leads to a small reduction in the amplitude of the $\mathcal{E}$-field. If the laser beams have enough intensity so that the $H \to C$ state preparation and $H \to E$ detection transitions are saturated, this term has no effect on the measurement.

The second term requires more caution. Since it is $\hat{z}$-polarized, it couples the $H, J = 1, |m_J = \pm 1\rangle$ states to $|m_J = \pm 1\rangle$ states in the C, E electronic states. For the static electric fields typically used in the experiment ($\vec{\mathcal{E}} \sim$100 V/cm $\hat{z}$), this does not resonantly couple the $H, J = 1|m_J = \pm 1\rangle$ levels to any allowed transitions. It does however lead to off-resonant energy level shifts (light shifts/AC Stark shifts). The state preparation laser's frequency is detuned from resonance with the allowed $H, J = 1\ |m_J = \pm 1\rangle \to C, J = 1\ |m_J = \pm 1\rangle$ transition, by $\sim$ 100s of MHz (depending on the tensor Stark shift in the C state and the choice of $\mathcal{N}$ for the H and C states). Similarly, in the E state, the laser's frequency is detuned from resonance with the allowed $H, J = 1\ |m_J = \pm 1\rangle \to E, J = 1\ |m_J = \pm 1\rangle$ transition, by $\sim$ 20 GHz.

Since the detuning that enters this light shift is different for the $H, |m_J = \pm 1\rangle$ states (due to the differential Zeeman shift between the H state and the excited electronic C or E state), this can lead to a differential phase shift between $|m_J = \pm 1\rangle$. In addition, this phase shift can be dependent on $\mathcal{N}$, either due to technical errors in setting the frequency step of the laser to switch between $\mathcal{N} = \pm 1$ states, or due to the difference in the magnetic moment $\mu_{\mathcal{N}}$ for $\mathcal{N} = \pm 1$ states in a way that is dependent on the $\mathcal{E}$ field. Further, this detuning can have a dependence on the $\mathcal{E}$-field due to the tensor Stark shift in the H state.

We estimate the size of this effect now. We will perform the analysis with the C state in mind, since the detuning is smaller for the $H \to C$ transition, but the same kind of analysis can be used for the $H \to E$ transition. Let the transition dipole moment of the $H \to C$ transition be D_{HC}. We assume that the angle θ is small, and therefore so is the perturbing term in the Hamiltonian $H_{int} \approx -D_{HC}\mathcal{E}_{L,0}\theta$ that leads to the light shift, compared to the detuning Δ. The light shift $\Delta E_{\pm 1}$ for the $H, J = 1$ $|m_J = \pm 1\rangle$ states can be obtained using perturbation theory:

$$\Delta E_{\pm 1} = \frac{D_{HC}^2 \mathcal{E}_{L,0}^2 \theta^2}{\Delta_{\mathcal{N}} \pm \delta\mu_{\mathcal{N}} \mathcal{B}}. \tag{3.20}$$

Here $\Delta_{\mathcal{N}}$ is the detuning from the $\mathcal{B}$-field free position of $|m_J = \pm 1\rangle$ states and $\delta\mu_{\mathcal{N}}$ is the difference between the magnetic moments of the H state and the C state. Both these terms have been written with explicit $\mathcal{N}$ labels as reminders that they can be different for $\mathcal{N} = \pm 1$ states. Since the differential Zeeman shift is small compared to the detuning, we can expand the denominator in a Taylor series and obtain

$$\Delta E_{\pm 1} = \frac{D_{HC}^2 \mathcal{E}_{L,0}^2 \theta^2}{\Delta_{\mathcal{N}}} \Big(1 \mp \frac{\delta\mu_{\mathcal{N}} \mathcal{B}}{\Delta_{\mathcal{N}}}\Big). \tag{3.21}$$

The size of this effect is estimated using realistic parameters: $D_{HC}\mathcal{E}_L = 2\pi\times$ 10 MHz, $\theta = 1$ mrad, $\Delta_{\mathcal{N}} = 2\pi\times$ 100 MHz, $\delta\mu_{\mathcal{N}}\mathcal{B} = 2\pi\times$ 10 kHz in a $\mathcal{B}$-field of 10 mG (dominated by the magnetic moment of the C state). We find that

$$\Delta E_{\pm 1} = (2\pi \times 10^{-6} \text{ Hz})\, f(\mathcal{N}, \mathcal{E}) \times [1 - 10^{-4} g(\mathcal{N}, \mathcal{B}, \mathcal{E})] \tag{3.22}$$

where we have explicitly written dimensionless functions f, g to show the possible dependence of the light shift on $\mathcal{N}, \mathcal{B}, \mathcal{E}$.

The phase shift due to this light shift is suppressed since the light shifts are restricted to the regions where the lasers interact with the molecules. Over an interaction time $T_{laser} \sim 1$ mm$/\overline{v}_x = 6$ μs, the light shift leads to a phase offset between H $|m_J = \pm 1\rangle$ that is

$$\overline{\phi_r}_{LS} \sim (7 \times 10^{-11} \text{ rad})\, f(\mathcal{N}, \mathcal{E}) \times [1 - 10^{-4} g(\mathcal{N}, \mathcal{B}, \mathcal{E})]. \tag{3.23}$$

Hence, this phase offset is not problematic as it is small compared to the targeted sensitivity of the experiment.

3.2.2 Non-reversing $\mathcal{E}$-fields & g-factor difference

Off-resonant energy shifts can be a bothersome source of eEDM-like systematics, especially in experiments where the electric field $\mathcal{E}_{mol}$ experienced by the eEDM can only be reversed using the laboratory electric field. In such experiments, any phase offsets $\overline{\phi_r}$ that are linear in the lab electric field can appear to mimic an eEDM-induced phase $\phi_{\mathcal{E}}$. However, ThO has the advantage that the Ω-doubling in the H state allows the internal field $\mathcal{E}_{mol}$ to be reversed by reversing $\mathcal{N}$ (e.g. by moving the state preparation and detection lasers in frequency), without changing anything to do with the lab electric field. This is a powerful feature that allows the separation of $\mathcal{E}$-linear phase offsets from $\phi_{\mathcal{E}}$.

The effect of such perturbations is conveniently treated using the formalism developed in Section B.8. The energy shift due to $\mathcal{E}, \mathcal{B}$-fields leading to the geometric phase is shown there to be identical for states with $\mathcal{N} = \pm 1$, as long as the detuning, electric dipole moment and magnetic moment are identical. Here we construct a potential systematic error that might arise due to the fact that the magnetic moments are not identical. The $\mathcal{E}$-field part of (B.61) for the energy shift between $|m_J = \pm 1; \mathcal{N}\rangle$ is

$$\Delta E^{\mathcal{N}}_{\pm 1} = \frac{1}{2}\Big[\frac{d^2_{\perp,\mathcal{N}}\mathcal{E}^2_\perp}{\Delta_{st,\mathcal{N}} + \mu_{z,\mathcal{N}}\mathcal{B}_z - \omega^E_\perp} - \frac{d^2_{\perp,\mathcal{N}}\mathcal{E}^2_\perp}{\Delta_{st,\mathcal{N}} - \mu_{z,\mathcal{N}}\mathcal{B}_z + \omega^E_\perp}\Big]. \tag{3.24}$$

Explicit dependences on $\mathcal{N}$ have been indicated for parameters that could be different for $\mathcal{N} = \pm 1$ states. We make the simplifying assumption that $\Delta_{st,\mathcal{N}} \approx d^2_\parallel \mathcal{E}^2_z$, and that $d_{\perp,\mathcal{N}} = d_\perp$. This leaves just the magnetic moments to be dependent on $\mathcal{N}$. The

energy shift becomes

$$\Delta E^{\mathcal{N}}_{\pm 1} \approx -\Big(\frac{d_\perp \mathcal{E}_\perp}{d_\parallel \mathcal{E}_z}\Big)^2 (\mu_{z,\mathcal{N}} \mathcal{B}_z - \omega^E_\perp). \tag{3.25}$$

The $\mathcal{N}$ dependence of the magnetic moment is: $\mu_{z,\mathcal{N}} = \mu_{z,0} + \mathcal{N}\gamma|\mathcal{E}_z|$, where $\gamma = \mu_{z,0}\frac{3d_\parallel}{20B}$ following (3.16). Therefore we have

$$\Delta E^{\mathcal{N}}_{\pm 1} = -\Big(\frac{d_\perp \mathcal{E}_\perp}{d_\parallel \mathcal{E}_z}\Big)^2 (\mu_{z,0}\mathcal{B}_z - \omega^E_\perp + \mathcal{N}\gamma|\mathcal{E}_z|\mathcal{B}_z). \tag{3.26}$$

We ignore the geometric phase term $\omega^E_\perp$ and the $\mathcal{N}$-independent Zeeman shift term $\mu_{z,0}\mathcal{B}_z$, and focus our attention on the $\mathcal{N}$-odd energy shift ΔE_{gf}.

$$\begin{aligned} \Delta E_{gf} &= -\Big(\frac{d_\perp \mathcal{E}_\perp}{d_\parallel \mathcal{E}_z}\Big)^2 (\mathcal{N}\gamma|\mathcal{E}_z|\mathcal{B}_z) \\ &= -\frac{(d_\perp \mathcal{E}_\perp)^2}{d_\parallel^2 |\mathcal{E}_z|}(\mathcal{N}\gamma\mathcal{B}_z). \end{aligned} \tag{3.27}$$

This term is nominally even under $\mathcal{E}$-reversals, but a combination of reversing and non-reversing transverse components can make a difference. We write the transverse electric field vector as $\vec{\mathcal{E}}_\perp = \vec{\mathcal{E}}^r_\perp + \vec{\mathcal{E}}^{nr}_\perp$ to denote reversing and non-reversing components respectively. A reversing transverse field $\vec{\mathcal{E}}^r_\perp$ could arise, for example, due to non-parallelism of the electric field plates. A non-reversing transverse field $\vec{\mathcal{E}}^{nr}_\perp$ could arise from technical sources, such as offsets in the voltages applied to the plates, or due to effects such as patch potentials.

We ignore $\mathcal{E}$-even terms and focus on the (effectively) $\mathcal{E}$-odd cross term between reversing and non-reversing components, which leads to the energy shift

$$\Delta E_{gf} = -\mathcal{N}\Big(\frac{d_\perp}{d_\parallel}\Big)^2 \Big(\frac{\vec{\mathcal{E}}^r_\perp \cdot \vec{\mathcal{E}}^{nr}_\perp}{|\mathcal{E}_z|}\Big)(2\gamma\mathcal{B}_z), \tag{3.28}$$

and the phase shift

$$\overline{\phi}_{gf} = \mathcal{N}\Big(\frac{d_\perp}{d_\parallel}\Big)^2 \Big(\frac{\vec{\mathcal{E}}^r_\perp \cdot \vec{\mathcal{E}}^{nr}_\perp}{|\mathcal{E}_z|}\Big)(2\gamma\mathcal{B}_z\tau). \tag{3.29}$$

This is a potentially dangerous systematic. Note its properties:

- It is odd under $\vec{\mathcal{E}}$-reversal.

- It does not scale with the magnitude of $\vec{\mathcal{E}}$, due to the appearance of the "geometric" term $\vec{\mathcal{E}}_\perp^r/|\mathcal{E}_z|$.

- It is odd under $\mathcal{N}$-reversal.

It can be distinguished from $\phi_\mathcal{E}$ only by its linear dependence on $\mathcal{B}$. Further, there is a part of $\overline{\phi}_{gf}$ that is independent of the $\mathcal{B}$-field in the lab, since there are inevitable offsets in the magnetic field. These can arise from offsets in the current supplies and due to incomplete suppression of the ambient field in the lab by the magnetic shields. Having constructed this potential systematic, it remains to evaluate its size.

We use the following parameters:

- $\mathcal{E}_z = 100$ V/cm, $\mathcal{E}_\perp^{nr} = 10$ mV/cm, $\mathcal{E}_\perp^{nr} = 10$ mV/cm. The reversing and non-reversing transverse components are assumed to be collinear, to obtain a worst-case estimate. Reversing and non-reversing components at this level are not unreasonable to expect, based on the alignment of the field plates and plausible non-reversing potentials on the plates.

- $\mu_{z,0} = 2\pi\times$ 11.33 kHz/G,
  $d_\parallel \approx d_\perp \approx 2\pi\times$ 2.13 MHz/(V/cm),[4]
  $B = 2\pi\times$ 9.8 GHz, the rotational constant for the H state
  $\gamma = \mu_{z,0}\frac{3d_\parallel}{20B} \approx 2\pi \times 0.37$ Hz/(G V/cm)
  $\mathcal{B}_z = 10$ mG
  $\tau = \mathrm{L}/\overline{v}_x = 1.3$ ms.

With these parameters, (3.29) can be evaluated to obtain $\overline{\phi}_{gf} \lesssim \mathrm{sgn}(\vec{\mathcal{E}})\cdot\mathrm{sgn}(\mathcal{N})\ 10^{-10}$ rad. While it has the correct symmetries to mimic an eEDM, its magnitude is much smaller than the targeted uncertainty of the ThO eEDM experiment.

In conclusion, we note that mixed-origin terms such as this one are likely to be the leading sources of systematic errors in the experiment. A couple of the most plausible sources have been examined in this chapter and it has been found that, with conservative estimates of the parameters involved, they do not lead to a systematic error at the level of the statistical sensitivity that is foreseeable in an eEDM experiment with ThO.

[4]See Chapter 4 for details regarding the measurement of the electric and magnetic dipole moments.

Chapter 4

Measurements

> "I think we just look," he said. "We find what we find. Then we think about it."
>
> Joe Leaphorn, *A Thief of Time*

This chapter describes some measurements that were made along the way as inputs for the design of the EDM apparatus, and for estimating the statistical sensitivity and size of systematic effects in the experiment.

4.1 Production of ThO beams

One of the standard approaches to the production of buffer gas cooled beams of thermodynamically unstable molecules (such as ThO) is by dissociation of a stable precursor. In the case of ThO, the convenient stable precursor is thorium dioxide (ThO_2). It is a thermal and electrical insulator, and can be made into a tough ceramic by standard ceramic powder processing methods [BVK+88]. However, ThO_2 has a high melting point ($\sim$ 3600 K) and low vapor pressure at any reasonably attainable temperatures. Pulsed laser ablation of ThO_2 using focused nanosecond pulses (which can dissociate the target material non-thermally) is a convenient means of directly producing ThO. This method has been the mainstay of our work with ThO so far.

The cryogenic beam source for the ThO EDM experiment has been extensively optimized and characterized by the Doyle group. In its latest incarnation the buffer gas that is used is neon, which has the advantage over helium that it can be easily cryo-pumped at $\sim$ 10 K in the cryogenic source chamber and the cryo-pumping maintained for a long time without requiring regular bakeouts. In spite of the rather high

temperature of a neon-based production cell ($\sim$ 17 K),[1], rotational cooling obtained during supersonic expansion out of the cell into the beam region cools the molecules to a rotational temperature of $\sim$ 3 K. As the starting temperature for the supersonic expansion is much lower ($\sim$ 17 K compared to $\sim$ 300 K for standard supersonic beam sources), low final temperatures can be obtained without the high backing pressure and gas pumping requirements of standard supersonic beam sources. A detailed characterization of the cryogenic ThO beam source is presented in [HPG$^+$11], and a description of a closely related cryogenic beam source is in [BSD11].

In this Section, some early measurements of ThO production and molecular beam yield are presented, purely for reference. They have since been superseded by the more extensive characterization in [HPG$^+$11] and other unpublished measurements.

Figure 4.1 shows one of the first measurements of ThO produced by laser ablation in a closed cell filled with helium buffer gas. ThO molecules produced by the ablation were monitored by CW laser absorption at 613 nm on the strong $X, v = 0, J_i = 1 \rightarrow E, v = 0, J_f = 0$ $P(1)$ line. An absorption fraction of $\eta \approx 60\%$ was consistently obtained at a helium stagnation density of $n_{He} \sim 10^{16}/\mathrm{cm}^3$ using 10 mJ pulses of 532 nm Nd:YAG laser light focused by an f/10 lens onto a sintered ThO_2 ceramic target. This absorption fraction η can be turned into a measurement of the density n_{ThO} of ThO molecules in the $X, v = 0, J = 1$ state, using an estimate of the absorption cross-section σ_0 and the length ℓ of the column of molecules traversed by the laser, by the formula

$$n_{ThO} = -\frac{\log(1-\eta)}{\sigma_0 \ell}. \tag{4.1}$$

The cross section for a Doppler-broadened line between two molecular states, the initial state with angular momentum J_i and the final state with angular momentum J_f, at a resonant wavelength λ is [BKD08]

$$\sigma_0 = \frac{2J_f+1}{2J_i+1}\frac{\lambda^2}{4\sqrt{\pi}}\frac{\gamma_p}{\Gamma_D} \tag{4.2}$$

where γ_p is the partial linewidth for the transition being probed and $\Gamma_D = 2\pi v_{th}/\lambda = 2\pi \times 30$ MHz is the calculated Doppler width of the transition at 5 K. If τ is the lifetime of the excited state used in the transition, and BR = EBF $\times$ FCF $\times$ RBF is the branching ratio (a product of the electronic branching fraction EBF, the

[1]This temperature is required to obtain a buffer gas density of $\sim 10^{16}/\mathrm{cm}^3$ of neon in the production cell, in order to thermalize the ThO molecules before they exit the cell.

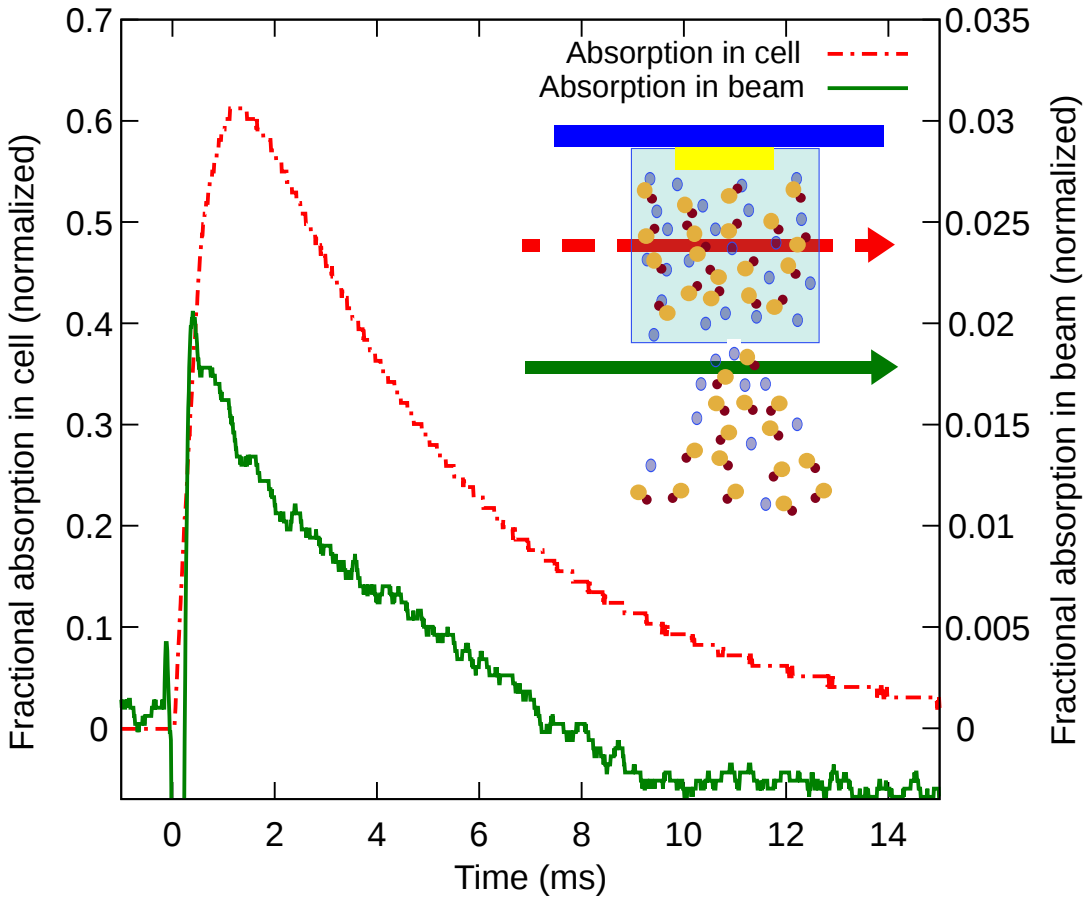

Figure 4.1: Absorption measurements of ThO molecules in the $X, V = 0, J = 1$ state, inside the buffer gas cell and outside, simultaneously probed using absorption on the $P(1)$ line of the $X \to E$ transition at 16 318.30 cm^{-1}.

Franck-Condon factor FCF describing the vibrational branching ratio, and the rotational branching fraction RBF) for the rovibrational transition used, then the partial linewidth is $\gamma_p = \mathrm{BR}/\tau$.

Figure 4.1 shows two absorption traces, one measured inside the cell and one measured $z = 2$ mm away from the cell aperture in the mini-beam apparatus MB1.[2] For the $P(1)$ line that was used, RBF = 1 (calculated using Equation A.16), FCF = 0.87 [WS72] and EBF ≈ 1 (based on the E state's spin-orbit content in [KDSP94]). The lifetime of the E state in ThO is unknown. I estimate the lifetime of the E state based the following: a) the E state has 50% (probability) $^1\Sigma$ content [KDSP94], b) the estimated dipole matrix element for a fully allowed $^1\Sigma \rightsquigarrow {}^1\Sigma$ transition is $\sim ea_0$. Therefore, $D_{EX} \approx 0.7ea_0$, leading to the estimated lifetime $\tau = 300$ ns (using Fermi's

[2]The "mini-beam" molecular beam sources are described in Chapter 5.

Golden Rule). The resulting absorption cross section for the $P(1)$ line is

$$\sigma_0 = \frac{1}{3}\frac{(613\text{ nm})^2}{4\sqrt{\pi}} \times \frac{0.87}{2\pi \times 300\text{ ns} \times 30\text{ MHz}} = 8 \times 10^{-12}\text{ cm}^2 \tag{4.3}$$

which yields a peak ThO density $n_{ThO} = 4.5 \times 10^{10}/\text{cm}^3$, using the distance from the target to the probe laser as the size of the cloud of molecules, $\ell = 2.5$ cm. This is the density of molecules in the $X, v = 0, J_i = 1$ state, which has $\approx 23\%$ Boltzmann fraction of the population at 5 K. The total density of molecules (summed over rotational states) calculated using the $X \rightarrow E$ absorption signal inside the cell is $n_{ThO,\text{cell}} = 2 \times 10^{11}/\text{cm}^3$.

The beam apparatus is operated at a helium flow rate $f_{He} = 10$ sccm (standard cubic centimeters per minute) $\simeq 4 \times 10^{18}$ atoms/s. The peak absorption fraction measured outside the cell aperture is $\sim 2\%$, which yields a peak density $n_{ThO,\text{beam}} = 1.7 \times 10^{10}/\text{cm}^3$ (assuming the same Doppler width as the inside of the cell, summed over all rotational states). The density of ThO molecules outside the aperture $n_{ThO,\text{beam}}$ can be used to estimate the emission rate $\dot{N}_{\text{beam}}$, using the area of the cell aperture that was used ($A = 6$ mm $\times$ 1 mm) and the forward velocity $v_\parallel \approx$ 160 m/s (using data from [BSD11] for a similar beam source at $f_{He} = 10$ sccm), in the relation

$$\dot{N}_{\text{beam}} = \alpha\ n_{ThO,\text{beam}}\ v_\parallel A. \tag{4.4}$$

Here α is a quantity of order unity that depends on the hydrodynamics of the flow of buffer gas out of the cell into the vacuum outside.[3] Assuming $\alpha = 1$ this yields an estimate of the peak molecule emission rate $\dot{N}_{\text{beam}} \approx 1.6 \times 10^{13}/\text{s}$. The pulse of molecules lasts ~ 3 ms, yielding $N_{\text{beam}} \approx 5 \times 10^{10}$ molecules/pulse emitted into the beam in the X state (summed over all rotational states).

4.2 Lifetime of the H state

The lifetime of ThO in the metastable H state was measured using a closed cryogenic buffer gas cell. The cell used for this measurement had no aperture and no flow of helium gas. The cell was filled with between 40-800 mTorr of helium gas at 5 K and laser ablation in the buffer gas environment produced $\sim 10^{11}$ ThO molecules

[3] $\alpha = 1/4$ for an effusive beam. $\alpha = 1$ for fully developed flow along a streamline [LL87]. The value of α for entrained hydrodynamic flow is expected to be close to the value for fully developed flow.

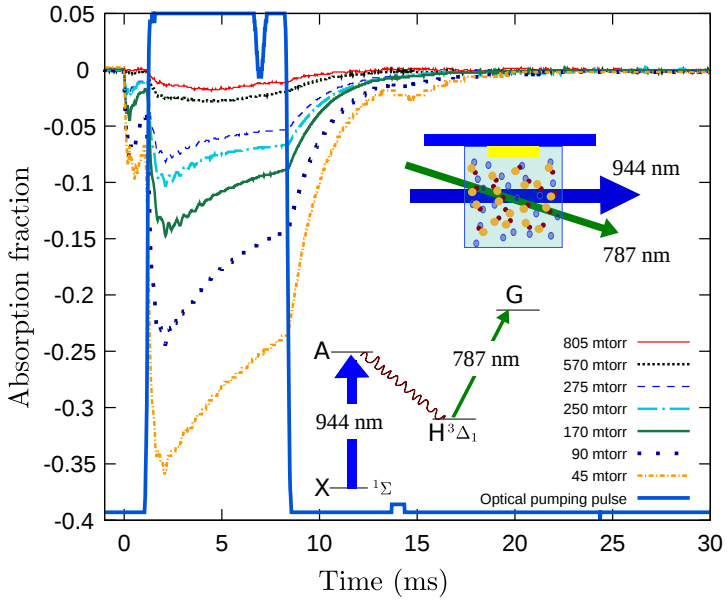

(a) R(1) line decay curves

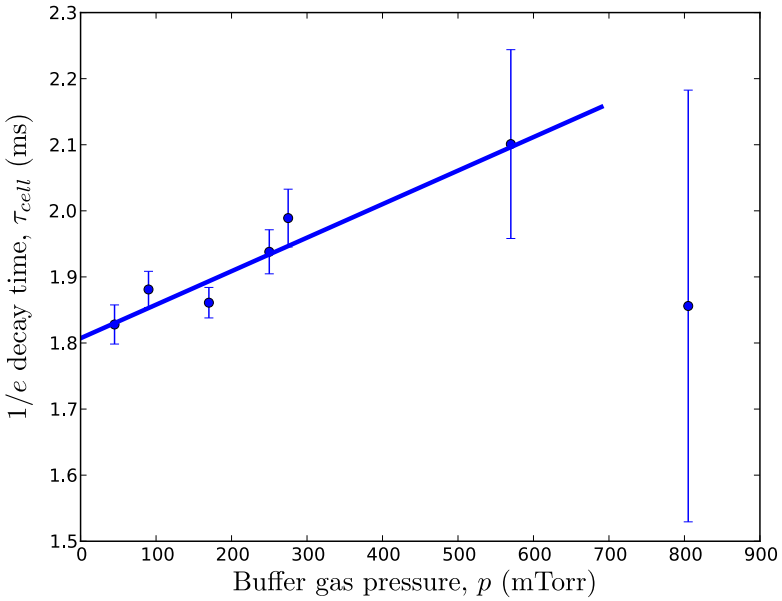

(b) Fit lifetimes vs. buffer gas pressure

Figure 4.2: The H state population was monitored by laser absorption on the $H \rightarrow G$ transition. The probe laser was overlapped inside the buffer gas cell with an optical pumping beam exciting the $X \rightarrow A \rightsquigarrow H$ transition. a) Absorption curves measured on the $H, v = 0 \rightarrow G, v = 0$ R(1) line. Each trace is an average of the signal from 64 ablation laser shots. b) Lifetimes were derived from exponential fits to the decay of the absorption signal after the optical pumping was shuttered off. (The data point at 805 mTorr was not used in the fit as it yielded an anomalously low lifetime, likely due to collisional effects from the buffer gas, and had a large uncertainty.) A linear extrapolation to zero pressure yielded $\tau_{cell}(p = 0) = 1.81(3)$ ms.

in the ground X state. Molecules from the $X, v = 0, J = 1$ state were optically pumped into the H state via the A state. The cell was illuminated with a laser tuned to the $X, v = 0, J = 1 \rightarrow A, v' = 0, J' = 0$ $P(1)$ line at 10 600.15 cm^{-1}, for a variable duration. (Approximately 4% absorption fraction was observed on the $X \rightarrow A$ transition.) Molecules in the H state were probed by laser absorption on the $H, v = 0, J = 1 \rightarrow G, v'' = 0, J'' = 2$ $R(1)$ line at 12 694.58 cm^{-1}. Optical pumping into the H state was observed only when the pump and probe lasers were overlapped inside the cell. The diameter of the optical pump $X \rightarrow A$ laser ($\sim$ 10 mW) was expanded to 7 mm, while the $H \rightarrow G$ probe laser ($\sim$ 1 μW) had a 0.5 mm diameter beam and was aimed near the center of the pump laser beam.[4] We observed in initial measurements that the H state was continuously repopulated, at a low level, following the ablation pulse. This is probably due to radiative or collision-induced decays from higher-lying electronic states and/or vibrational levels populated during the ablation pulse, although the shelf states were not unambiguously identified. To eliminate errors due to this repopulation, we only analyzed the transient decay of optically pumped molecules in the H state after the optical pumping beam was rapidly extinguished. A shutter, built using an audio voice coil, extinguished the $X \rightarrow A$ pump laser beam in < 500 μs. Exponential fits to the decay, in the time window immediately after the pump laser was switched off, were used to extract lifetimes in the cell, τ_{cell}. The lifetimes were measured at a number of different buffer gas pressures, as shown in Fig.4.2, and an increasing trend for the lifetime versus the buffer gas pressure was observed. In addition to the effects of diffusion (which are accounted for by the large pump volume which envelopes the probe volumes), the buffer gas can have two effects – quenching (which depopulates the H state, and decreases the apparent lifetime) and repopulation from shelf states (which increases the apparent lifetime). From the buffer gas pressure dependence in the plot in Fig.4.2, it appears that (net) repopulation effects are at work. Therefore, the observed decay lifetimes were extrapolated to zero buffer gas pressure and the value at zero pressure, $\tau_{cell}(p = 0)$, is reported here. This procedure yielded $\tau_{cell}(p = 0) = 1.81(3)$ ms for the $R(1)$ line. The same procedure yielded $\tau_{cell}(p = 0) = 1.74(1)$ ms for the $R(2)$ line.

[4]This arrangement was used in order to mitigate the systematic effect of diffusion, where the diffusion of optically pumped molecules out of the probe laser beam can affect the apparent lifetime. With the optical pump beam expanded to be larger than the probe beam, the loss of optically pumped molecules out of the probe beam's volume is expected to be balanced by the influx of optically pumped molecules into the probe beam's volume. With a helium density $n_{He} = 1.6 \times 10^{17}$/cm^3 ($\equiv$ 100 mTorr at 5 K) and an assumed helium-ThO diffusion cross section of $\sigma_D = 5 \times 10^{-15}$ cm^2, the dwell time of molecules within the probe laser's volume is $\sim$ 1 ms.

In the absence of a model for why these two values should differ, we consider this difference as the systematic error in the measurement. The total error is considered to be this systematic error added in quadrature with the fit uncertainties. The final result is $\overline{\tau}_{cell}(p = 0) = 1.8(1)$ ms. In the absence of repopulation effects in the buffer gas cell that persist for pathologically long times, this value should be the radiative lifetime τ_H of the H state.

4.3 Magnetic and electric dipole moments of the H state

[5]The advantages of the suppressed magnetic moment, as well as the Ω-doublet structure and large polarizability, of the $H\ ^3\Delta_1$ state have been described in Chapter 1. Measurements of the magnetic moment μ_H and the molecule-fixed electric dipole moment D_H are described here. The measurements were carried out using a molecular beam of ThO, produced in the mini-beam apparatus MB2 described in Section 5.1, probed at a distance of 30 cm from the cell aperture. The lowest rovibrational level in the H state $(H, v = 0, J = 1)$ was populated by optical pumping from the ground electronic $X\ ^1\Sigma^+, v = 0, J = 1$ state via the $A\ ^3\Pi_{0^+}, v = 0, J = 0$ state. It was subsequently probed a few mm downstream by exciting laser-induced fluorescence (LIF) on the $H, v = 0, J = 1 \rightarrow E, v = 0, J = 0 \rightsquigarrow X$ transition at 908 nm. Both the 943 nm light to drive the $X \rightarrow A$ pump transition and the 908 nm light for the $H \rightarrow E$ probe transition were derived from external cavity diode lasers (DL Pro, Toptica). Fluorescence from $E \rightsquigarrow X$ at 613 nm was collected with an f/1.0 lens, channeled through a ϕ1 in. × 12 in. long quartz lightpipe and a bandpass interference filter (FB610, Thorlabs) and monitored with a photomultiplier tube (H6780-20, Hamamatsu). The pump and probe lasers were perpendicular to the molecular beam and the transverse Doppler width on the $H \rightarrow E$ probe transition was ~ 5 MHz. With the pump laser locked to resonance, the probe laser's frequency was tuned. The frequency steps were calibrated by monitoring the laser's transmission through a scanning confocal interferometer, which was actively stabilized to a 1064 nm YAG laser (in turn locked to an iodine cell) [Far07]. The free spectral range of the interferometer was independently measured by two methods, a) from a measurement its length, and b) from measurements of spectra with RF sidebands added to the

[5]This section is based on [VSG+11].

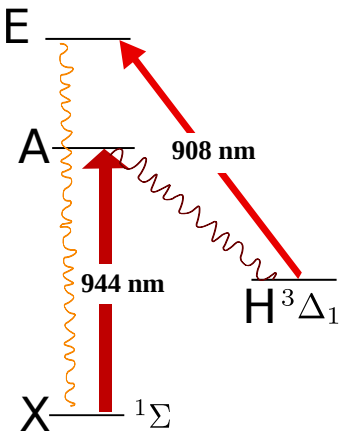

Figure 4.3: Levels and transitions used in the measurement of the electric and magnetic moments of the H state. Molecules were optically pumped into the H state using the $X \to A$ transition at 943 nm. The structure of the H state in the electric and magnetic fields was probed using laser-induced fluorescence (excitation using $H \to E$ at 908 nm, photons emitted from $E \rightsquigarrow X$ at 613 nm).

laser by current modulation [Gur11]. The frequency of the lasers was stepped using piezoelectric actuators mounted on the grating. The voltage to frequency conversion factor for the piezos obtained by the two methods (a) and (b) disagreed by 1%. This is considered as the systematic error in the frequency calibration.

4.3.1 Magnetic dipole moment

The size of the g-factor estimated before the measurement was $\sim$ 0.01-0.1 μ_B ($\sim$ 10-100 kHz/G), based on the spin-orbit admixture data for the H state in [PNH$^+$03]. Initial attempts to split the zero-field resonance line using a $\mathcal{B}$-field of up to 70 G (provided by a 100 turn coil) did not succeed. So a compact permanent magnet assembly using NdFeB magnets[6] was constructed in order to provide a larger $\mathcal{B}$-field. It consists of 8 magnets, each 0.125 in. x 0.125 in. x 1 in. arranged with their poles as shown in Fig.4.4. This geometry was chosen in order to obtain a uniform $\mathcal{B}$-field, while allowing access for the molecular beam, probe laser and light collection optics along three mutually perpendicular directions. The separation and alignment of the magnets was adjusted using spacing screws to obtain a uniform magnetic field over the region probed by the laser. After assembly, the permanent magnets (which are

[6] A useful trick for assembling permanent magnets in unstable configurations: if assembled on the surface of a (steel) optics table, they tend to stay in place during assembly, even if adjacent pairs of magnets strongly repel/attract each other.

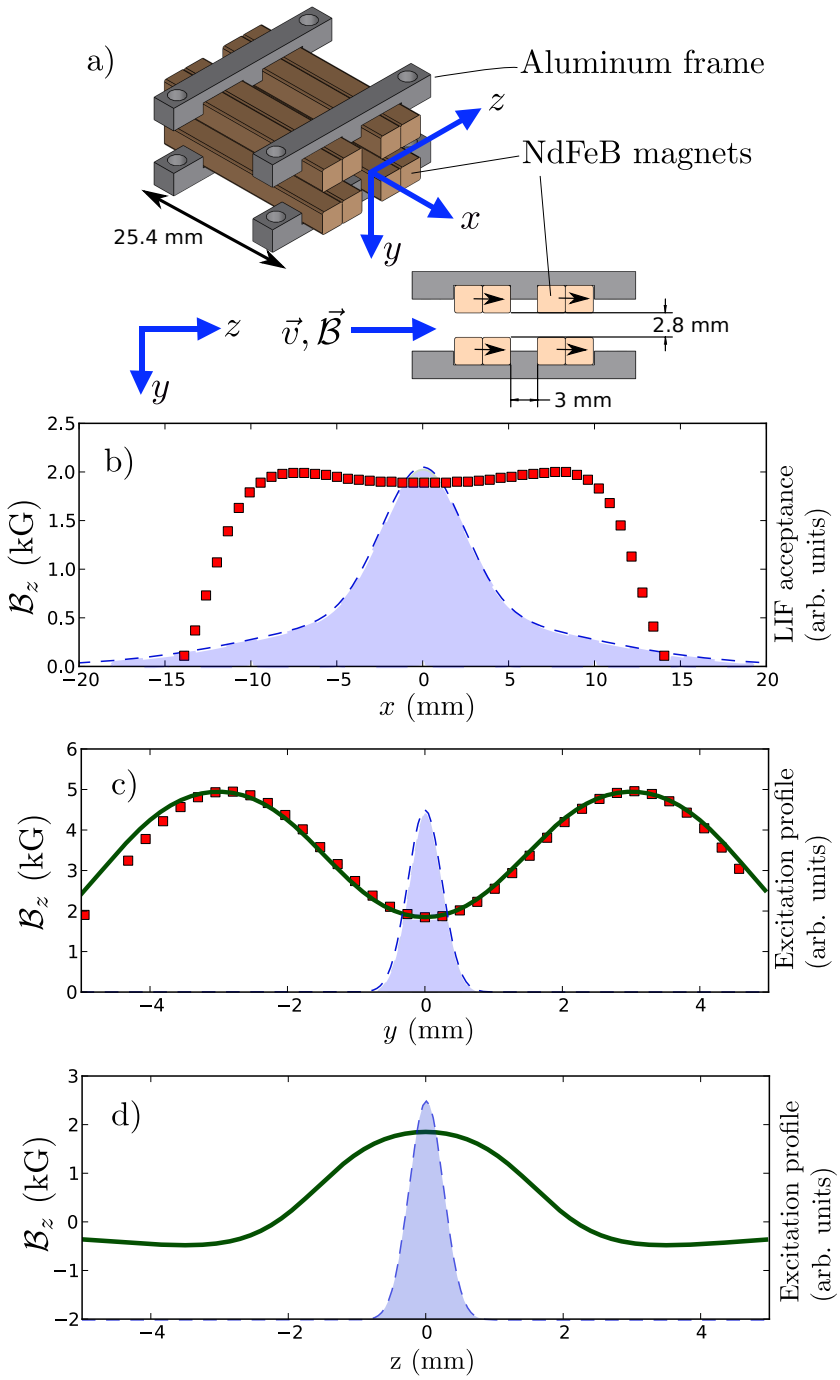

Figure 4.4: a) The magnet assembly used in the measurement of μ_H. Arrows on the NdFeB magnets indicate the direction of magnetization. b) The $\hat{z}$ component of the $\mathcal{B}$-field, $\mathcal{B}_z$, measured along the x-axis. The shaded area indicates the calculated acceptance of the LIF detection optics. c) Measured (red squares) and calculated (solid green line) values of $\mathcal{B}_z$ along the y-axis. The shaded area indicates the LIF excitation region, defined by the probe laser's intensity profile. d) Calculated values of $\mathcal{B}_z$ along the z-axis. The shaded area indicates the probe laser's intensity profile.

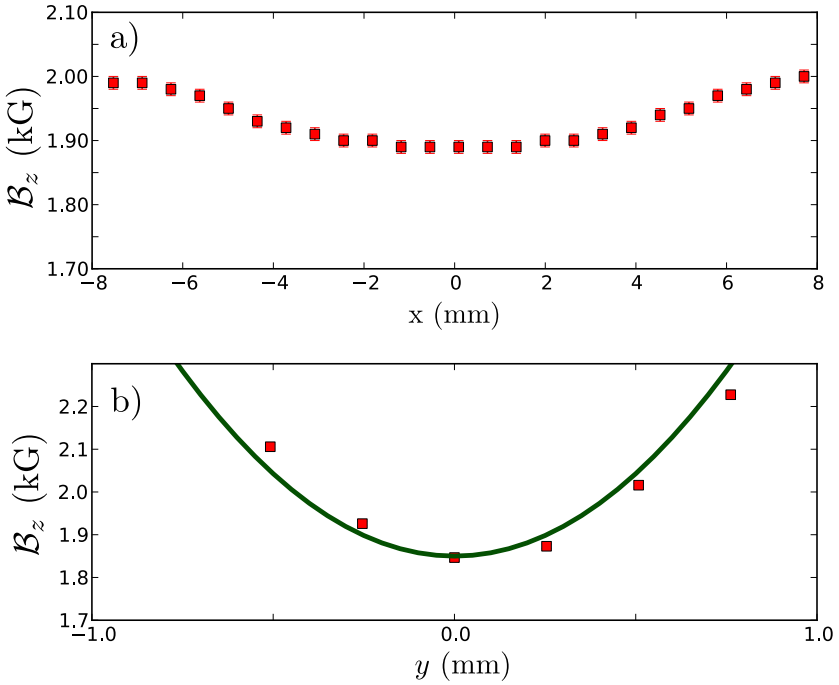

Figure 4.5: a) Zoom in on the center of curve in Fig.4.4b. b) Zoom in on the center of the curve in Fig.4.4c. The calculated curve is the solid green line.

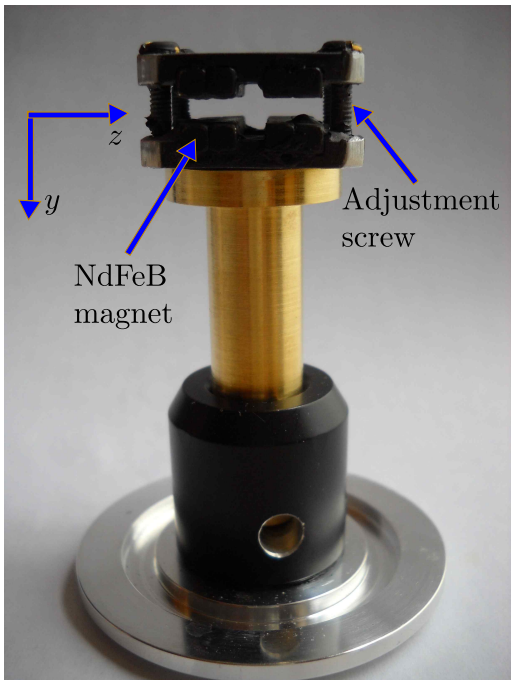

Figure 4.6: Photograph of the magnet assembly, mounted on a KF40 flange. The view is along the direction of propagation of the probe laser ($\hat{x}$-axis in Fig.4.4a).

usually nickel coated to prevent corrosion) were sprayed with flat black chalkboard paint (7704T162, McMaster-Carr) to reduce laser light scatter, and baked at 70 ^{o}C in vacuum to reduce outgassing from the paint.[7] The magnet assembly was epoxied onto a ϕ0.5 in. brass post, which was mounted in a standard aluminum optics post holder, in turn mounted onto a KF40 vacuum flange. This arrangement allowed us to conveniently insert and orient the magnets in the KF40 6-way cross which formed the probe region. The magnet was oriented so that $\vec{\mathcal{B}} \parallel \vec{v}$, the velocity of the molecular beam, in order to avoid spurious effects due to motional electric fields ($\vec{\mathcal{E}}_{mot} = \vec{v} \times \vec{\mathcal{B}}$) polarizing the molecular state. About 120 mW of probe laser power was collimated (intensity FWHM = 0.6 mm) to spatially select a well-defined region near the center of the magnet assembly;[8] The k-vector of the probe laser was aligned along $\hat{x}$ in Fig.4.4a. The polarization $\hat{\epsilon}$ of the probe laser was adjusted to be parallel (perpendicular) to the $\mathcal{B}$-field in order to probe the unshifted $m_J = 0$ (Zeeman-shifted $m_J = \pm 1$) states. The LIF collection lens was epoxied (using optically transparent Epo-tek 301) to the end of a 1 in. quartz lightpipe, which was fed into vacuum through a 1 in. quick-disconnect feedthrough on a KF40 flange. The lens and lightpipe were along the $\hat{y}$ direction in Fig. 4.4a. The distance of the lens from the center of the magnet was set to be equal to its focal length, f = 25.4 mm.

The spectra of LIF collected from the $H, J = 1$ state in the magnetic field region are shown in Fig. 4.7. Spectra with $\hat{\epsilon} \parallel \vec{\mathcal{B}}$ and $\hat{\epsilon} \perp \vec{\mathcal{B}}$ were simultaneously fit to a sum of 3 gaussian lineshapes using a nonlinear least squares routine. As these routines can only use y-error bars for the optimization, the x-error bars (which are not negligible) were converted into equivalent y-error bars using the slope of the data trace (numerically evaluated from adjacent pairs of data points and smoothed over a neighborhood of 4 points). These derived y-error bars were added in quadrature with the bare y-error bars. The line centers and linewidths were constrained to have the same value for both data sets. We included 'minority' peaks corresponding to the orthogonal polarization (i.e. the $m_J = 0$ peak in the $\hat{\epsilon} \perp \vec{\mathcal{B}}$ fit, and the $m_J = \pm 1$ peaks in the $\hat{\epsilon} \parallel \vec{\mathcal{B}}$ fit) to model the effect of elliptical polarization (due to an imperfect waveplate and birefringence in vacuum windows). The measured ratio of unwanted to desired polarization ($\approx 15\%$) was in fair agreement with that deduced from the

[7] A higher temperature than this was avoided in order to leave the permanent magnets unaffected. They have a Curie temperature of ~ 100 ^{o}C. The field profiles of the magnet assembly shown in Figure 4.4 were measured after the bakeout.

[8] The saturation intensity of the $H \rightarrow E$ transition was measured by Ben Spaun to be ~ 1 W/cm^2. The intensity in the probe laser beam is estimated to be 0.4 W/cm^2.

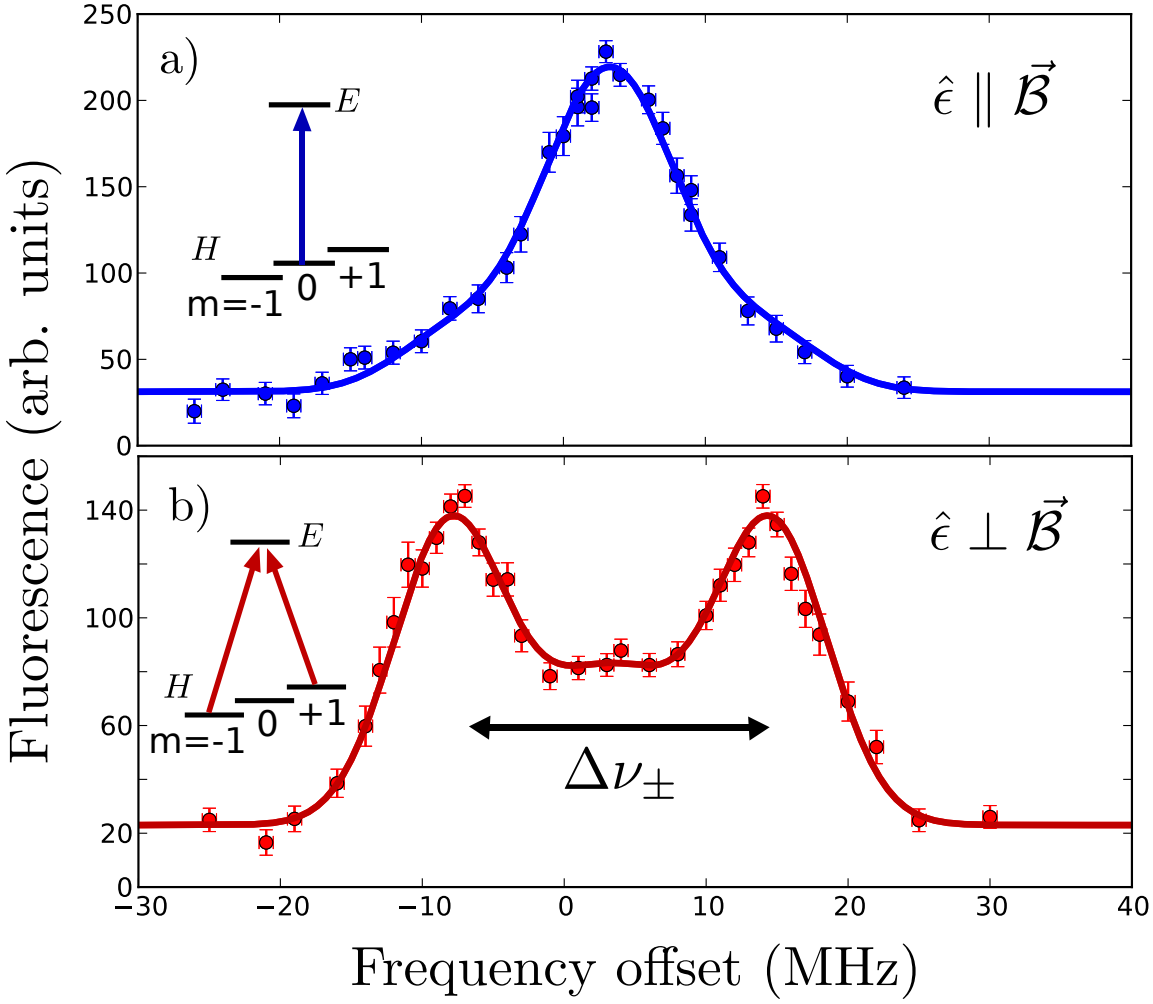

Figure 4.7: Spectra of LIF from the $H, J = 1$ state in a magnetic field $\mathcal{B}_z = 1.9(1)$ kG, acquired with 16 averages per data point. The x-error bars account for the standard error in the laser's frequency offset (derived from the rms frequency excursion of the lock's error signal) and y-error bars indicate the standard error of the LIF signal due to shot-to-shot fluctuations in the yield of molecules in a pulse. a) The probe laser's polarization $\hat{\epsilon} \parallel \vec{\mathcal{B}}$; in this configuration the $m_J = 0$ sublevel is probed. b) With the laser polarization $\hat{\epsilon} \perp \vec{\mathcal{B}}$, the $m_J = \pm 1$ sublevels are probed. The fit to the spectrum in (b) yields $\Delta\nu_{\pm} = 22.66(41)$ MHz for the Zeeman splitting between $m_J = \pm 1$.

relative size of the minority peaks ($\approx 20\%$). We verified that changes in the size of the minority peaks did not affect the Zeeman shift extracted from the fit, to within its uncertainty. Allowing the width of the minority peaks to be a free fit parameter (rather than constraining them to have the same width as the majority peaks) shifted the fit value of $\Delta\nu_{\pm}$ by 0.33 MHz; this effect is included as a systematic contribution to the fit uncertainty. The fit frequency separation between the $m_J = \pm 1$ peaks in Fig.4.7b is $\Delta\nu_{\pm} = 22.66(41)$ MHz. Changing the lineshape function to a lorentzian (instead of a gaussian) yielded $\Delta\nu_{\pm} = 22.20(27)$ MHz (including the systematic uncertainty due to the peak shift after relaxing the constraint on the widths of the peaks, as above). These values agree to within the stated uncertainties. The value obtained with gaussian lineshapes is used to obtain the magnetic moment in the following, as it is expected to be a better physically motivated description of the transverse Doppler distribution of the collimated molecular beam. $\Delta\nu_{\pm}$ is related to the intrinsic magnetic moment of the H state, μ_H, by the formula $h\Delta\nu_{\pm} = \frac{2\mu_H \mathcal{B}}{J(J+1)}$, which can be derived using (A.16).

The magnetic field sampled by molecules in the experiment was characterized as follows. The magnetic field profiles in Fig.4.4b,c were measured with a Hall probe (Lakeshore, HGT-2010) whose active area (0.127 mm $\times$ 0.127 mm) is small compared to the area illuminated by the laser beam. Spatial selectivity along the x-axis was provided by the LIF detection optics, as shown in Fig.4.4b. The acceptance of the optical system was modeled with ray-tracing software (LightTools). The lens and lightpipe were included using built-in models, and the measured distance from the end of the lightpipe to the front face of the PMT (and the distance from the PMT window to the photocathode) were mocked up as an air gap. The light paths were modeled in reverse: with a uniform extended light source at the position of the photocathode, the calculated light intensity distribution at the focal plane was normalized and used as the acceptance function of the light collection system. The angular acceptance of the optical filter was included in the model by restricting the range of angles of light rays emitted by the extended source. This approach allowed the acceptance of the light collection system to be obtained in one shot, instead of having to map it out by scanning a point source at a number of points on the focal plane of the collection lens. The simulated acceptance function is shown in Fig.4.4b. Most of the LIF photons were collected from molecules near the center of the magnet assembly, with small contributions from the wings. The symmetric appearance of the Zeeman shifted peaks in Fig.4.7b confirms that the contribution of the wings of

the acceptance function was small, as a large contributions from the wings would skew the peaks to have larger tails towards the zero field LIF peak position. A further constraint on the range of x-values sampled by the LIF collection optics can be derived from the Doppler width of the zero-field peak in Fig.4.7a, which implies that the maximum FWHM (along the $\hat{x}$-direction) of the LIF acceptance function is $\Delta x = 10$ mm.[9] The average $\mathcal{B}_z$ calculated along the $\hat{x}$ direction over a range $\pm$ 5 mm from the center (1.91 kG) is very close to the value of the $\mathcal{B}$-field at $x = 0$ (1.89 kG), and both are well within the systematic error in $\langle \mathcal{B}_z \rangle$ quoted below.

The separation between the magnets was too small to allow a direct measurement of $\mathcal{B}_z$ along $\hat{z}$, so we accounted for the spatial dependence in the yz plane in the following way. The value of the $\mathcal{B}$-field measured at the origin in the $\mathcal{B}_z$ vs. y profile was used to calibrate the pole strength in a 2D numerical calculation in the yz plane based on the (measured) magnet geometry. When weighted over an area corresponding to the Hall probe, the calculation reproduced the measured $\mathcal{B}$-field profile, as shown in Fig.4.4c. The calculated $\mathcal{B}$-field pattern was weighted by the Gaussian intensity profile of the probe laser beam in the yz plane and averaged to obtain $\langle \mathcal{B}_z \rangle$. Changing the weighting function (representing the laser's transverse mode profile) to a lorentzian shape did not affect the variation observed in $\langle \mathcal{B}_z \rangle$. Changing the width of the laser beam profile, from a Gaussian with a width $\sigma =$ 0.16 mm (the value measured for the laser's transverse mode profile) to one with a width $\sigma' = 0.48$ mm (to account for the remote possibility that the $H \rightarrow E$ transition was very strongly power-broadened) changed $\langle \mathcal{B}_z \rangle$ from 1.86 kG to 1.95 kG. This is well within the systematic uncertainty due to deviations off the center line, derived below.

The effect of deviations of the laser beam path from the center line of the magnet assembly on the value of $\langle \mathcal{B}_z \rangle$ was also calculated using the 2D numerical calculation, for a range of displacements of the laser beam profile ($\pm$ 0.5 mm) from the exact center of the magnets in the yz plane. This was done to account for the experimental uncertainty in the laser's position and pointing.[10] The range of variations observed

[9] This estimate uses the value $v_{\parallel} = 160$ m/s for the forward velocity.

[10] This range of displacements was used based on the estimated uncertainty of the procedure for the alignment of the laser beam along the center-line of the magnet assembly. This procedure involved the following steps: a visible laser (690 nm) was aligned along the center-line of the magnets, by observing the "shadow" of the magnets in the scattered light profile after passing through the magnets. A spatial scale for the variations in pointing observed in the shadow was provided by the spacing between the magnets (3 mm). The 908 nm probe laser was aligned to be collinear with the visible laser beam, and the visible laser beam was blocked during the measurement. Due to the

in $\langle \mathcal{B}_z \rangle$ under this procedure leads to the estimate that $\langle \mathcal{B}_z \rangle = 1.9(1)$ kG in the probed volume. As a further check on systematic errors arising from the probe laser's alignment, an independent measurement with a complete realignment of the laser's path through the magnet yielded a value $\Delta\nu_{\pm} = 21.7(4)$ MHz - this value of the Zeeman shift is within the estimated range of possible changes in $\langle \mathcal{B}_z \rangle$ due to misalignment (5%).

We combine the fit uncertainty in quadrature with uncertainties in the probe laser's frequency calibration (1%) and the central value of the $\mathcal{B}$-field in the probed volume (5%) to obtain $|\mu_H| = 8.5(5) \times 10^{-3}\ \mu_B$ for the magnetic moment of the H state. Note that the measurement arranged this way is only sensitive to $|\mu_H|$; the probe laser would have to be sent parallel to the molecular beam in order to establish the sign of μ_H. It is remarkable that in this molecular state, with $2\mu_B$ worth of magnetic moment each from the orbital and spin angular momenta, these contributions cancel out to better than 1%.

4.3.2 Molecule-fixed electric dipole moment

For these measurements a pair of 0.9 mm thick glass plates, coated with transparent conducting indium tin oxide on one side and broadband anti-reflection coating on the other (CH-50IN-1509, Delta Technologies), were used to make a capacitor with 25 mm x 30 mm plates separated by a 3.00(5) mm vacuum gap. The molecular beam was passed between the plates and a linearly polarized probe laser was sent at right angles to the molecular beam, normal to and through the transparent plates. This electric field plate assembly was again mounted on a KF40 flange for modular insertion into the probe region in MB2. LIF was collected with the same optical arrangement used for the magnetic moment measurement, at right angles to both the molecular beam velocity and the probe laser's k-vector.

In the $H(v = 0)$ state, we focus our analysis on the $J^p = 1^{\pm}, |m_J| = 1$ Ω-doublet states (p denotes the parity of the state). In the absence of an electric field, these states are parity eigenstates and are separated by an energy Δ_0. (The Zeeman sublevels with $m_J = 0$ do not mix in an electric field as a result of angular momentum selection rules, and we ignore them in the rest of this analysis.) In the

aspect ratio of the laser's path through the magnets, offsets in the laser's transverse position, unless compensated by the laser's pointing, would not have allowed it to pass through the center-line of the magnets - as a result, even with transverse position offsets, the laser is estimated to have intersected the volume at the center of the magnet to within ± 0.5 mm.

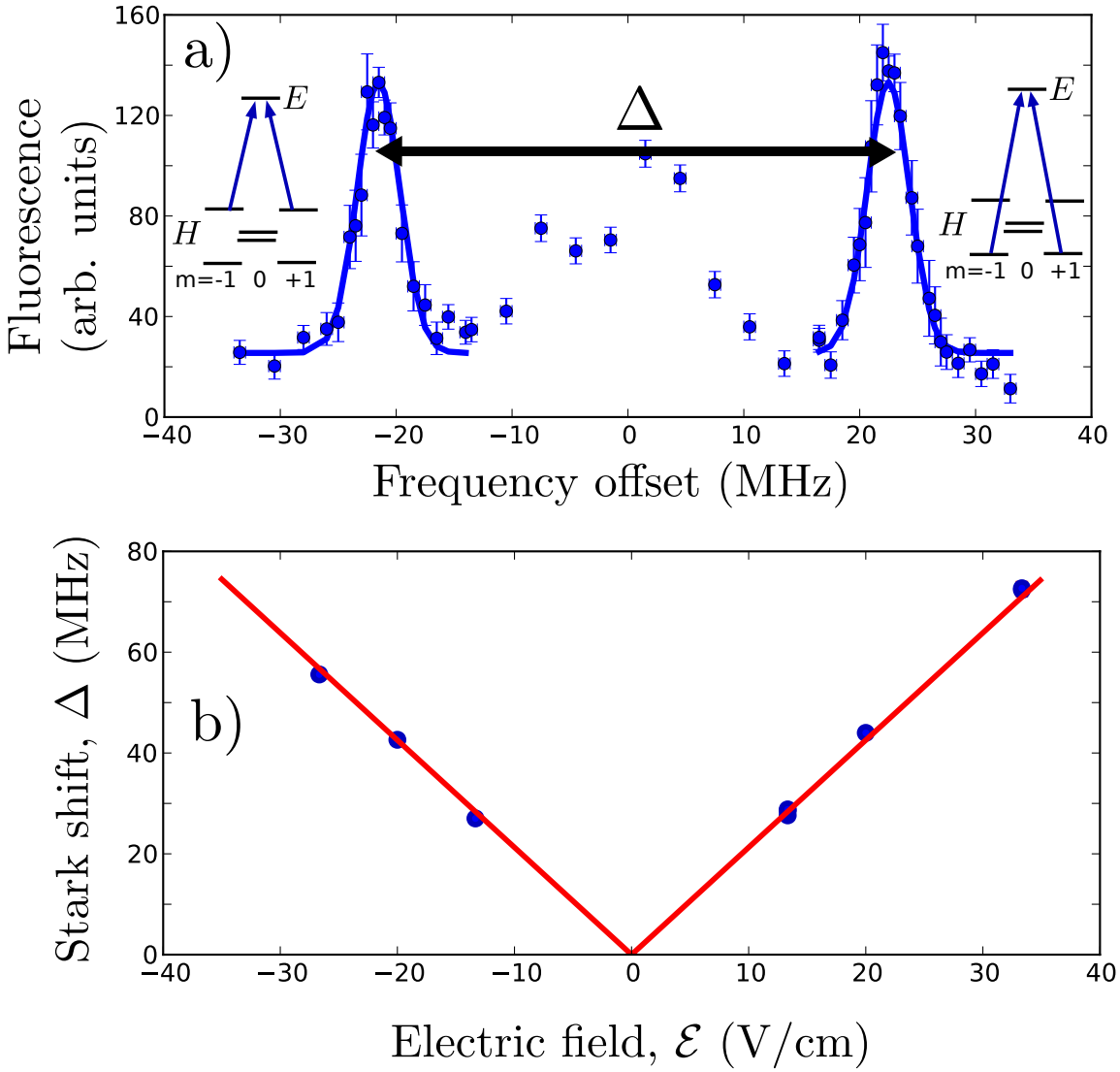

Figure 4.8: a) Example LIF spectrum from the $H, J = 1$ state in an electric field $\mathcal{E}$ =20 V/cm, acquired with 16 averages per data point. The error bars are assigned in the same way as in Figure 4.7. The two $\mathcal{E}$-field polarized states are separated by a frequency Δ. The LIF signal near zero offset is due to molecules outside the electric field plates. In b), Δ is plotted as a function of the $\mathcal{E}$-field across the plates. The solid line is a fit to the function $\Delta = |D_J\mathcal{E}|$. The slope of the plot yields $D_{J=1} = h \times 2.13(2)$ MHz/(V/cm) for the dipole matrix element between the Ω-doublets in $H, v = 0, J = 1$ state.

two-state space spanned by the basis states $J = 1^{\pm}, m_J = +1$ (or identically, the space with $m_J = -1$, since $m_J = \pm 1$ are degenerate in an $\mathcal{E}$-field), the system in an $\mathcal{E}$-field is described by the Hamiltonian $H = \begin{pmatrix} -\Delta_0/2 & -D_J\mathcal{E} \\ -D_J\mathcal{E} & \Delta_0/2 \end{pmatrix}$, where D_J is the electric dipole matrix element connecting the two basis states. The energy spacing between the eigenstates is $\Delta = 2\sqrt{\Delta_0^2/4 + D_J^2\mathcal{E}^2}$. In the limit where $|D_J\mathcal{E}| \gg \Delta_0$, the parity eigenstates are completely mixed and the energy spacing between the polarized eigenstates is $\Delta \approx 2|D_J\mathcal{E}|$.

In the measurement, the probe laser couples the $\mathcal{E}$-field-polarized states in the $H, v = 0, J = 1$ manifold to the $E, v = 0, J^p = 0^+$ state for LIF. The excited E state does not have Ω-doublets, and in an $\mathcal{E}$-field the predominant mixing of the $E, J^p = 0^+$ state is with the neighboring $E, J^p = 1^-$ rotational state. Since the rotational spacing in the E state ($\sim 2\pi\times$ 20 GHz) is much larger than the zero-field Ω-doublet spacing ($\Delta_0 \sim 2\pi\times$ 400 kHz) in the H state [EL84], whereas the dipole matrix elements are of comparable size, there is a range of electric fields (1 V/cm $\lesssim |\mathcal{E}| \lesssim$ 1 kV/cm) where the $H, J^p = 1^{\pm}$ Ω-doublets are fully mixed while the $E, J^p = 0^+$ state remains a parity eigenstate to a good approximation. In this regime therefore, LIF signals from both the polarized eigenstates in H should be visible with equal intensity. Since the laser polarization $\hat{\epsilon} \perp \vec{\mathcal{E}}$, only $|m_J| = 1$ states are excited by the laser.

The sample LIF spectrum in Fig.4.8a shows peaks from the $\mathcal{E}$-field polarized eigenstates that are separated by a frequency Δ. They are also well separated from the residual $\mathcal{E}$-field-free signal, which was due to molecules excited outside the capacitor plates. The narrowness of the $\mathcal{E}$-field polarized spectral peaks was due to additional collimation of the molecular beam by the capacitor plates. Gaussian lineshapes were fit to the $\mathcal{E}$-field polarized spectral peaks and their separation Δ was extracted. Changing the lineshape function to a lorentzian did not affect the peak separation that was extracted from the fit. The $\mathcal{E}$-field-free signal was excluded (by excluding data points more than 2 linewidths from the peak center, towards the zero-field peak) for the purpose of fitting and extracting Δ from the data. Changing the boundary of the excluded data by 0.5 $\times$ linewidth changed the the fit separation between the field-polarized peaks by $\sim 1\%$ (in this respect, a lorentzian lineshape was found to be more robust than a gaussian). This effect is added in quadrature to the statistical uncertainty on the peak separations obtained from the fit. In Fig.4.8b, the frequency separations Δ extracted from a set of LIF spectra are shown plotted

against the $\mathcal{E}$-field across the plates. The linear dependence of Δ as a function of $|\mathcal{E}|$ indicates that the H state was fully polarized over the range of $\mathcal{E}$-fields applied during the measurements. The fit yields the value $D_{J=1} = h \times 2.13(2)$ MHz/(V/cm). The intercept of the linear fit constrains $\Delta_0 \leq 2$ MHz, in agreement with the result of [EL84]. The relation between D_J and the molecule-fixed dipole moment in the H state, D_H, is $D_J = \frac{D_H}{J(J+1)}$, using (A.16). We found $|D_H| = 1.67(4)\ ea_0$, where the reported error is a quadrature sum of the fit uncertainty (1%), and systematic uncertainties due to laser frequency calibration (1%) and field plate spacing (2%).

Chapter 5

Apparatus

> It is very easy to be blinded to the essential uselessness of them by the sense of achievement you get from getting them to work at all.
>
> The Guide, *So Long, and Thanks for All the Fish*

This Chapter contains a description of some of the pieces of the molecular beam EDM apparatus that I designed or constructed. The global coordinate system for the experiment defined in Chapter 2 is used in the descriptions. Recall that $\hat{x}$ is the molecular beam axis (horizontal in the lab), $\hat{y}$ is the vertical axis in the lab and $\hat{z}$ is the direction of the main $\mathcal{E}$ and $\mathcal{B}$-fields (horizontal in the lab).

5.1 Mini-beam sources

The measurements described here were performed using test molecular beam sources, built around a liquid helium cryostat (Infrared Labs, HDL-5).[1] I constructed one closed-cell apparatus (CC1) and two beam sources (MB1 and MB2) at various points between 2007 and 2010. These sources are fairly similar in construction and share a number of common features. CC1 was used for the initial production, optical pumping and H state lifetime measurements. MB1 (which has a vertical downwards-pointing beam) was used in the initial measurements of beam extraction out of the cell, a number of spectroscopy measurements (to probe transitions to the A, C, G, E states from the X, H states and measure their saturation intensities),

[1] These are dubbed "mini-beam" sources to distinguish them from the pulse-tube cooled molecular beam source that is used for the full-blown eEDM experiment.

and a measurement of the lifetime of the C state. MB2 was used to measure the electric and magnetic moments of the H state, precise saturation intensities of the $X \to C, X \to A, H \to C$ and $H \to E$ transitions, and for preliminary measurements of the optical detection of spin precession.

The structure of the latest beam source (MB2) is described briefly here. ThO molecules are produced by pulsed laser ablation of solid ThO_2 using $\sim$ 6 ns long, 10 mJ pulses at 532 nm from an Nd:YAG laser. The ablation targets used in these studies were broken off from a sintered pellet of ThO_2 powder with a density of 6.9 g/cm^3.[2] The target is held inside a copper cell which is thermally anchored to a liquid helium cryostat. Helium gas continuously flows at a rate of 4×10^{18} atoms/s through the cell and exits it through a 1/8 in. diameter aperture in a 0.25 mm thick copper plate, resulting in a stagnation density $n_{He} \sim 10^{16}$/cm^3 in the cell. A charcoal-covered copper shield, with a 0.25 in. aperture that is 2 in. away from the cell aperture along the molecular beam axis, surrounds the cell to pump away the helium buffer gas atoms and maintain a good vacuum. After passing through a 0.50 in. aperture in the 77 K radiation shield of the cryostat, molecules exit the cryostat vacuum chamber and enter a room temperature vacuum chamber ("probe" chamber). Molecules in the beam are probed either inside the cryostat vacuum chamber, or in the probe chamber. The probe chamber is constructed out of a 6-way KF40 cross, which allows optical access for lasers and light collection at right angles to each other and to the molecular beam. A beam collimator, made out of 1/16 in. thick sheet metal brazed into a KF40 centering ring, is used to provide a narrow and well-defined velocity distribution for some measurements. A 60 l/s turbo pump, at the opposite end of the cross from the cryostat chamber, provides additional pumping for the probe chamber. Viewports on the laser access ports are constructed from 1 in. anti-reflection coated glass windows (Thorlabs) that are sealed onto a machined seat in an aluminum KF40 stub using an indium wire gasket. This procedure provides simple, leak-free seals on the viewports. Either a commercial (non-AR-coated) KF40 viewport, or a lightpipe fed through a 1 in. diameter quick-disconnect $\to$ KF40 adapter, are used on the light collection ports to collect fluorescence. In this apparatus, we typically observe a pulse of $N_{beam} \approx 10^{10}$ molecules in a single quantum state exiting the cell, with a pulse width of $\sim$ 5 ms. The beam source has been operated at repetition rates up to 15 Hz.

[2]This target was fabricated at Oak Ridge National Laboratory, and provided to us by Dr. Daniel Stracener.

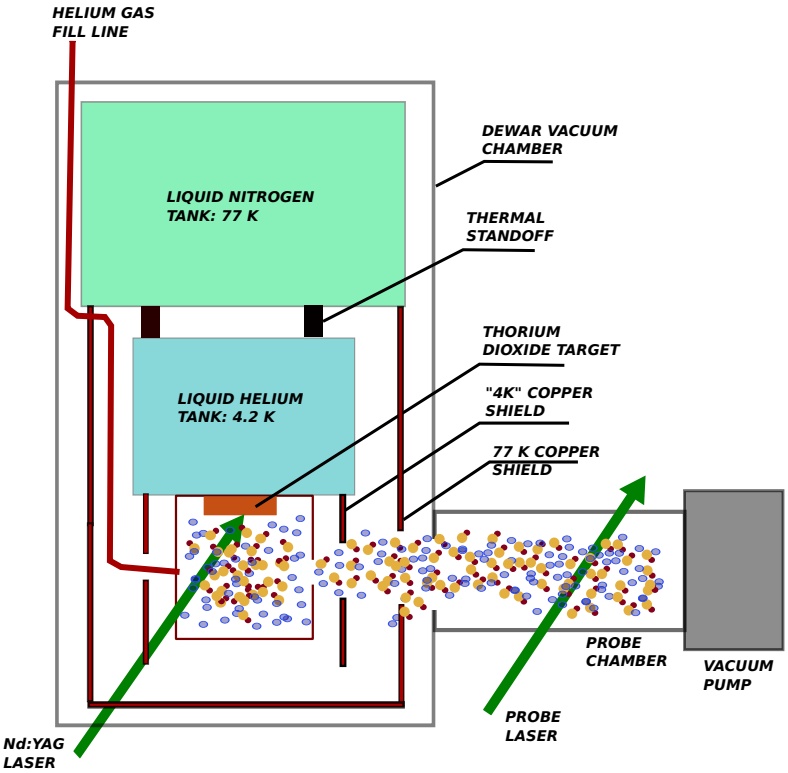

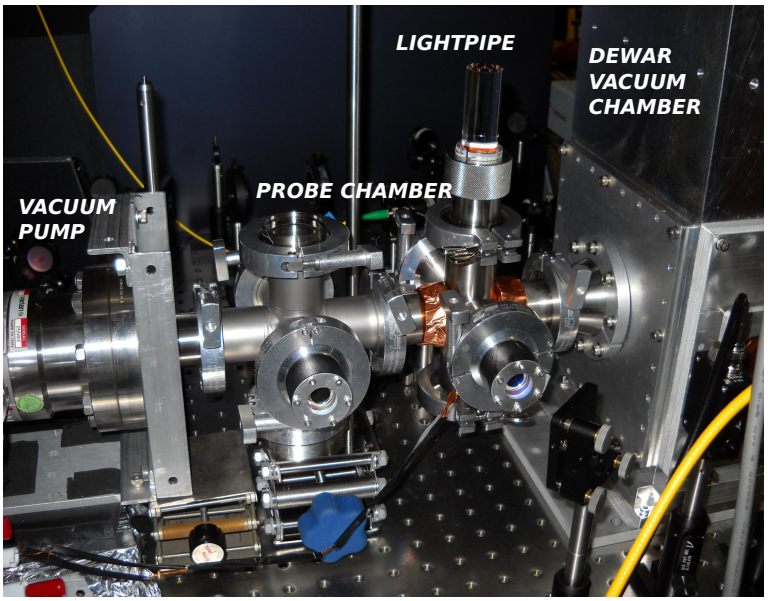

Figure 5.1: Schematic of the mini-beam source MB2. The photograph shows a view of the dewar vacuum chamber and the probe region, assembled on an optics table.

5.2 Electric field plate assembly

The purpose of the electric field assembly is to provide a spatially uniform $\mathcal{E}$-field over the volume sampled by the molecular beam during the free precession of the spin in the H state. The $\mathcal{E}$-field is provided by a pair of parallel plates. This arrangement was chosen in the interest of simplicity, both for construction and for calculation of the field. Based on unpublished information from the YbF experiment, where some systematics were found to be related to the bowing of the plates and from strains in their support structure, the decision was made to mount the plates vertically to avoid deforming them. As described in Chapter 2 the method of optical detection of spin precession, using the polarization of the state-preparation and detection lasers, requires the lasers to propagate parallel to the $\mathcal{E}$-field in order to excite the molecules with both $\hat{\epsilon}_x$ and $\hat{\epsilon}_y$ polarizations. It is also convenient to be able to collect laser-induced fluorescence from the molecules at the end of their precession path. Due to these reasons, convenient optical access through the field plates was a further requirement of the design. Since the field plates are located inside the interaction region vacuum chamber, and within the magnetic shields, further constraints included the following:

- Construction entirely out of non-ferrous and non-magnetic alloys, to avoid generating $\mathcal{B}$-field offsets.
- All materials used in construction to be UHV-compatible, to reduce outgassing.
- No dissimilar metals in contact, in order to avoid thermo-electric currents generated by contact potentials.

These requirements and constraints were addressed in the design as follows. The electrodes were constructed out of 1/2 in. thick plates of borofloat glass, coated with a conducting transparent layer of indium tin oxide (ITO). Borofloat glass stock is readily available with extremely flat and parallel surfaces. Using standard glass polishing techniques, its surface can be finished to specifications that are much flatter and smoother (in terms of surface roughness) than can be achieved for metals. In addition, glass is an extremely good electrical insulator and is mechanically very rigid. The field plates were fabricated by Custom Scientific Inc. The plates are 17 in. wide x 9 in. high. The plates were designed to have a z-spacing of up to 1.5 in. and therefore the dimensions of the plates were chosen to be large in order

to minimize fringing effects from the edges. Both surfaces were polished to b$\sim 3\lambda$ flatness (at $\lambda = 633$ nm) and with a parallelism ~ 10 arc seconds across the entire surface. One face of each plate has a deposited ITO layer with an electrical sheet resistance of 100 Ω/square. The opposite face is coated with a broadband anti-reflection coating between 600 and 1100 nm, which has an average reflectance $< 1\%$ at normal incidence in this wavelength band.

The mechanical structure supporting the field plates was an integral part of the design. It was required to have enough degrees of freedom so that the plates could be precisely aligned to be mutually parallel (or deliberately misaligned to test for systematic effects), but also required to be mechanically stable and robust against slow variations and vibrations once the plates were positioned in place inside the vacuum chamber. For this reason, a kinematic design was used, where the number of constraints of the mechanical assembly equals the number of degrees of freedom of the components in the structure [Fur81, Str38]. The mechanical structure of the field plate assembly is as follows. Each ITO-coated glass field plate is sandwiched between a copper front frame and an aluminum back frame. The copper front frame holds the glass plate along its periphery, and is constructed out of C101 copper coated with a 5 μm thick layer of gold.[3] The front frame doubles as a guard ring electrode in order to extend out the fringing field of the plates and to make the $\mathcal{E}$-field more uniform. The front frame is electrically isolated from the ITO-coated conducting surface with a polyimide (Kapton) spacer. The front frame also serves to shield the corners of the ITO-coated glass plate (where non-ITO-coated rail marks exist along two edges, and other parts where electrical leads are attached to the plates) from being 'seen' by the molecules in the beam. The back frames are machined out of of 6061 aluminum and form the structural support for each plate sandwich. They contains a number of thru holes, through which non-conducting plastic (PEEK[4]) screws are used to thread into tapped holes on the back of the front frame and compress each sandwich. They also have a number of tapped holes, for spring attachments and for attachment to the horizontal base plate of the $\mathcal{E}$-field assembly. The seat for the glass plates on the aluminum back frames is cushioned with a polyimide gasket, to suppress the generation of cracks at glass-metal contact points. One of the plate sandwiches is shown in section in Figure 5.2.

[3]This is a thicker layer than usual, to counter the effect of gold diffusing into the copper since no intermediate layer was used. An intermediate layer was avoided since most alloys used for that purpose are nickel-based. The gold coating was done by Aotco Inc.

[4]Poly ethyl ether ketone, a low-outgassing plastic with favorable mechanical properties.

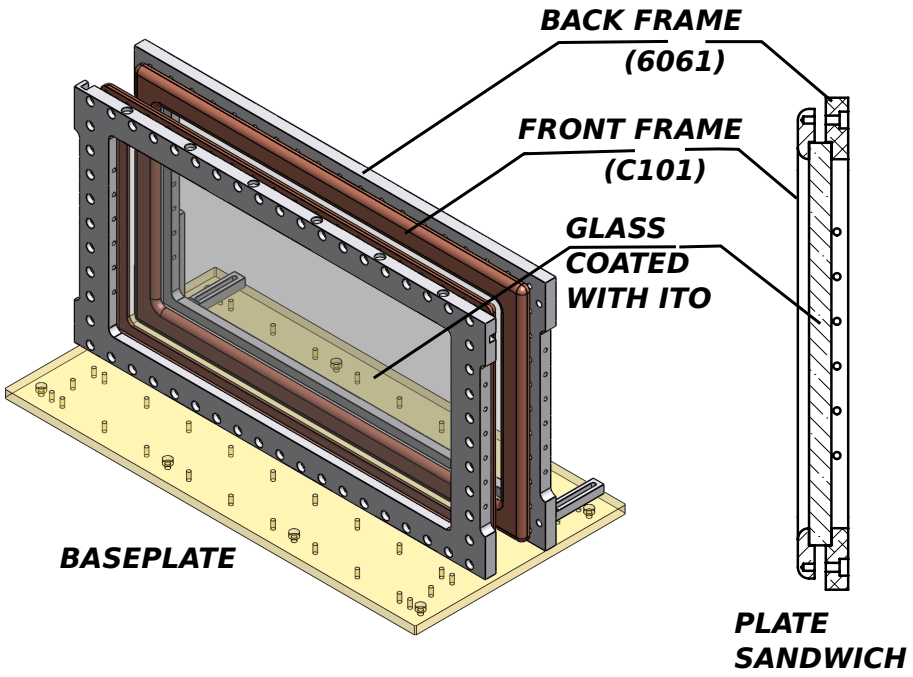

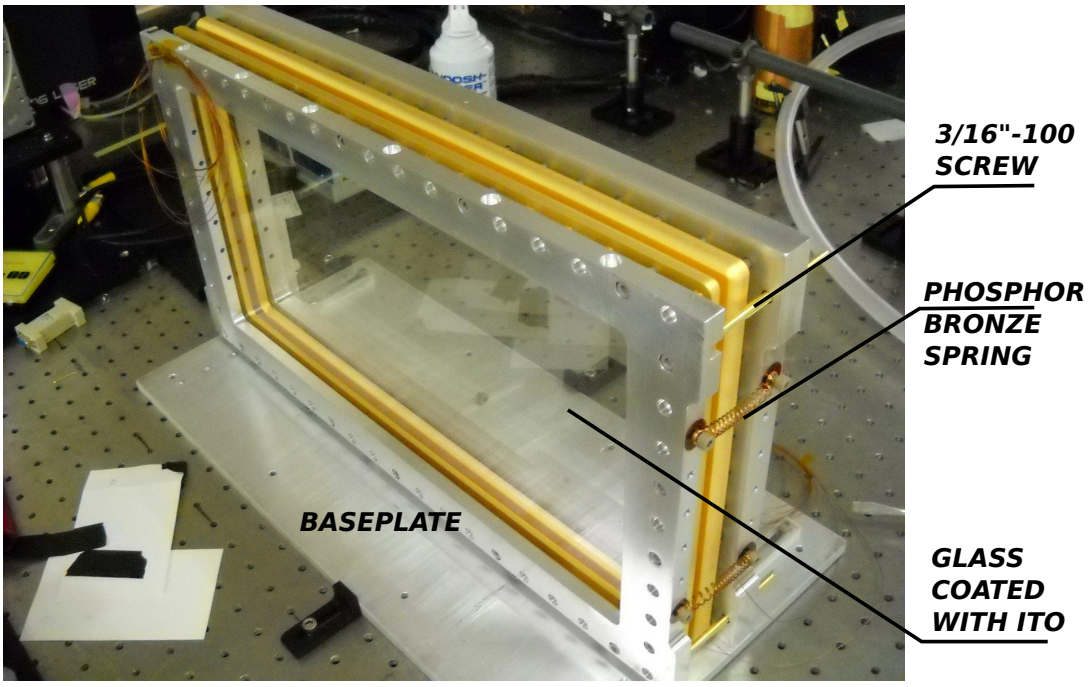

Figure 5.2: The electric field plate assembly, consisting of a pair of plate sandwiches (Cu frame:ITO-coated glass:Al frame) clamped together with springs. The contact points between the plate sandwiches and the base plate are kinematically constrained. The structure is assembled on the baseplate and then loaded inside the vacuum chamber.

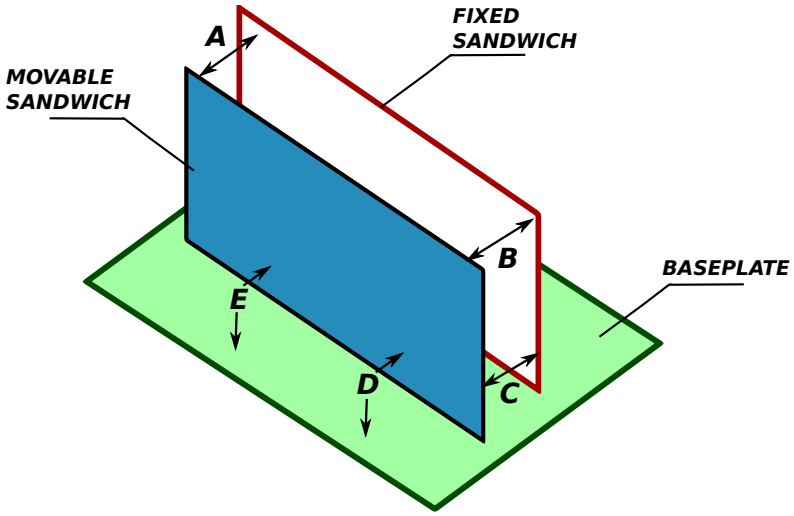

Figure 5.3: The diagram shows the linkages between the pieces of the kinematic mount. The fixed and movable plate sandwiches consist of copper-glass-aluminum sub-assemblies as shown in Figure 5.2. The fixed sandwich is rigidly bolted to the baseplate. The linkages labeled in the diagram are: (A) ball on flat, (B) ball on flat, (C) ball in V-groove, (D) ball on flat, (E) ball on flat. The fixed and movable sandwiches are held together under tension by phosphor bronze springs. Fine pitch (3/16"-100) screws at A,B and C provide control over the spacing and parallelism of the glass plates contained in the sandwiches.

One of the sandwiches forms the "fixed" piece of the kinematic assembly. It is rigidly attached to the aluminum baseplate with PEEK screws. The other sandwich forms the "movable" piece of the kinematic assembly. The kinematic contacts are modified from the usual Kelvin clamp contact, familiar from a regular optics mirror mount, in order to avoid lifting the considerable weight of the movable plate using only spring tension. By relaxing two of the constraints of a Kelvin clamp, and adding two points of contact to the baseplate to restore the kinematic condition, the movable piece can be supported by normal reaction off the baseplate. The contacts consist of one ball-in-groove contact + 2 ball-on-plate contacts between the fixed and movable pieces, and two ball-on-plate contacts between the movable piece and the baseplate. The diagram in Figure 5.3 shows how the sub-assemblies are linked into the kinematic assembly. All the kinematic contacts are directly between the aluminum back plates of the fixed and movable sandwich and the aluminum breadboard, i.e. between surfaces that are all nominally at ground potential. As there are no spacers directly between the electrodes, this should suppress leakage current paths and their resultant $\mathcal{E}$-correlated $\mathcal{B}$-fields. Sapphire balls (General Ruby) and thin sapphire

disks (Edmund Optics) are used for the contacts. They are epoxied[5] into recessed seats on the metal plates. The sapphire balls making contact between the fixed and movable sandwiches are located on the end of fine-pitch screws (3/16"-100, turned out of C260 low-ferrous brass tube) that thread into PEEK inserts epoxied into the fixed plate sandwich. These allow the angle between the ITO-coated glass plates to be varied in < 0.2 mrad increments. The two plate sandwiches are clamped together using 4 phosphor bronze springs (Century Spring Inc.), which together provide approximately 20 lbs. of clamping force, to keep the structure kinematic and suppress vibration modes. The baseplate has a number of tapped holes for the attachment of mounts for the fluorescence collection optics. The entire structure, consisting of the $\mathcal{E}$-field plate assembly and the light collection optics, can be assembled and tested on the bench and loaded as a module into the vacuum chamber. The field plate assembly, consisting of plates and kinematic mount, is shown in Figure 5.2(b). The location of the field plate assembly within the vacuum chamber and along the molecular beam line is constrained by close clearance screws that bolt it onto the frame of the vacuum chamber.

The field plate assembly is designed to be modular, and all components can be replaced or modified easily when required. When assembled, the only surfaces that are visible to the molecular beam over the spin precession region are the ITO-coated faces of the glass plates and the gold-coated copper guard rings.[6] The parallelism of the plates is measured using a white light interferometric sensor to map out the separation between the plates at various points across its surface [Pat71]. It is capable of remotely measuring the separation between the plates to an accuracy of about 2 μm and mapping this separation across the surface of the plates in the the xy-plane. This system for measuring the plate separation was built by Ivan Kozyryev.

5.3 Vacuum system

The vacuum chamber encloses the electric field plate assembly and the light collection optics. It is located within the magnetic field coil and the magnetic shields. It is connected to the cryogenic molecular beam source on the upstream end. The molecular beamline continues through the chamber and ends in a vacuum pump. Based

[5]The epoxy used was Stycast 2850FT + catalyst 24LV (Emerson-Cummings) in a 100:7 ratio. It has outgassing specifications that are slightly better than Epo-tek 353ND, an epoxy that is routinely used for UHV assemblies [CS93].

[6]The patch potential properties of ITO and gold are reported in [RBB$^+$06].

on a conservative estimate of the mean free path of ThO molecules in collisions with background gas molecules, the vacuum chamber was designed to work at a vacuum level of $\lesssim 10^{-7}$ Torr. It was designed to use only non-ferrous alloys everywhere. It was constructed out of plates of 6061 aluminum welded on the inside seams, by Atlas UHV Inc. The chamber is a rectangular box, approximately 25 in. (x) x 16 in. (y) x 16 in. (z), with large flanges covering the openings on each side. These flanges have smaller ports and sub-flanges to allow the vacuum chamber to be modular. At the time of writing, the chamber has 3 optical viewports on the xy-plane flanges, 11 cm apart. The top (xz-plane) flange has some utility ports that could potentially be used as electrical or gas feedthroughs. The yz-plane flanges on the upstream and downstream ends of the chamber have a large central port for the pumpout trunks described below, and a number of smaller KF16 and KF10-sized ports. The KF16 ports are used as feedthroughs for lightpipes from the fluorescence collection system and the KF10 ports are used for electrical feedthroughs. One of the benefits of aluminum construction is that these vacuum port configurations on the chamber's flanges can be quickly and easily reconfigured if required, since aluminum is easily machinable. All vacuum seals on the chamber are made using viton o-rings that are baked in a vacuum oven at 150 ^{o}C for 6 hours. In operation, the pressure in the chamber is $\sim 5 \times 10^{-8}$ Torr, with the gas load dominated by water vapor, likely due to adsorbed molecules on the aluminum surfaces.

The chamber is connected to the cryogenic source chamber upstream through a 4 in. diameter x 12 in. long aluminum tube ("trunk"), and to the vacuum pump on the downstream end through an identical trunk. The purpose of these trunks is to penetrate the magnetic shields axially, and allow vacuum connections to the beam source and the pump to be made outside the shields using standard off-the-shelf vacuum hardware that is free to contain ferrous alloys. The vacuum pump is a single 500 l/s turbo pump (V550, Varian) backed by a dry scroll pump (TS300, Varian). This choice was made in order to avoid having any contamination on the chamber or its contents from vacuum pump oil.

The vacuum chamber is supported by bolting its frame to extruded 71 in. long aluminum rails (80/20 Inc.), which extend out from the magnetic shields and form a frame. This frame can be moved on casters and leveled, and locked in place by bolting it to threaded inserts that were installed in the concrete floor of the lab. Figure 5.4 shows this support structure, assembled with the aluminum rails extending through the endcap assembly of the magnetic shields.

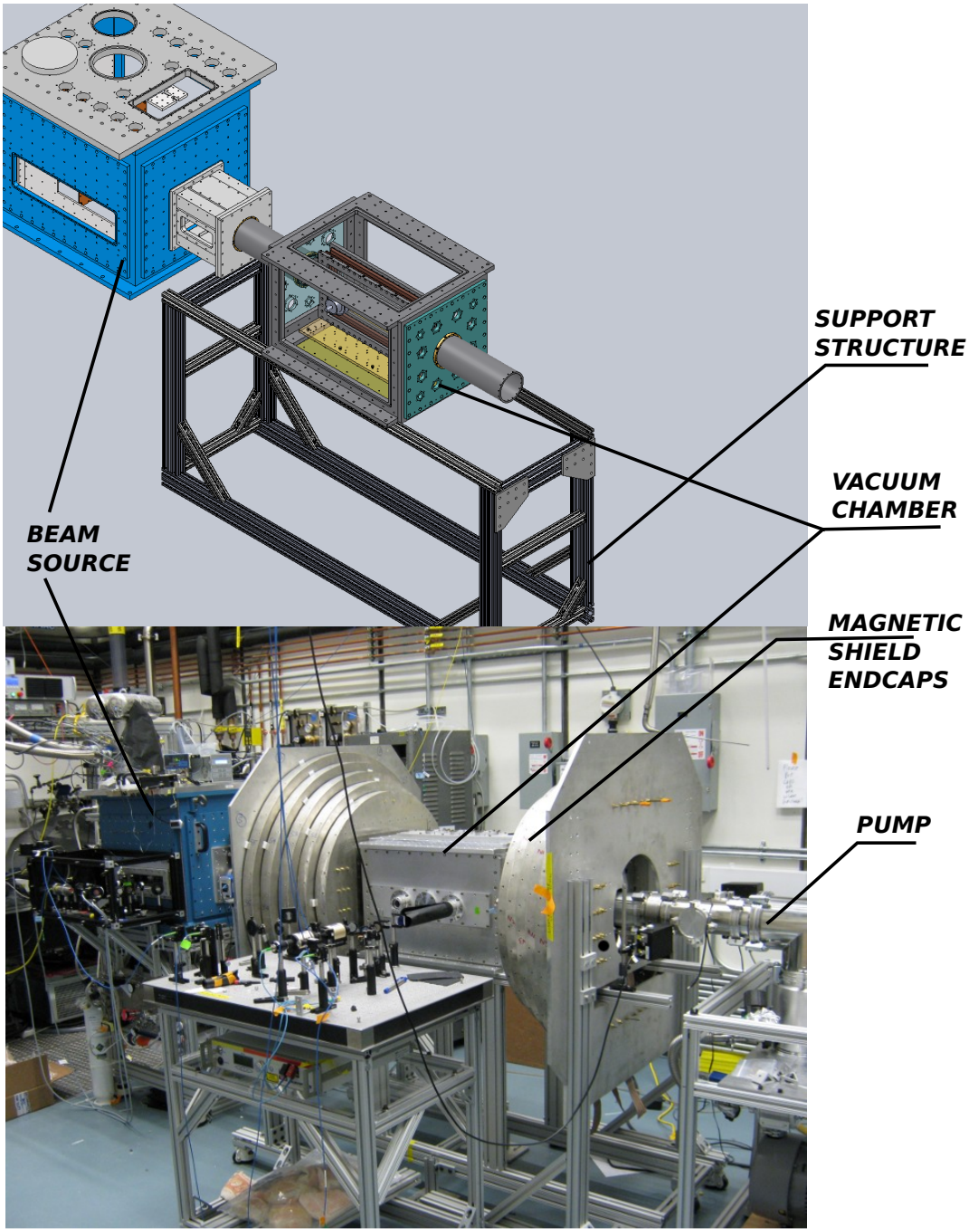

Figure 5.4: The drawing and photo show the vacuum chamber for the interaction region of the measurement, assembled along the molecular beam line. The photo also shows the stack of endcaps for the magnetic shields, assembled around the vacuum chamber. The $\mathcal{B}$-field coil around the vacuum chamber and the half-cylinders for the magnetic shields are not shown.

5.4 Magnetic shielding

The requirements on the $\mathcal{B}$-field derived in Chapter 2 imply that DC and low-frequency magnetic fields must be reduced over the volume of the interaction region by a factor of at least 10^3. (Typical $\mathcal{B}$-fields in the lab from the earth's field and building material are ~ 1 G.) AC magnetic fields can be shielded efficiently by the skin effect, but low frequency (near DC) magnetic fields are more complicated to shield. They can be cancelled either a) actively, using large Helmholtz coils and a magnetic sensor in the region of interest [DDBT07], or b) passively, using high-permeability magnetic shielding [SPS87]. Passive magnetic shielding was chosen based on its relative simplicity and based on our familiarity with its performance in the PbO experiment. The shielding factor S, the ratio of the $\mathcal{H}$-field outside the shield to the $\mathcal{H}$-field inside it, for a single-layer magnetic shield is $S \sim \mu t/D$, where μ is the magnetic permeability (relative to free space) of the material, t is its thickness and D is a characteristic length dimension of the shield [SPS87]. Permeabilities for the typical high-permeability soft magnetic materials used for shielding (usually alloys containing $\sim$75% nickel) are in the range of 1000-5000. These materials are expensive, and so magnetic shields are usually formed out of (up to 1/16 in. thick) sheets of these alloys. Therefore, obtaining a large shielding factor over the volume of the vacuum chamber requires the use of nested magnetic shields, in order to take advantage of the multiplicative effect of nested shields, rather than a single thick shield. However the nested shields cannot be treated as independent entities. They interact in a complicated way with each other and with the air gaps separating them.

The low-frequency shielding factor of a set of nested shields can be calculated using standard formulae [SPS87]. However, a more physical appreciation of the function of magnetic shields (along with some intuition for concepts such as "good magnetic contact") can be obtained by using the method of magnetic circuits [PS00]. This relies on the formal analogy between the equations of steady-state electrical conduction

$$\begin{aligned} \vec{J} &= \sigma\vec{\mathcal{E}} \\ \vec{\nabla}\cdot\vec{J} &= 0 \\ \vec{\nabla}\times\vec{\mathcal{E}} &= 0, \end{aligned} \tag{5.1}$$

relating the current density $\vec{J}$ and the electric field $\vec{\mathcal{E}}$ in a material with a conductivity

σ, and the magnetostatic Maxwell equations

$$\begin{aligned} \vec{\mathcal{B}} &= \mu\vec{\mathcal{H}} \\ \vec{\nabla}\cdot\vec{\mathcal{B}} &= 0 \\ \vec{\nabla}\times\vec{\mathcal{H}} &= 0, \end{aligned} \tag{5.2}$$

relating the $\mathcal{B}$-field and the $\mathcal{H}$-field in a material with a permeability (magnetic "conductivity") μ (in units where $\mu_0 = 1$). This allows the use of intuitively familiar electrical concepts to the design of magnetic circuits, while being rigorously correct since the boundary conditions and constitutive relations for the fields are exactly analogous.[7] This approach allows the analysis of magnetic shields, shield subcomponents and the air gaps between the shields as lumped magnetic circuit elements [8]. The concept of magnetic "resistance" is useful in analyzing the quality of a magnetic contact.[9] It is defined as

$$\mathcal{R} = \Phi_B/\mathcal{H}, \tag{5.3}$$

and is the ratio between the magnetic flux Φ_B through a magnetic circuit element and the $\mathcal{H}$-field that generates it. The problem of calculating the shielding factor of a set of nested shields can then be reduced to one of solving a simple electrical circuit for the ratio of analogous electrical currents. Figure 5.5 shows an example of this approach applied to a set of 3 nested shields. Some important properties of magnetic shielding are clarified by the magnetic circuit approach:

- The $\mathcal{H}$-field lines are (almost) perpendicular to the surface of a good magnetic conductor, just as the $\mathcal{E}$-field lines are (almost) perpendicular to the surface of a good electric conductor.

- The air gaps between the shields have an important function. They behave as a (large) finite magnetic resistance in parallel with the small magnetic resistance of the shields. The larger the resistance of the air gap compared to the shield, the smaller is the splitting ratio for the magnetic flux to enter the air gap compared to being returned through the shield.

[7] However, appropriate care is needed: the permeability $\mu(\mathcal{H})$ is a function of the $\mathcal{H}$-field, and the analogous magnetic conductivity is given by the slope of the $\mathcal{B}-\mathcal{H}$ hysteresis curve at the operating point.

[8] Electric and magnetic circuit components can be treated as lumped elements when their length scale is much smaller than the wavelengths of the electromagnetic fields involved.

[9] More properly, this quantity is called the magnetic reluctance.

- The consequences of saturating a magnetic shield (driving the material into the saturated portion of its $\mathcal{B} - \mathcal{H}$ curve) can be easily understood. In this situation, the magnetic conductivity of the material drops to zero, and the shield no longer behaves as a low resistance magnetic short for the flux.

A 5-layer set of nested magnetic shields was designed with the following characteristics, with modularity and ease of assembly being the main criteria, in addition to obtaining a large shielding factor. Mu-metal is a magnetically delicate material, especially after it has been hydrogen annealed, and needs to be protected from any strain developing in the grain structure of the material. Therefore, shields that can be conveniently assembled are likely to survive repeated assembly and dis-assembly in the lab. Typical magnetic shields are constructed as single pieces, which limits the extent to which they can be reconfigured for changes in the enclosed experiment. The shields described here were designed in order to allow them to be reconfigured easily, without requiring a full re-annealing treatment after modifications.

The shields completely enclose the interaction region vacuum chamber and magnetic field coil. They were constructed out of 1/16 in. thick mu-metal by Amuneal Inc.. The outermost shield is 52 in. long and has a 42 in. diameter. The innermost shield is 34 in. long and has a 30 in. diameter. There are 1.5 in. radial gaps and approximately 2 in. axial gaps between consecutive shield layers. Each shield consists of 4 pieces: 2 end caps and 2 half-cylinders, which assemble together to form a closed cylinder. Each end cap has a removable circular panel at the center which can be readily machined on a water-jet cutter.[10] This allows the shields to be customized for various arrangements of vacuum plumbing and optical lightpipes. Currently, the circular panels on the end caps have 5 in. diameter holes for vacuum pumpout tubes, with an array of 3/4 in. diameter holes for electrical and optical access to the interaction chamber. The design includes protective HDPE (high density polyethylene) plastic covers for exposed sheet metal edges to protect them from being accidentally deformed during repeated assembly/disassembly. The shields are supported through their end caps. The stack of 5 end caps is clamped together with 2.125 in. HDPE spacers. This stack is mounted onto an aluminum frame which remains fixed in position around the interaction chamber. The half-cylinders are brought into position

[10]Water-jet machining makes use of a directed stream of water containing garnet grit, to cut through metal by abrasion. The zone of the material that is affected by this machining process is restricted to an extremely small volume around the area of the cut (typically $\lesssim 0.01$ in. in extent). This method of machining is also ideally suited to cutting sheet metal without heating (as the workpiece is submerged under water) or mechanically stressing the bulk of the workpiece.

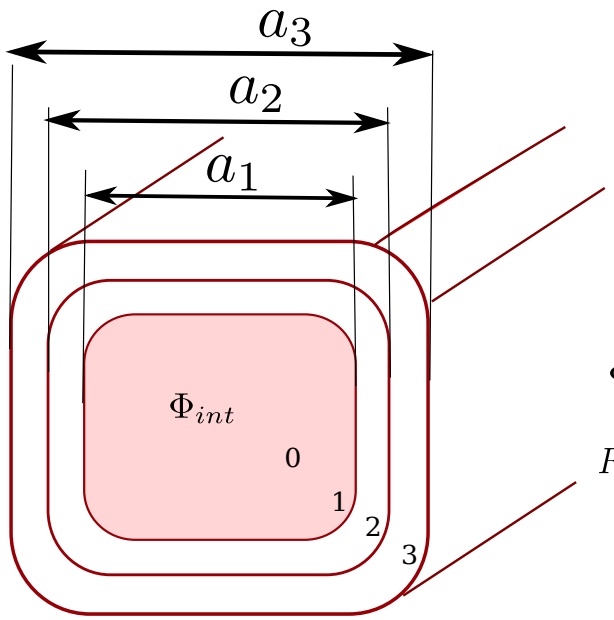

$$S_i \approx \frac{\mu t}{a_i}$$

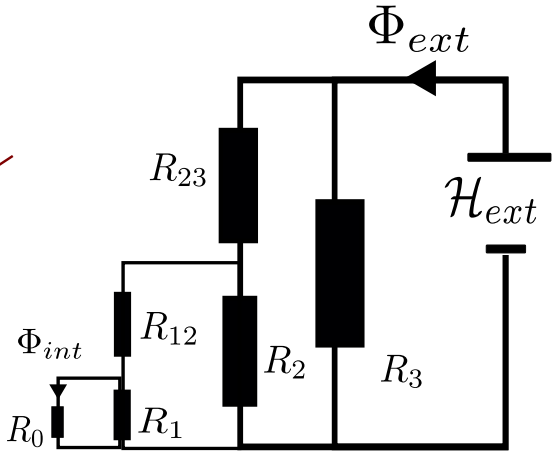

$$\Phi_{32} = \Phi_{ext}\left[\frac{\mu t}{a_3}\left(1 - \frac{A_2}{A_3}\right)\right]^{-1}$$

$$\Phi_{21} = \Phi_{32}\left[\frac{\mu t}{a_2}\left(1 - \frac{A_1}{A_2}\right)\right]^{-1}$$

$$\Phi_{int} = \Phi_{21}\left[\frac{\mu t}{a_1}\right]^{-1}$$

$$S_T = \frac{\mathcal{H}_{ext}}{\Phi_{int} R_0} = S_1 \times S_2\left(1 - \frac{A_1}{A_2}\right) \times S_3\left(1 - \frac{A_2}{A_3}\right)$$

Figure 5.5: An example of the use of the magnetic circuit method to calculate the shielding factor of a set of 3 nested shields, based on [PS00]. The shields are assumed to be made out a thickness t of material with permeability μ, and have cross sectional areas $A_i = a_i^2$ $(i = 1, 2, 3)$. The fluxes Φ_{ij} in the regions between the shields i and j are modeled as currents in the corresponding branches of the equivalent electrical circuit shown. The axial shielding factor S_T is the ratio of the $\mathcal{H}$-fields on the outside of the shields to that inside them. This expression is identical to that derived using the formalism in [SPS87].

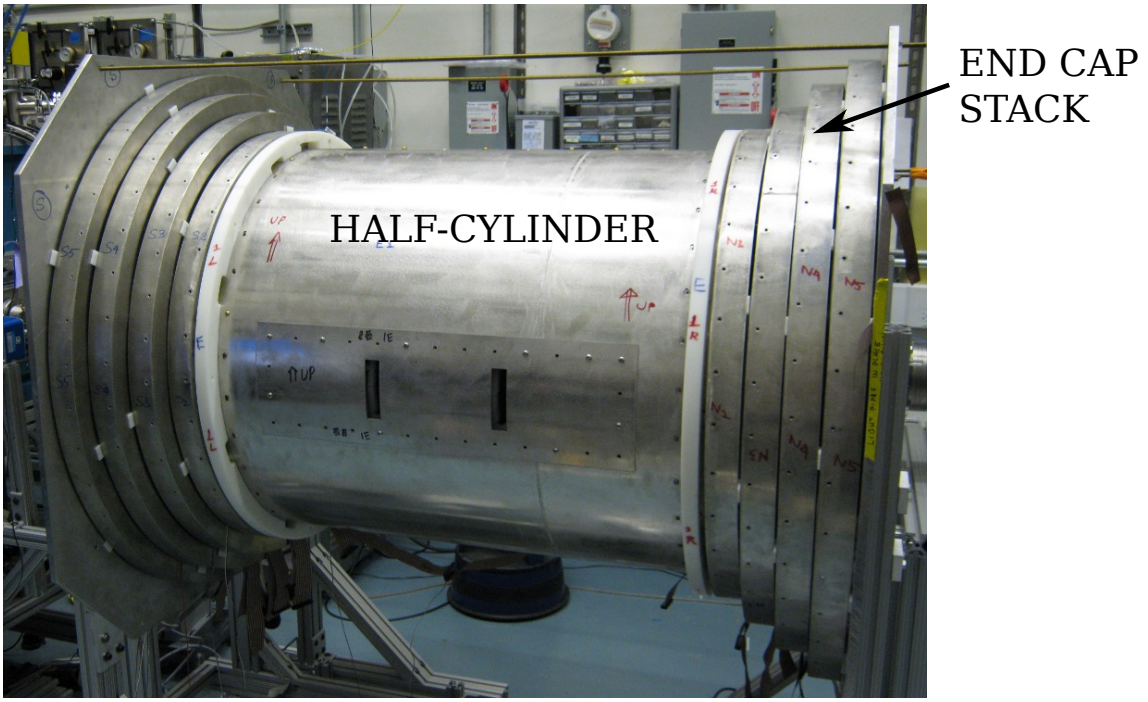

Figure 5.6: A photograph of the magnetic shields, assembled around the vacuum chamber and the interaction region.

transverse to the molecular beam axis and then screwed into place. All removable mates between sheet metal surfaces have approximately 2 in. width of overlap. The half-cylinders have horizontal slots which are covered by removable panels, where the panels again allow the shields to be easily configured with holes for optical access for the state-preparation and detection lasers, without requiring a full redesign of the shields. Good magnetic contact between the different pieces of a magnetic shield requires that mating surfaces have a sufficiently large area of overlap, and that they are clamped together with sufficient force. During manufacture, threaded sheet metal inserts (Penn Engineering, PEM F-032, F-832) were installed to be flush with the surface of mating sheet metal faces, and tack-welded in place to keep them from being stripped out during fastening. Mating pieces are attached together using brass bolts screwed into the threaded inserts. Coils consisting of ribbon cable are wound in between the shields for demagnetizing them, and driven with a 60 Hz waveform that first drives the shields to saturation and then slowly ramps the $\mathcal{H}$-field down to zero [KL97, KBC$^+$65]. The shielding factor of the set of 5 shields for transverse $\mathcal{B}$-fields was measured to be $\sim 10^5$ by Emil Kirilov.

5.5 Dead ends, and other lessons

On the principle that mistakes are more useful to hear about than successes, this section contains a random collection of ideas, some good, some which were partially pursued, and some which were pursued and found not to be fruitful. They are listed here in the hope that they may either prevent some mistakes from being made, or give rise to some new ideas.

Fresnel lenses and bent lightpipes

The initial concept for the light collection system involved large area ($\sim$ 5 in. diameter) Fresnel lenses positioned adjacent (and parallel to) the field plates, with holes machined through their centers to pass the state preparation and detection lasers through. Fresnel lenses with a small f-number (up to f/0.2) are commercially available (FresnelTech Inc. and NTKJ Corp., Japan) and are inexpensive. They have the advantage that they are usually molded out of acrylic, which can be readily machined and modified unlike glass. However, Fresnel lenses work optimally only over a small range of wavelengths around the design wavelength (i.e. they suffer from strong chromatic aberrations), and they have large Fresnel losses at steep angles of incidence when used without anti-reflection coatings (e.g. the Fresnel loss is $\sim$ 45% at 80 degrees). This limits the utility of off-the-shelf Fresnel lenses, especially under the stringent focusing requirements needed to efficiently pipe the collected fluorescence light (which emerges from an extended source) into lightpipes.

A related piece of the light collection concept was the use of right-angle bent lightpipes, constructed out of two cylindrical lightpipes epoxied (using optically transparent Epo-tek 301) onto the faces of a right angle prism. This was conceived of as a way to allow the lightpipes to approach the fluorescence emission region through the downstream (yz plane) end of the vacuum chamber, while still presenting a perpendicular face towards the electric field plates. When the input ray bundle had a large angular spread, leakage through the 90 degree bend was found (through ray-tracing simulations) to be severe enough to limit the utility of this concept.

Hybrid photodetectors

Recall from Table 2.1 that the quantum efficiency of the detectors used at the end of the light collection system enters the sensitivity of the eEDM experiment. Pho-

tomultiplier tubes (PMTs) that are most sensitive to the emitted fluorescence (613 nm) have red-enhanced multi-alkali photocathodes, which yield a quantum efficiency of about 10% in this wavelength region. A higher quantum efficiency can be obtained by using detectors based on GaAsP photocathodes, which can have a quantum efficiency of about 40%. This would result in a factor of 2 improvement in the statistical sensitivity of the eEDM experiment. Therefore, PMTs using GaAsP photocathodes were examined as alternative options. Unfortunately, reasonably priced detectors with GaAsP photocathodes are only available in the form of hybrid photodetectors (HPDs). The HPD available from Hamamatsu (part number R9792U-40) has a photocathode biased at -8 kV to accelerate the photoelectrons emitted from the photocathode, which are then aimed at an avalanche diode. This provides an electron bombardment gain of about 1500. An additional gain of about 50 is obtained by biasing the avalanche diode at about 400 V. While this architecture does not have an overall gain as large as a typical PMT (and hence requires some further amplification), it is sufficient to make such a detector feasible for use in the experiment. One such HPD was obtained and tested in the summer of 2010 by Ana Malagon. The results of the test showed up a peculiar problem with these detectors, namely the appearance of extremely large current pulses (even in the absence of any light incident on the detector) at the rate of ~ 10/s. The manufacturer attributed these to bremsstrahlung X-rays produced when the photoelectrons accelerated by the large (8 kV) voltage are slammed into the avalanche diode, which in turn give rise to multiple photoelectron pulses. The appearance of such large pulses at a rate of $\sim$ 10/s was specified to be an unavoidable feature of the HPD architecture. Such large pulses are not a concern if the detector is used in photon counting mode, but as expected in the eEDM experiment, if they are used to detect the photocurrent (i.e. with a lower detection bandwidth) the energy contained in these large pulses cannot be kept from contaminating the signal. It is possible that operating the tube with a low acceleration voltage ($\sim$ 1 kV, rather than the manufacturer's recommended 8 kV) could eliminate the large bremsstrahlung pulses, at the expense of gain, but this was not a parameter range that had been tested by the manufacturer. As a result of these issues, and since the technology for the detectors did not seem to be sufficiently mature, the use of HPDs to detect fluorescence was abandoned in favor of off-the-shelf multi-alkali photocathode PMTs (R8900-20). At some time in the future, if detectors using GaAsP photocathodes (without any pathological noise features) can be obtained, they might be a competitive approach compared to PMTs

for detecting fluorescence from the molecules.

In-vacuum actuators

The fine pitch screws that are used on the linkages between the field plate sandwiches need to be manually adjusted to set the parallelism and spacing between the field plates. This means that, once the structure is assembled (and aligned) on the bench and placed inside the vacuum chamber, and the vacuum chamber is evacuated, the spacing and parallelism cannot be adjusted. This is not expected to be a problem in terms of the stability of the kinematic assembly, but it does mean that the vacuum chamber must be vented in order to adjust (or vastly misalign, for testing systematics) the parallelism of the field plates. An initial concept involved using actuators in vacuum, in order to adjust the spacing between the plates electrically and circumvent this problem. The constraints on these actuators are quite severe: they must be UHV compatible and non-magnetic. This rules out solutions such as motors or linear variable displacement transducers. Piezoelectric stacks were considered, but they have the twin disadvantages of (a) small throw, and (b) large quiescent current draw (enough to cause significant magnetic fields in the interaction region) when holding position. A good solution to these problems is provided by recent advances in piezoelectric motors, which use piezoelectric extensions ("legs") that ratchet across a bearing surface, and have the advantage that they lock in place when the driving voltage is set to zero. Therefore these actuators can be used to hold position without any quiescent leakage current. In particular, the LEGS-L01NMV-11 (Piezomotor.se/MicroMo) linear piezo actuator is rated for use in ultra-high vacuum and is constructed using non-magnetic alloys - the bearing and springs in it are constructed out of Be-Cu alloy, and the motor contains a non-magnetic copper-nickel alloy called ARCAP AP1D (UNS 79350). Unfortunately, the pushing force achievable with this actuator is limited to 10 N. The weight of the plate sandwiches is about 70 N. Also, spring tensions of $\sim$ 100 N are required to clamp the kinematic field plate assembly. Therefore single motors driving the kinematic linkages would not have the requisite force to actuate the plate spacing and parallelism under vacuum, without some sort of additional force multiplying linkages. Therefore, the use of in-vacuum actuators was not pursued. It is possible that technological advances in the next few years might lead to piezo motors with higher force ratings becoming available. Nevertheless, even the presently available piezo motors might be useful for

actuating other objects (e.g. collimators) under vacuum.

Bill of Materials

In designing many sub-components of the interaction region, that all had to fit together and remain modular enough to be useful, I found the use of a Bill of Materials (BOM) to be extremely helpful. BOMs are standard design tools in an industrial setting, but only rarely find use in physics instrument design. In the case of the interaction region of the ThO experiment, its use was justified by the large number of components and the need to

- Keep track of the various suppliers for components and specialty materials.
- Manage lead times for various components and fabricated parts, especially since they could easily vary from a few days to many months.
- Document the suppliers' part numbers of all the components, to be able to obtain equivalent replacement parts in the future.

The BOM for the interaction region of the ThO eEDM experiment is at `tinyurl.com/ThO-BOM`. A benefit of the BOM system is the automatic assignment of unique part numbers to all the components. This aided me in keeping track of part drawings and CAD models for the various assemblies and sub-assemblies, such as the electric field plates, magnetic shields, vacuum chamber components etc. during the design process, and led naturally to the design getting documented in detail. The use of such a system for complicated design projects is highly recommended.

Chapter 6

Summary

> His grenades are of wrong system.
>
> Semyon, *White Sun of the Desert*

This thesis records some of my contributions to the ThO eEDM experiment between Jan 2007 and Aug 2011. The factors that led to the choice of the ThO molecule for a molecular beam-based eEDM experiment have been explained in the Introduction. The scheme of the experiment, and an analysis of the noise entering the measurement, have been described in the Overview. Initial measurements of ThO molecular beam production, measurements of the lifetime, magnetic and electric dipole moments of the H state have been presented. These measurements feed into the estimated statistical sensitivity of the experiment and the analysis of potential systematics. Some of the pieces of the experiment's hardware that I designed and constructed have been described under Apparatus.

At the time of writing, the eEDM experiment has been assembled and can be used to obtain spin precession signals from ThO molecules in the beam. Some of the immediate next steps include demonstrating that the measurement of spin precession can be made with shot-noise limited sensitivity, and maximizing the statistical sensitivity that is expected with the current version of the apparatus (Table 2.1). Reaching this level of statistical uncertainty, $\delta d_e \sim 3 \times 10^{-29}$ e cm with an integration time of 1 day, would allow the experiment to quickly test systematic effects in the $10^{-27} - 10^{-28}$ e cm region. In the absence of systematic errors, this should allow the experiment to lower the uncertainty on the eEDM by 1 order of magnitude. A null measurement at this level would begin to seriously limit the parameter space of electro-weak baryogenesis.

Some further improvements are foreseeable, and they will be briefly mentioned here. First, note from (2.28) that, once the molecule has been chosen, both $\mathcal{E}_{mol}$ and τ are fixed. Therefore, the only parameter that can be optimized is the detection rate of molecules at the end of their precession. The following upgrades are likely to improve the detection rate:

- **Molecular beam source**: A thermo-chemical means of producing ThO, by taking advantage of a chemical reaction between ThO_2 and Th metal powders at ~ 2000 K which predominantly releases ThO in the gas phase [RFG+08], has been recently demonstrated in the Doyle group. A pressed target containing Th and ThO_2 powders, located inside a standard buffer gas cooling cell, is locally heated by a focused CW YAG laser. The buffer gas cools the molecules and extracts them into a molecular beam as usual. This method has the potential to produce a continuous beam of ThO, which could have a larger duty-cycle for the beam current compared to the pulsed ablation-based beam source.

- **Molecular beam divergence**: Reducing the loss of molecules during their flight through the dead length L_0 (see Section 2.4) would increase the detection rate. This can be achieved by shortening the apparatus, and/or by collimating the molecular beam. Molecules in the X state experience a quadratic Stark shift in $\mathcal{E}$-fields up to ~ 20 kV/cm, and can therefore be guided in weak field seeking states (e.g. $X, J = 1, m_J = 0$) using an electrostatic quadrupole guide. Some improvements along these lines have been demonstrated at a preliminary level in the DeMille group.

- **State transfer & state preparation**: The scheme laid out in the Overview used optical pumping from $X \to A \rightsquigarrow H$, which leads to a dilution by a factor of 0.07 between transferring a single quantum state in X into a single quantum state in H. This loss can be circumvented by using a coherent state transfer scheme such as STIRAP (STimulated Raman Adiabatic Passage), using the $X \leftrightarrow C \leftrightarrow H$ Λ-type system to transfer molecules from X to H. This can also eliminate the separate state preparation step, and directly populate the superposition of $H, J = 1|m_J = \pm 1\rangle$ that undergoes spin precession. Such schemes have been explored and preliminarily demonstrated in the DeMille group.

- **Geometric collection efficiency**: A larger geometric coverage of the fluo-

rescence emitted by the molecules would increase the detection rate. Some designs to improve the solid angle coverage of the light collection system have been explored by Nick Hutzler.

- **Detection efficiency**: Some approaches to improving the detection efficiency have been explored in the Doyle/DeMille/Gabrielse groups, such as the use of Si photodiodes instead of PMTs, to take advantage of their higher quantum efficiency. Other approaches to increase the detection efficiency include optical cycling schemes (where multiple independent photons are emitted by a single molecule) and ionization detection schemes (where the molecule is photo-ionized by a strong laser, and the ion is detected with a multi-channel plate detector). These approaches have the potential to provide almost 100% efficiency of detection of molecules in the beam.

At the time of writing, these schemes are being pursued and tested. I will not attempt to make any predictions about the sensitivity achievable with these upgrades, and will leave this to others who are more directly involved in these efforts. It is plausible, however, that 1 more order of magnitude in eEDM sensitivity can be gained through some combination of these improvements.

In summary, the saga of the search for the electric dipole moment of the electron continues. It is reasonable to expect that this experiment with the ThO molecule (along with other contemporary eEDM efforts) will lower the limit on the size of the eEDM enough to test electro-weak baryogenesis and other more creative proposals to explain the cosmological matter-antimatter asymmetry.

It is an audacious notion that, twirling knobs on some instrument in a basement lab, one might hope to shed some light on the evolution of the universe. For no other reason than this audacity alone, perhaps the search for an eEDM is worth pursuing.

Appendix A

Miscellany

"Two added to one – if that could but be done,"
It said, "with ones fingers and thumbs !"
Recollecting with tears how, in earlier years,
It had taken no pains with its sums.

The Hunting of the Snark, The Beaver's Lesson

A.1 P, T-violation and EDMs

The purpose of this section is to rigorously show that the existence of a permanent electric dipole moment in a quantum mechanical system requires the violation of both P and T symmetries. This is usually discussed in the context of the EDM of a spin-1/2 fermion f, where the P, T-transformation properties of the relativistic Hamiltonian, $H_{EDM} = -d_f \beta \vec{\Sigma} \cdot \vec{E}$, are directly used to prove this point [Sak64]. The proof is more involved for the case of a more general system, such as an atom or molecule, and it is shown here that non-zero expectation values of the permanent dipole moment operator require P and T-violation.

The EDM operator acting on the states of the system, say an atom, is $\vec{D}_a$. This is a polar vector operator. The Hamiltonian for its interaction with an external electric field is

$$H_{EDM} = -\vec{D}_a \cdot \vec{\mathcal{E}}. \tag{A.1}$$

Let P be the linear, Hermitian parity inversion operator. Consider an atomic state $|\psi\rangle$ in which the measurement is made. Inserting the identity operator $\mathbf{1} = P^{-1}P$,

the expectation value of the dipole moment can be shown to be zero:

$$\begin{aligned} \langle\psi|\vec{D}_a|\psi\rangle &= \langle\psi|P^{-1}\ P\vec{D}_a\hat{P}^{-1}\ P|\psi\rangle \\ &= -\langle\psi|\vec{D}_a|\psi\rangle \qquad \text{(A.2)} \\ \Rightarrow \langle\psi|\vec{D}_a|\psi\rangle &= 0. \qquad \text{(A.3)} \end{aligned}$$

This is valid whenever $|\psi\rangle$ is an eigenstate of the parity operator: $P|\psi\rangle = \pm|\psi\rangle$, and relies on the fact that the dipole moment is a polar vector that is odd under parity: $P\vec{D}_a\hat{P}^{-1} = -\vec{D}_a$. Therefore, the measurement of a nonzero expectation value for a dipole moment implies that the state $|\psi\rangle$ is not an eigenstate of parity.

Now for T-invariance, which corresponds to motion-reversal invariance. This proof is based on the discussion of T-invariance in [San68a, Sak85]. Let Θ be the antiunitary T-inversion operator. Let $|\psi\rangle$ be an angular momentum eigenstate $|J, m_J\rangle$ with integer J, as is the case for ThO. Under the action of the Θ operator, the ket $|J, m_J\rangle \rightarrow \Theta|J, m_J\rangle = (-1)^{m_J}|J, -m_J\rangle$. The dipole moment operator is even under the action of the Θ operator: $\Theta\vec{D}_a\Theta^{-1} = +\vec{D}_a$. We again make use of the identity operator $\mathbf{1} = \Theta^{-1}\Theta$ and find that

$$\begin{aligned} \langle J, m_J|\vec{D}_a|J, m_J\rangle &= \langle J, m_J|\Theta^{-1}\ \Theta\vec{D}_a\Theta^{-1}\ \Theta|J, m_J\rangle \\ &= +\langle J, -m_J|\vec{D}_a|J, -m_J\rangle. \qquad \text{(A.4)} \end{aligned}$$

Assume next that the matrix element of the $\hat{z}$-component of $\vec{D}_a$ is evaluated (the matrix elements of the other components can be obtained from this $\hat{z}$-component using the Wigner-Eckart theorem). We have

$$\langle J, m_J|D_{a,z}|J, m_J\rangle = +\langle J, -m_J|D_{a,z}|J, -m_J\rangle. \qquad \text{(A.5)}$$

under the action of the Θ operator.

Now we make use of the rotation operator $R_\pi = \mathcal{D}(0, \pi, 0)$, which corresponds to a rotation about the y-axis by 180 degrees. Under the action of this operator, the kets transform as $R_\pi|J, -m_J\rangle = e^{i\phi}|J, +m_J\rangle$, and the operator $D_{a,z}$ transforms as $R_\pi D_{a,z}R_\pi^{-1} = (-1)D_{a,z} + R_{\pi,zx}D_{a,x} + R_{\pi,zy}D_{a,y}$.[1]. Inserting R_π through the identity

[1]These results can be obtained from (A.13) and (A.14) See also Equation (3.10.22) in [Sak85].

operator $\mathbf{1} = R_\pi^{-1} R_\pi$, we have

$$\begin{aligned}
\langle J, m_J | D_{a,z} | J, m_J \rangle &= +\langle J, -m_J | D_{a,z} | J, -m_J \rangle \\
&= \langle J, -m_J | R_\pi^{-1}\ R_\pi D_{a,z} R_\pi^{-1}\ R_\pi | J, -m_J \rangle \\
&= \langle J, m_J | e^{-i\phi}\ [(-1) D_{a,z} + R_{\pi,zx} D_{a,x} + R_{\pi,zy} D_{a,y}]\ e^{i\phi} | J, m_J \rangle \\
&= -\langle J, m_J | D_{a,z} | J, m_J \rangle. \qquad \text{(A.6)} \\
\Rightarrow \langle J, m_J | D_{a,z} | J, m_J \rangle &= 0 \qquad \text{(A.7)}
\end{aligned}$$

In the penultimate step, the matrix elements of $D_{a,x}, D_{a,y}$ are set to zero between states with identical m_J. We therefore find that the measurement of a non-zero expectation value of $\vec{D}_a$ requires a violation of the transformation properties of angular momentum states under the action of the T-operator.

A.2 State mixing in an electric field

Consider two states $|p\rangle$ and $|q\rangle$ that have opposite parity and have an energy difference $\Delta_{pq} = E_p - E_q$ between them. If they both have the same eigenvalue of J_z, they can be mixed by the electric field $\vec{\mathcal{E}} = \mathcal{E}\hat{z}$. Let the matrix element of the dipole moment operator between them be $\langle p | D_z | q \rangle \equiv D_{pq}$. The eigenvectors in the electric field are given exactly by:

$$\begin{aligned}
|\widetilde{p}\rangle &= |p\rangle \cos\xi/2 + |q\rangle \sin\xi/2 \\
|\widetilde{q}\rangle &= |q\rangle \cos\xi/2 - |p\rangle \sin\xi/2 \qquad \text{(A.8)}
\end{aligned}$$

where $\tan\xi = \frac{-D_{pq}\mathcal{E}}{\Delta_{pq}/2}$. In the limit when $D_{pq}\mathcal{E} \ll \Delta_{pq}/2$ (i.e. when $\tan\xi \approx \xi$), the eigenvectors are

$$\begin{aligned}
|\widetilde{p}\rangle &\approx |p\rangle + |q\rangle \frac{-D_{pq}\mathcal{E}}{\Delta_{pq}} \\
|\widetilde{q}\rangle &\approx |q\rangle + |p\rangle \frac{D_{pq}\mathcal{E}}{\Delta_{pq}}. \qquad \text{(A.9)}
\end{aligned}$$

This is the *weakly polarized regime*. In the opposite limit, when $|\tan\xi| \gg 1$, the eigenvectors are

$$\begin{aligned} |\widetilde{p}\rangle &\approx \frac{|p\rangle - |q\rangle}{\sqrt{2}} \\ |\widetilde{q}\rangle &\approx \frac{|q\rangle + |p\rangle}{\sqrt{2}}. \end{aligned} \tag{A.10}$$

This is the *strongly polarized regime*. These expressions are useful in understanding the effect of the $\mathcal{E}$-field on the various energy levels in the ThO molecule.

A.3 Matrix elements between molecular states

For the evaluation of matrix elements between states in a diatomic molecule, the lab-to-molecule frame transformation formula is often useful. The formula can be found in [Dra06], Section 33.2. What follows is a simple derivation. The aim is to obtain the matrix elements of a spherical tensor operator T^k_Q between two molecular eigenstates of angular momentum: $|J, M, \Omega; \Gamma\rangle$ and $|j, m, \omega; \gamma\rangle$. Here J is the angular momentum of the state, M is the projection of J onto the lab $\hat{z}$-axis, Ω is the projection of J onto the intra-molecular axis $\hat{n}$, and Γ is a set of molecule-fixed quantum numbers unrelated to the rotational properties of the state. Hund's case (c) molecular states can be written as a product of symmetric top wavefunctions $|J, M, \Omega\rangle$ and molecule-fixed wavefunctions $|\Omega; \Gamma\rangle$,

$$|J, M, \Omega; \Gamma\rangle = |J, M, \Omega\rangle \times |\Omega; \Gamma\rangle \tag{A.11}$$

where the symmetric top part of the wavefunction, $|J, M, \Omega\rangle$, contains all the information about the transformation properties of the molecular state under the rotation group $SO(3)$ (i.e. 3D rotations) [Hou01]. The representation of the $|J, M, \Omega\rangle$ symmetric top wavefunctions in terms of Euler angles is

$$\langle\Theta|J, M, \Omega\rangle = \sqrt{\frac{2J+1}{8\pi^2}}\, \mathcal{D}^J_{M\Omega}(\Theta) \tag{A.12}$$

where $\mathcal{D}^J(\Theta)$ is the Wigner rotation matrix for angular momentum J, and Θ is a convenient shorthand for the triplet of Euler angles (θ, ϕ, α) [Dav76](Eq. 45.5).

A lab-frame angular momentum eigenstate state, with angular momentum J and

lab frame $\hat{z}$-projection M, transforms under rotations by a set of Euler angles (θ, ϕ, α) as

$$|J, M\rangle = \sum_m \mathcal{D}^J_{Mm}(\Theta)\ |J, m\rangle. \tag{A.13}$$

Spherical tensor operators transform like angular momentum eigenstates. A spherical tensor operator T^k_Q with the lab-frame azimuthal index Q can be transformed into the molecule-fixed frame and written in terms of the azimuthal index q as

$$T^k_Q = \sum_q \mathcal{D}^k_{Qq}(\Theta) T^k_q \tag{A.14}$$

Using the following property of the $\mathcal{D}^J$ matrices [Dav76](Eq. 43.24)

$$\begin{aligned}\int \mathcal{D}^{J*}_{MK}(\Theta)\mathcal{D}^{j_1}_{m_1k_1}(\Theta)\mathcal{D}^{j_2}_{m_2k_2}(\Theta)\ d\Theta &= \frac{8\pi^2}{2J+1}\langle J, M|j1, m_1; j2, m_2\rangle \\ &\quad\times\langle J, K|j1, k_1; j2, k_2\rangle\end{aligned} \tag{A.15}$$

we get the lab-to-molecule transformation formula, relating the rotational properties of matrix elements between two molecular states to Clebsch-Gordan coefficients:

$$\begin{aligned}\langle J, M, \Omega; \Gamma|T^k_Q|j, m, \omega; \gamma\rangle &= \sqrt{\frac{2J+1}{8\pi^2}}\sqrt{\frac{2j+1}{8\pi^2}}\sum_q \int \mathcal{D}^{J*}_{M\Omega}\mathcal{D}^k_{Qq}\mathcal{D}^j_{m\omega}\ d\Theta \\ &= \sum_q \sqrt{\frac{2j+1}{2J+1}}\langle J, M|k, Q; j, m\rangle \\ &\quad\times\langle J, \Omega|k, q; j, \omega\rangle\langle\Gamma; \Omega|T^k_q|\gamma; \omega\rangle.\end{aligned} \tag{A.16}$$

Here $\langle\Gamma; \Omega|T^k_q|\gamma; \omega\rangle$ is a matrix element in the molecule-fixed frame, that depends on the details of the molecular wavefunction, but is independent of rotations. The result is valid for Hund's case (c) basis functions, whose transformation properties under rotations are described by symmetric top wavefunctions [Hou01]. Other Hund's case eigenstates might have to be expressed as superpositions of case (c) eigenfunctions before this formula can be applied.

Corollary: Wigner-Eckart theorem

An amusing corollary of the lab-to-molecule transformation formula is the Wigner-Eckart theorem, usually encountered in connection to matrix elements in atoms. For regular spherical harmonics, $|J, M\rangle = |J, M, \Omega = 0\rangle$ and we obtain the usual

Wigner-Eckart theorem

$$\langle J, M; \Gamma | T^k_Q | j, m; \gamma \rangle = \langle J, M | k, Q; j, m \rangle \langle J; \Gamma | T^k_0 | j; \gamma \rangle. \tag{A.17}$$

A.4 Simple picture of Ω-doublets

Ω-doublets are closely spaced states of opposite parity that show up in molecular states which have a nonzero projection of the electronic angular momentum $\vec{J_e}$ onto the internuclear axis $\hat{n}$ ($\Omega = \vec{J_e} \cdot \hat{n}$). Physically, in a diatomic molecule with nonzero angular momentum about the symmetry axis, there are two degrees of freedom corresponding to electrons orbiting clockwise or anti-clockwise about the axis. These are the degrees of freedom that lead to Ω-doubling. The same effect (known as "parity doubling") also occurs in deformed nuclei. In molecular physics literature, this is sometimes also referred to as Λ-doubling ($\Lambda = \vec{L_e} \cdot \hat{n}$), since the main ideas are independent of whether the electronic angular momentum $\vec{J_e} = \vec{L_e} + \vec{S}$ contains a contribution solely from the electronic orbital angular momentum $\vec{L_e}$ or not. It is simplest to have a physical picture for this in terms of the orbital angular momentum (since the wavefunctions in real space can visualized easily). Also, the H state in ThO is a good Hund's case (a) molecular state (with $\Lambda = 2$) and it is not incorrect to think of the Ω-doubling in the H state as being equivalent to Λ-doubling. In states with strong spin-orbit coupling, this picture is not totally accurate, and one must fall back on the mathematics. The full quantum-mechanical approach to Ω-doubling is treated in detail in [BC03, LL81]. For completeness, a short summary is given below (in general terms, using $\vec{J_e}$ instead of $\vec{L_e}$).

The rotation of the molecule is governed by the Hamiltonian $H_r = BN^2$, where B is the rotational constant of the molecule and N is the rotational angular momentum of the two atoms about their center of mass. In terms of the reduced mass of the two atoms M and their separation R, $B = 1/2MR^2 = 1/I_M$, where I_M is the moment of inertia of the rotating molecule. The total angular momentum $\vec{J} = \vec{N} + \vec{J_e}$ is the only good quantum number in the rotating molecule. H_r can be rewritten in terms of J as

$$H_r = B(\vec{J} - \vec{J_e})^2 = BJ^2 - 2B\vec{J} \cdot \vec{J_e} + BJ_e^2. \tag{A.18}$$

Further BJ_e^2 is independent of the rotational quantum number J and is a constant for a given electronic state, so it only contributes to the baseline energy of the electronic state. BJ^2 gives rise to the usual rotational ladder of states. The term in

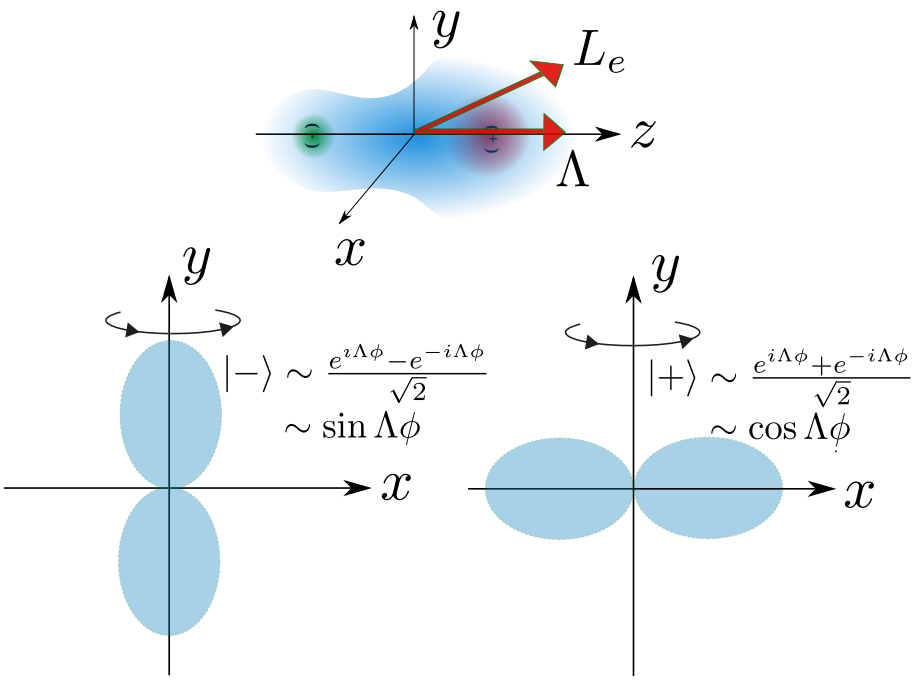

Figure A.1: The illustration at the top schematically shows the angular momentum vectors in the molecule-fixed frame. The illustration below show the azimuthal probability density of the electrons in the even and odd combinations of the molecule-fixed eigenvectors $|\Lambda\rangle$ in a $\Lambda = 1$ electronic state.

the Hamiltonian that is responsible for Ω-doubling is the so-called Coriolis coupling $H_{Cor} = -2B\vec{J}\cdot\vec{J}_e$. This can be rewritten in terms of the usual raising and lowering operators for J and J_e, referred to the internuclear axis $\hat{n}$, as

$$H_{Cor} = -2B(\Omega^2 - J^-J_e^+ - J^+J_e^-) = \text{const.} + 2B(J^-J_e^+ + J^+J_e^-) \tag{A.19}$$

where $\vec{J}\cdot\hat{n} = \vec{J}_e\cdot\hat{n} = \Omega$ ($\hat{N}$ is orthogonal to $\hat{n}$). Hence $-2B\Omega^2$ is yet another J-independent constant term added to the baseline energy.

The appearance of the off-diagonal terms $J^{\pm}J_e^{\mp}$ in H_{Cor} leads to a coupling between an electronic state with quantum number $\Omega = \Omega_0$ and those with $\Omega = \Omega_0 \pm 1$. In the absence of this coupling, electronic states with $\Omega = \pm\Omega_0$ are degenerate in energy. Under the influence of H_{Cor}, these are coupled through a chain of intermediate states $|\Omega_0 - 1\rangle, |\Omega_0 - 2\rangle ... |-\Omega_0 + 1\rangle$ at $(2\Omega_0)$-th order in perturbation theory, and acquire a slight energy difference. This is what leads to Ω-doubling.

In the following, a simple physical reason for the appearance of these doublets is presented, in the hope that this might provide some intuition. Consider the polar

molecule shown in Figure A.1. As mentioned above, it is sufficient to consider Λ-doubling, arising from the non-zero orbital angular momentum of the electrons about the space-fixed internuclear axis. The two degenerate degrees of freedom, in the non-rotating molecule, correspond to positive or negative projections of $\vec{L}_e$ along $\hat{n}$. The amplitude for the states $|\pm\Lambda\rangle$ at an azimuthal angle ϕ about $\hat{n}$ is $\sim e^{\pm i\Lambda\phi}$, leading to a uniform probability density about the internuclear axis (as expected for a cylindrically symmetric system). As these are degenerate states, we can equally generally consider a pair of orthogonal states formed from their superpositions:

$$|\pm\rangle = \frac{|\Lambda\rangle \pm |-\Lambda\rangle}{\sqrt{2}} \tag{A.20}$$

These have probability densities proportional to $\cos(\Lambda\phi)$ ($\sin(\Lambda\phi)$), and for $\Lambda = 1$ are peaked along the x (y) axis referred to the molecule-fixed frame (where $\hat{n} \equiv \hat{z}$). In the lab-frame, rotation of the atoms about their center of mass corresponds to a rotation of the probability densities shown in Figure A.1 about the molecule-fixed x or y axes. Without loss of generality, say the molecule rotates about y (in other words, the y-axis can always be aligned with the axis of rotation of the molecule by a choice of the zero of azimuthal angle ϕ). It is evident that electrons in $|+\rangle$ have a different moment of inertia I_e about the axis of rotation than electrons in $|-\rangle$, and therefore pick up different amounts of kinetic energy due to the rotation of the molecule as a whole. This energy difference ΔE can be readily estimated, since the spatial extent of the lobe of the wavefunction is $\sim a_0$.

$$\begin{aligned} \Delta E &= \frac{1}{2}\Delta I_e \omega^2 \\ &\sim \frac{1}{2} m_e a_0^2 \Big(\frac{J}{I_M}\Big)^2 = \frac{m_e a_0^2}{4MR^2} J^2 \\ &\sim \frac{m_e}{M}\ J(J+1), \end{aligned} \tag{A.21}$$

recognizing that the typical inter-atomic spacing R in a molecule is on the order of a Bohr radius a_0. This simple argument gives the right size and J-scaling of the Λ-doubling in a molecule with $\Lambda = 1$. The appearance of the ratio of the mass of the electrons to the mass of the atoms, m_e/M, reminds us that the key physics behind Ω-doubling is a "dragging" of the electrons by the atoms in the molecule as they rotate in the lab-frame. It can also be seen why, for $\Lambda > 1$, the difference between the moments of inertia of electrons in $|+\rangle$ and $|-\rangle$ gets smaller as the lobes in the

azimuthal probability density become more azimuthally symmetric.

A.5 Magnetic Johnson noise

The charge carriers in a conductor thermalize due to collisions with phonons in the material. At a temperature T, the charge carriers are in equilibrium with a thermal bath of phonons, and as a result the velocities of the charge carriers fluctuate in time. This leads to fluctuating currents in the conductor, which in turn generate fluctuating magnetic fields in the vicinity of the conductor. These fluctuating magnetic fields are referred to as magnetic Johnson noise. The spectral density of magnetic Johnson noise from a conductor is calculated here in a simple form. Alternative expressions for the magnetic Johnson noise can be found in [Lam99, Mun05].

In a small volume element $\delta\Upsilon_i$ of the conductor, the spectral density of the current density j is

$$j_\nu = \sqrt{\frac{4k_B T}{\rho\ \delta\Upsilon_i}} \tag{A.22}$$

where ρ is the resistivity of the material. At a distance $\vec{r}_i$ from the volume element, the power spectral density of the magnetic field due to the fluctuating current density is

$$\widetilde{\mathcal{B}_{\nu,i}} = \frac{\mu_0}{4\pi}\frac{\vec{j}_\nu \times \vec{r}_i}{r_i^3}\delta\Upsilon_i. \tag{A.23}$$

The squared cross product $(\vec{j}_\nu \times \vec{r}_i)^2$, which we will need below, can be simplified as

$$(\vec{j}_\nu \times \vec{r}_i)^2 = j_\nu^2\, r_i^2 - (\vec{j}_\nu \cdot \vec{r}_i)^2 \approx \frac{2}{3}\, j_\nu^2\, r_i^2 \tag{A.24}$$

when averaged over the orientations of $\vec{j}_\nu$ with respect to $\vec{r}_i$. Using the fact that Johnson currents in different volume elements are uncorrelated,[2] the spectral density of the $\mathcal{B}$-field can be obtained from the quadrature sum of the $\mathcal{B}$-fields due to different

[2]The typical correlation length for thermal noise currents is on the order of the mean free path of electrons in the conductor.

volume elements.

$$\begin{aligned} \widetilde{\mathcal{B}_\nu} &= \sqrt{\sum_i (\widetilde{\mathcal{B}_{\nu,i}})^2} = \left(\frac{\mu_0}{4\pi}\right)\sqrt{\sum_i \frac{8k_BT}{3\rho}\frac{\delta\Upsilon_i}{r_i^4}} \\ \mapsto \quad \widetilde{\mathcal{B}_\nu} &= \left(\frac{\mu_0}{4\pi}\right)\sqrt{\frac{8k_BT}{3\rho}\int\frac{d\Upsilon}{r^4}} \end{aligned} \tag{A.25}$$

The geometry of the conductors enters through the shape factor $\mathfrak{S} = \int d\Upsilon/r^4$. For example, at the center of a cylindrical shell of radius R, thickness ΔR and height H the shape factor is $\mathfrak{S} = 2\pi\ \tan^{-1}\left(\frac{H}{2R}\right)\frac{\Delta R}{R^2}$, while for a sphere of radius R and thickness ΔR it is $\mathfrak{S} = 4\pi\Delta R/R^2$, about the same order of magnitude as a cylinder with $H \sim R$. It can be seen from (A.25) that in general, $\mathfrak{S} \sim t/R^2$ for a conductor of thickness t that is located at a distance R from the point of evaluation.

We now estimate $\widetilde{\mathcal{B}_\nu}$ for the aluminum vacuum chamber described in Section 5.3. For the purpose of this estimate, it is modeled as a cylinder with radius $R = 8$ in. height $H = 25$ in. and thickness $\Delta R = 5/8$ in., and the shape factor thus obtained is $\mathfrak{S} = 1.9\ \text{m}^{-1}$. This shape factor and the electrical conductivity of 6061 alloy, $\rho_{Al} = 4 \times 10^{-8}\ \Omega$ m, are substituted in (A.25) to obtain $\widetilde{\mathcal{B}_\nu} \approx 70\ \text{fT}/\sqrt{\text{Hz}}$.

A.6 Cross-polarization in Gaussian beams

Even propagating through free space, a polarized Gaussian light beam picks up new polarization components ("cross polarization") purely as a consequence of propagation according to the wave equation. The curvature of the wavefront of a converging/diverging Gaussian beam is a well-known effect. The appearance of cross-polarization components can be understood as arising due to the constraint (from Maxwell's equations) that the $\mathcal{E}$- and $\mathcal{B}$-field vectors in free space have to always be transverse to the converging/diverging wavefront. The curvature of the wavefront rotates the $\mathcal{E}$ and $\mathcal{B}$-vectors as the beam propagates. Since the preparation and detection of the spin superposition in the H state relies on the polarization of laser beams, it is plausible that the appearance of cross-polarization components could mimic the rotation of the preparation and detection bases for spin precession in the H state, and cause systematic effects. In the following section, an elementary derivation of the cross-polarization effect is presented and an estimate of the size of the cross-polarization components is obtained.

The electromagnetic wave equation is

$$(\nabla^2 - \partial_t^2)\vec{\mathcal{E}} = 0. \tag{A.26}$$

The derivation of this equation uses the following free-space Maxwell equations, which are constraints to be satisfied by the solutions and initial conditions of the wave equation.

$$\vec{\nabla} \cdot \vec{\mathcal{E}} = 0 \tag{A.27}$$

$$\vec{\nabla} \times \vec{\mathcal{E}} = -\partial_t \vec{\mathcal{B}} \tag{A.28}$$

Assuming $\vec{\mathcal{E}} \sim e^{-i\omega t}$ we get the following Helmholtz equation for the spatial dependence of the electric and magnetic fields

$$(\nabla^2 + k^2)\vec{\mathcal{E}} = 0 \tag{A.29}$$

with $k^2 = \omega^2$. The simplest solutions of this equation are (unphysical) infinite plane waves $\vec{\mathcal{E}} \sim e^{i\vec{k}\cdot\vec{x}}$. To get a description of 'finite' beams, we make the assumption that $\vec{\mathcal{E}} \sim \vec{\mathcal{E}}(x, y, z)e^{ikz}$ where $\vec{\mathcal{E}}(x, y, z)$ is a slowly varying function of z. The meaning of 'slowly varying' will become a bit clearer further on. With this slowly varying envelope approximation, the Helmholtz equation becomes the *paraxial wave equation*

$$ik\frac{\partial \vec{\mathcal{E}}}{\partial z} = -\frac{1}{2}(\partial_x^2 + \partial_y^2)\vec{\mathcal{E}} \tag{A.30}$$

where the approximation is valid if $(\partial_x^2 + \partial_y^2)\vec{\mathcal{E}} \ll k^2\vec{\mathcal{E}}$. First, we assume separation of the variables (x, y) and z and use the linearity of the wave equation to write

$$\vec{\mathcal{E}}(x, y, z) = \int d^2k\ \vec{\mathcal{E}}(k_x, k_y, z)e^{ik_x x}e^{ik_y y} \tag{A.31}$$

The paraxial wave equation can be solved for the z-dependence of the field

$$\frac{1}{\mathcal{E}}\frac{\partial \mathcal{E}}{\partial z} = -i(k_x^2 + k_y^2)/2k \tag{A.32}$$

$$\Rightarrow \vec{\mathcal{E}}(k_x, k_y, z) = \vec{\mathcal{E}}(k_x, k_y)e^{-i\ (k_x^2+k_y^2)z/2k} \tag{A.33}$$

and the full solution is

$$\vec{\mathcal{E}}(z) = \int d^2k_\perp \; \vec{\mathcal{E}}(k_\perp) \; e^{i\vec{k}_\perp \cdot \vec{x}_\perp} e^{ikz} e^{-ik_\perp^2 z/2k} \tag{A.34}$$

where $\vec{k}_\perp$ is shorthand for the transverse vector (k_x, k_y). Note that $k - \frac{k_\perp^2}{2k} \simeq \sqrt{k^2 - k_\perp^2} = k_z$, at a level of approximation consistent with the paraxial approximation. The notion of slow variation can now be made more precise: *the paraxial approximation consists of retaining terms up to* $\mathcal{O}(k_\perp^2/k^2)$.

The constraints that has to be satisfied by the field vector in (A.34) are

$$\begin{aligned} \vec{\nabla} \cdot \vec{\mathcal{E}} &= k_x \mathcal{E}_x(\vec{k}_\perp) + k_y \mathcal{E}_y(\vec{k}_\perp) + k_z \mathcal{E}_z(\vec{k}_\perp) = 0 \\ \Rightarrow \mathcal{E}_z &= -\frac{\vec{k}_\perp}{k} \cdot \vec{\mathcal{E}_\perp} + o(k_\perp^2/k^2) \end{aligned} \tag{A.35}$$

$$\vec{\mathcal{B}} = \hat{k} \times \vec{\mathcal{E}} \;\; \text{(alternatively, a definition of the B-field vector)} \tag{A.36}$$

Scalar Gaussian beams

To first get some insight, we ignore the vector nature of the field (A.35) and consider just the scalar wave equation. Different choices of the envelope function $\mathcal{E}(k_\perp)$ result in different propagating beam profiles. The simplest choice $\mathcal{E}(k_\perp) = \mathcal{E}_0 = const.$ gives the Fresnel solution $\mathcal{E} \sim \mathcal{E}_0 e^{ikx_\perp^2/2z}$. This corresponds to the beam diverging from a perfect point source at $z = 0$. The 'radius of curvature' here is equal to z.

A more physical choice is a Gaussian wavepacket $\mathcal{E}(k_\perp) = \mathcal{E}_0 e^{-k_\perp^2 w^2/2}$ with a waist w in the plane with $z = 0$. A light beam from a laser, for example, corresponds to such a wavepacket. The corresponding spatial profile at $z \neq 0$ is

$$\begin{aligned} \mathcal{E}(z) &= \int d^2k_\perp \; \mathcal{E}_0 e^{-k_\perp^2 w^2/2} \; e^{i\vec{k}_\perp \cdot \vec{x}_\perp} e^{ikz} e^{-ik_\perp^2 z/2k} \\ &= \int d^2k_\perp \; \mathcal{E}_0 e^{-ik_\perp^2 \widetilde{z}/2k} \; e^{i\vec{k}_\perp \cdot \vec{x}_\perp} e^{ikz} && \text{(A.37)} \\ &= \int d^2k_\perp \; \mathcal{E}_0 e^{-k_\perp^2 \widetilde{w}^2/2} \; e^{i\vec{k}_\perp \cdot \vec{x}_\perp} e^{ikz} && \text{(A.38)} \\ &= \mathcal{E}_0 \; \frac{\pi}{\widetilde{w}^2} \; e^{-x_\perp^2/2\widetilde{w}^2} e^{ikz} = \mathcal{E}_0 \; \frac{\pi k}{\widetilde{z}} \; e^{ikx_\perp^2/2\widetilde{z}} e^{ikz} && \text{(A.39)} \end{aligned}$$

$$\Rightarrow \mathcal{E}(z) = \mathcal{E}(0) \; \frac{w^2}{w(z)^2} \; e^{-x_\perp^2/2w(z)^2} e^{ikx_\perp^2/2R(z)} e^{ikz} e^{-i\phi(z)} \tag{A.40}$$

where $\widetilde{w}^2 = w^2 + iz/k$ and $\widetilde{z} = z - ikw^2$. We define the *Rayleigh range* $z_R = kw^2$, the *radius of curvature* $R(z) = z + z_R^2/z$ and the beam waist $w(z) = w\sqrt{1 + \frac{z^2}{z_R^2}}$. The phase of the complex numbers $\widetilde{w}^2, \widetilde{z}$ appearing as normalization factors in (A.39) leads to the *Guoy phase*, $\phi(z) = \tan^{-1}(z/z_R)$.

Vector Gaussian beams

The exact vector Gaussian beam can be obtained from the general solution of the paraxial equation (A.34, A.35). We write the vector electric field, following a Gaussian spatial filter and an $\hat{x}$-oriented linear polarizer, in terms of its plane wave components

$$\vec{\mathcal{E}} = \int d^2k_\perp \; \mathcal{E}_0 e^{-k_\perp^2 w^2/2} \; e^{i\vec{k}_\perp \cdot \vec{x}_\perp} \begin{pmatrix} 1 \\ 0 \\ 0 \end{pmatrix}. \tag{A.41}$$

This field contains a propagating far field component satisfying the free space constraint $\vec{k} \cdot \vec{\mathcal{E}}(\vec{k}) = 0$, and the remainder a non-propagating near field component which satisfies the boundary conditions appropriate for the dielectrics and conductors in the filter and polarizer. The propagating part of the field vector can be isolated using the projection operator (matrix) $\hat{\mathcal{P}}(\vec{k}) = \mathbf{1} - \vec{k} \otimes \vec{k}/k^2 \simeq \mathbf{1} - \hat{z} \otimes \hat{z} - \vec{k}_\perp \otimes \vec{k}_\perp / k^2$, with the paraxial approximation used in the last step. The spatial profile of the propagating vector wave can now be obtained by integrating the propagating part of the initial wave field with the usual Gaussian kernel $e^{-ik_\perp^2 \widetilde{z}/2k}$.

The propagating Gaussian beam is therefore

$$\vec{\mathcal{E}} = \int d^2k_\perp \; \mathcal{E}_0 e^{-k_\perp^2 w^2/2} \; e^{i\vec{k}_\perp \cdot \vec{x}_\perp} e^{ikz} e^{-ik_\perp^2 z/2k} \; \hat{\mathcal{P}}(\vec{k}_\perp) \begin{pmatrix} 1 \\ 0 \\ 0 \end{pmatrix}. \tag{A.42}$$

Using the projection operator acting on the $\hat{x}$ unit vector

$$\hat{\mathcal{P}}(\vec{k}_\perp) \begin{pmatrix} 1 \\ 0 \\ 0 \end{pmatrix} = \begin{pmatrix} 1 - k_x^2/k^2 \\ -k_x k_y/k^2 \\ -k_x/k \end{pmatrix} \tag{A.43}$$

the cross polarization components of the propagating wave are already evident. The

propagating vector wave is

$$\begin{aligned}\vec{\mathcal{E}}(z) &= \mathcal{E}_0 e^{ikz} \int d^2k_\perp \; e^{-k_\perp^2 \tilde{w}^2/2} \; e^{i\vec{k}_\perp \cdot \vec{x}_\perp} \begin{pmatrix} 1 - k_x^2/k^2 \\ -k_x k_y/k^2 \\ -k_x/k \end{pmatrix} \\ &= \mathcal{E}_0 e^{ikz} \int d^2k_\perp \; e^{-ik_\perp^2 \widetilde{z}/2k} \; e^{i\vec{k}_\perp \cdot \vec{x}_\perp} \begin{pmatrix} 1 - k_x^2/k^2 \\ -k_x k_y/k^2 \\ -k_x/k \end{pmatrix} \end{aligned} \tag{A.44}$$

After performing the integration, we get the exact solution

$$\vec{\mathcal{E}}(z) = \mathcal{E}(0) \; \frac{w^2}{w(z)^2} \; e^{-x_\perp^2/2w(z)^2} e^{ikx_\perp^2/2R(z)} e^{ikz} e^{-i\phi(z)} \begin{pmatrix} 1 - x^2/\widetilde{z}^2 - i/k\widetilde{z} \\ -xy/\widetilde{z}^2 \\ -x/\widetilde{z} \end{pmatrix} \tag{A.45}$$

The $\mathcal{B}$ field can be obtained in a similar way. Note that this vector Gaussian beam field is exactly divergence-free (up to the paraxial approximation). This result is identical to that in [SSM86, SSM87], but has been obtained without using any group theoretical machinery.

In summary, when a Gaussian beam that is $\hat{x}$-polarized at $(x, y) = (0, 0)$ propagates, there are new polarization components that emerge:

1. There is a longitudinal ($\hat{z}$) component with amplitude $\mathcal{E}_z \sim \mathcal{E}_x x/\widetilde{z}$. Recall that $\widetilde{z} = z - ikw^2$, so the longitudinal component has a relative magnitude $\frac{\mathcal{E}_z}{\mathcal{E}_x} \lesssim (x/w)(\lambda/w)$.

2. Compared to the principal transverse ($\hat{x}$) component, the transverse cross-polarization ($\hat{y}$) component has a relative magnitude $\frac{\mathcal{E}_y}{\mathcal{E}_x} \lesssim (xy/w^2)(\lambda^2/w^2)$.

Appendix B

Geometric phases from energy shifts

> There are nine and sixty ways of constructing tribal lays,
> And every single one of them is right !
>
> Rudyard Kipling, *In the Neolithic Age*

[1]Geometric phases arise in a number of physical situations and often lead to systematic shifts in frequencies or phases measured in precision experiments [Com91, PHS$^+$04, LG05]. This investigation was motivated by the question of how geometric phase effects, which were one of the limiting systematic errors in the Tl EDM experiment [RCSD02], would play a part in the ThO experiment. With the complicated level structure (Ω-doublets) and strong $\mathcal{E}$-field effects in the H state, it was initially unclear whether/how the standard formulation of the geometric phase (in terms of the slowly evolving trajectory of eigenstates, usually formulated for a spin-1/2 particle in a $\mathcal{B}$-field, e.g. as in [Gri05]) could be carried over to this problem. The key insight, essentially contained in [Ram55], is that it is *always* sufficient to just evaluate the off-resonant energy level shifts due to the perturbing fields (be they electric or magnetic), and calculate the phase picked up due to these energy shifts in the usual way. The purpose of this Appendix is to provide some worked examples for a number of interesting systems, and to show how the usual geometric result can always be obtained as a limiting case using standard *algebraic* methods of calculation.

A geometric phase, often also referred to as an "adiabatic phase" or "Berry's

[1]Significant chunks of this chapter are based on [VD09], which was written for a pedagogical journal.

phase", is a real, physical phase shift that can lead to measurable effects in experiments ([BD87, RKGL88, Com91] are some examples). In the classic version of this effect, the state of a particle with a magnetic moment is modified under the influence of a magnetic field which undergoes a slow change in its direction. The motion of the field leads to a phase shift accumulated between the quantum states of the particle, in addition to the dynamical phase due to the Larmor precession of the magnetic moment around the magnetic field. This extra phase is termed a geometric phase because it can be interpreted in terms of the geometry traced out by the system's Hamiltonian as it evolves in its parameter space. [Hol89] and references within contain a good discussion of the standard geometric approach to calculating geometric phases, and its various connections with the topology of the parameter space.

In practice, calculating geometric phases can be non-trivial when the path traced out in the parameter space is not a closed loop [AWM95]. In addition the geometric formulation is strictly correct only in the limit of slow evolution, and corrections due to finite evolution speed can be important in some situations [AWM95, FHLR05]. Finally, the topology of multi-dimensional parameter spaces can become quite involved when the system is an atom or molecule with internal structure subject to various evolving fields (e.g. magnetic fields, electric fields, and their gradients).

Energy level shifts from time-varying off-resonant perturbations go by many names, such as Bloch-Siegert shifts, AC Stark shifts and light shifts. These are mostly treated in the literature as separate phenomena from geometric phases. However, the idea that both of these involve the same physics is implicit in some recent work [RKGL88, PHS$^+$04, LG05, Mey10] and originates in an analysis by Ramsey [Ram55]. While most of these treatments analyze the simple case of a spin-1/2 particle in a time-dependent magnetic field, the link between geometric phases and off-resonant energy level shifts is in fact quite general. Here, this connection is explored by looking at some instructive examples, showing with simple calculations how energy level shifts lead to geometric phases in each case. Using this approach correction terms to the (adiabatic) geometric phase, due to the finite rate of evolution of the perturbation, can be obtained easily.

In the following section the basic approach is introduced with the classic example of a spin-1/2 system subject to a magnetic field whose direction changes in time. Then in Section B.2 modifications to the usual geometric phase, when there are multiple Fourier components in the time evolution of the magnetic field, are worked out. Sections B.5 and B.6 show how the geometric phase can arise in a system acted

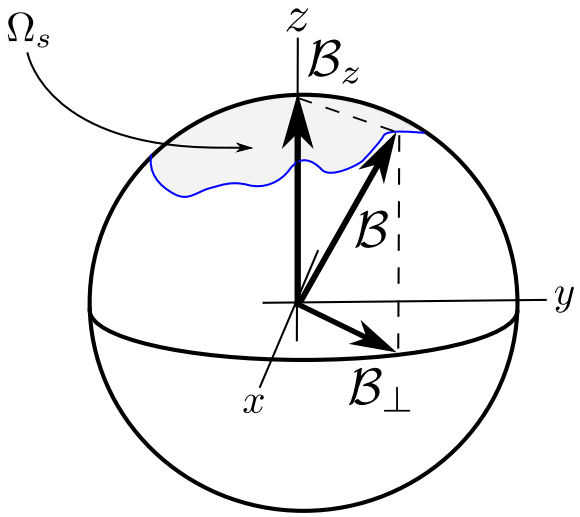

Figure B.1: An example of a trajectory traced by the magnetic field, showing how it can be decomposed into its components along a fixed set of axes: $\vec{\mathcal{B}} = \mathcal{B}_z\hat{z} + \vec{\mathcal{B}}_\perp(t)$. The geometric phase ϕ_g picked up between the sublevels of a spin-1/2 system interacting with this field is equal to the solid angle Ω_s enclosed by the trajectory.

upon by electric fields or a combination of electric and magnetic fields. These sections also indicate how geometric phases can be calculated in a system with a non-trivial level structure, such as an atom or molecule. This is followed in Section B.7 by examples showing how the energy shift formulation allows the calculation of these phase shifts in the non-perturbative regime. The last section applies the method to the problem that motivated this investigation: Ω-doublets in a polar molecule.

Brief recap of perturbation theory

Consider a pair of states $|g\rangle$ and $|e\rangle$, which are governed by a Hamiltonian $H = H_0 + \lambda H_{int}$ (λH_{int} is the interaction Hamiltonian). Assume that $H_0 = \begin{pmatrix} 0 & 0 \\ 0 & \Delta_{eg} \end{pmatrix}$. In analogy with Rayleigh-Schrodinger perturbation theory, we write $E = E_0 + \lambda E_1 + \lambda^2 E_2 + \mathcal{O}(\lambda^3)$ and $|\psi\rangle = |\psi_0\rangle + \lambda|\psi_1\rangle + \mathcal{O}(\lambda^2)$ for the energy and wavefunction of a state. The state $|g\rangle$ is perturbed by the interaction into $|\tilde{g}\rangle$, given by the usual expression from time-dependent perturbation theory

$$|\tilde{g}\rangle = |g\rangle + \frac{1}{i\hbar}\int_{-\infty}^{t} |e\rangle\langle e|\lambda H_{int}|g\rangle \; dt. \tag{B.1}$$

Assuming that the Hamiltonian contains no time-dependent terms resonant with the energy difference between $|g\rangle$ and $|e\rangle$, there is no population transfer and the sole effect of H_{int} is to shift the energies of the states. Further if $\langle g|\lambda H_{int}|g\rangle = 0$, then to leading order in λ, the energy shift of the state $|g\rangle$ is given by the expressions from Rayleigh-Schrodinger perturbation theory:

$$\begin{aligned}\Delta E_g &= \lambda^2 E_2 = \langle g|\lambda H_{int}|\tilde{g}\rangle \\ &= \langle g|\lambda H_{int}|e\rangle \times \int_{-\infty}^{t} \langle e|\lambda H_{int}|g\rangle \; dt/i\hbar \; + \; \mathcal{O}(\lambda^3 H_{int}^3 t^2). \end{aligned} \tag{B.2}$$

λ is a small parameter that is useful for deriving the perturbation series, but it can be set equal to 1 without loss of generality after the perturbation series has been obtained. If $H_{int} = F \; e^{-i\omega_\perp t} + F^\dagger e^{+i\omega_\perp t}$, then

$$\Delta E_g = \frac{|\langle e|F|g\rangle|^2}{-\Delta_{eg} + \omega_\perp} + \frac{|\langle e|F^\dagger|g\rangle|^2}{-\Delta_{eg} - \omega_\perp} + \; \mathcal{O}(F^3). \tag{B.3}$$

This expression is used at a number of places in the following sections, in order to obtain the energy shift in perturbative calculations.

B.1 Spin-1/2 system in a magnetic field

A spin S system in a magnetic field is a well-studied example of the geometric phase [BD87, RKGL88, Com91, Hol89]. When the tip of the magnetic field vector slowly traces out a closed loop in space, the sublevels $|m_S\rangle$ of the system pick up an extra "geometric" phase $\phi_g(m_S) = m_S \times \Omega_s$ (in addition to the usual dynamical phase from Larmor precession) [Ber84, Hol89, Gri05, BKD08]. Here Ω_s is the solid angle enclosed by the loop. In all the subsequent sections, without any loss of generality we focus on the observable quantity defined by the phase *difference* between the $|m_S = \pm S\rangle$ sublevels: $\Delta\phi_g = \phi(m_S = +S) - \phi(m_S = -S)$. In this section a spin S = 1/2 system in a magnetic field is examined and it is shown how the geometric phase shift can be traced back to an off-resonant energy level shift, in this case an AC Zeeman (or Ramsey-Bloch-Siegert) shift.

A fixed coordinate system is used and the changing magnetic field is resolved into a static longitudinal ($\hat{z}$-directed) component and a dynamic transverse component (in the xy plane), as shown in Figure B.1. Let the evolution of the transverse component's direction be composed of a rotation about the z-axis at a single angular

frequency $\omega_\perp$ ($\omega_\perp > 0$ denotes counter-clockwise rotations). The magnetic field written in terms of its components in the fixed coordinate system is

$$\vec{\mathcal{B}} \;=\; \mathcal{B}_z\hat{z} + \vec{\mathcal{B}}_\perp(t) \tag{B.4}$$

where the rotating transverse component of the magnetic field is

$$\vec{\mathcal{B}}_\perp(t) \;=\; \mathcal{B}_\perp(\hat{x}\ \cos\omega_\perp t + \hat{y}\ \sin\omega_\perp t). \tag{B.5}$$

For this discussion we consider small values of $\mathcal{B}_\perp/\mathcal{B}_z$, such that the solid angle enclosed by this loop is $\Omega_s \approx \pi\frac{\mathcal{B}_\perp^2}{\mathcal{B}_z^2}$.

The Hamiltonian of the particle in this magnetic field is

$$H_{int} \;=\; -\gamma\vec{S}\cdot\vec{\mathcal{B}} = -\gamma S_z\mathcal{B}_z - \frac{\gamma\mathcal{B}_\perp}{2}\Big(\ S_- e^{-i\omega_\perp t} + S_+ e^{i\omega_\perp t}\ \Big) \tag{B.6}$$

where γ is the gyromagnetic ratio and $S_\pm = S_x \pm iS_y$ are the spin raising and lowering operators respectively. In the presence of only the longitudinal field $\mathcal{B}_z\hat{z}$, the eigenstates $|m_S = \pm 1/2\rangle$ have energies $E_{m_S} = \langle m_S| - \gamma S_z\mathcal{B}_z|m_S\rangle = -\gamma\mathcal{B}_z m_S$ and the energy shift is $\hbar\omega_0 = (E_{-1/2} - E_{+1/2}) = \gamma\mathcal{B}_z$. We will consider the effect of the time-varying transverse field as a perturbation on the S_z eigenstates. To lowest order, the energy shifts $\Delta E_{\pm 1/2}$ of the $|\pm 1/2\rangle$ states are given by (B.2). Figure B.2 shows the energy levels and the operators connecting them. We define the transverse matrix elements of the spin operator to simplify notation

$$s_\perp^2 = |\langle +1/2|S_+|-1/2\rangle|^2 = |\langle -1/2|S_-|+1/2\rangle|^2 = 1. \tag{B.7}$$

Taking note of the usual selection rules on the matrix elements of the $S_\pm$ operators, we get

$$\begin{aligned}\Delta E_{+1/2} &= \frac{1}{4}\Big[\frac{\gamma^2 s_\perp^2\mathcal{B}_\perp^2}{-\hbar\omega_0 + \hbar\omega_\perp}\Big] \\ &= -\frac{1}{4}\Big[\frac{\gamma\mathcal{B}_\perp^2}{\mathcal{B}_z} + \frac{\mathcal{B}_\perp^2}{\mathcal{B}_z^2}\hbar\omega_\perp + \mathcal{O}(\omega_\perp^2)\Big]\end{aligned} \tag{B.8}$$

$$\begin{aligned}\Delta E_{-1/2} &= \frac{1}{4}\Big[\frac{\gamma^2 s_\perp^2\mathcal{B}_\perp^2}{\hbar\omega_0 - \hbar\omega_\perp}\Big] \\ &= \frac{1}{4}\Big[\frac{\gamma\mathcal{B}_\perp^2}{\mathcal{B}_z} + \frac{\mathcal{B}_\perp^2}{\mathcal{B}_z^2}\hbar\omega_\perp + \mathcal{O}(\omega_\perp^2)\Big].\end{aligned} \tag{B.9}$$

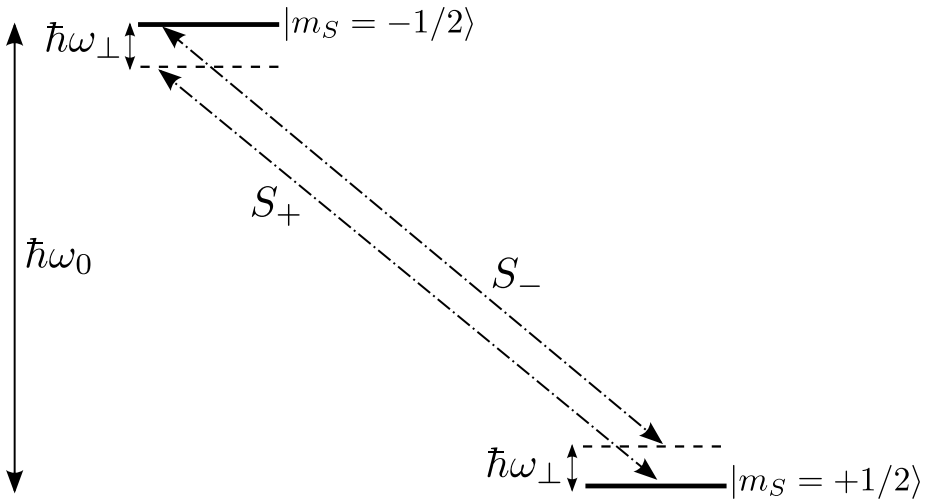

Figure B.2: Energy levels of a spin $S = 1/2$ system interacting with a magnetic field whose direction evolves over time. The level splitting in the longitudinal field is $\hbar\omega_0 = \gamma\mathcal{B}_z$. The dashed lines indicate virtual levels, offset from the real levels by the finite rotation frequency of the transverse field $\vec{\mathcal{B}}_\perp$. $S_\pm$ is the spin raising (lowering) operator which couples the $|m_S = \pm 1/2\rangle$ state to the [virtual] $|m_S = \mp 1/2\rangle$ state in the presence of $\vec{\mathcal{B}}_\perp$.

Note that the condition for applicability of this approximation *viz.* $\omega_\perp \ll \omega_0$ is the same as the adiabatic criterion invoked in the standard approach to describing the geometric phase [Gri05].[2]

The extra energy difference ΔE between $|\pm 1/2\rangle$ due to the transverse rotating component of the field is therefore

$$\begin{aligned} \Delta E &= \Delta E_{+1/2} - \Delta E_{-1/2} \\ &= \{-\gamma\frac{\mathcal{B}_\perp^2}{2\mathcal{B}_z}\} + [-\frac{1}{2}\frac{\mathcal{B}_\perp^2}{\mathcal{B}_z^2}\hbar\omega_\perp] = \Delta E_{QZ} + \Delta E_g, \end{aligned} \tag{B.10}$$

where ΔE_{QZ} (ΔE_g) corresponds to the term in curly (square) brackets. Note that the term ΔE_{QZ} is nonzero even when the field's direction evolves infinitesimally slowly. This term is nothing other than the correction to the Zeeman splitting because the total magnetic field becomes larger on application of the transverse field component: here $\mathcal{B} = \sqrt{\mathcal{B}_z^2 + \mathcal{B}_\perp^2} \approx \mathcal{B}_z + \frac{\mathcal{B}_\perp^2}{2\mathcal{B}_z}$. The term ΔE_g is responsible for the geometric phase. This term, which vanishes when $\omega_\perp \to 0$, nevertheless adds a relative phase

[2]Note that the definition of the term 'adiabatic' in quantum mechanics is distinct from its meaning in thermodynamics. In thermodynamics, an adiabatic process is specifically one where no heat is exchanged between a closed system and the rest of the universe. In quantum mechanics, 'adiabatic' is defined by the conditions of the adiabatic theorem.

between $|\pm 1/2\rangle$ even in this limit. The relative phase picked up over a time interval T is

$$\Delta\phi_g = -\Delta E_g T/\hbar = \frac{1}{2}\frac{\mathcal{B}_\perp^2}{\mathcal{B}_z^2}\omega_\perp T. \tag{B.11}$$

Over one full cycle of the field's evolution, $T = 2\pi/\omega_\perp$ and we get the standard geometric phase result $\Delta\phi_g = \pi\frac{\mathcal{B}_\perp^2}{\mathcal{B}_z^2} \simeq \Omega_s$. The restriction to small solid angles here is equivalent to truncating the perturbation series at second order in $\mathcal{B}_\perp$. Results in the case of larger solid angles can be analytically written down using higher orders of perturbation theory, or alternatively using a dressed-state formalism that is valid for arbitrarily large solid angle [Mey10, CTGDR92]. However the essential point remains that energy level shifts can be calculated *algebraically* (by numerically diagonalizing the Hamiltonian if necessary), without any reference to trajectories in parameter space.

This formulation can be easily extended to situations that are more complicated than the simple loop, as shown in the next section. Moreover, by keeping terms of higher order in $\omega_\perp$, corrections due to deviations from the adiabatic evolution assumption ($\omega_\perp \ll \omega_0$) can be calculated. The energy shift formalism eliminates the need to track the instantaneous basis states of the system throughout its evolution.

B.2 Spin-1/2 system with multiple evolution frequencies

Having illustrated the basic formalism, it can now be applied to a case where the field's direction traces out an arbitrary periodic path. This demonstrates the approach to be used in a general situation, *e.g.* in a precision atomic beam experiment where the fields experienced by an atom along its trajectory can be quite complicated and contain a number of Fourier components. This method will be illustrated with the simple example of a spin-1/2 system in a magnetic field as in the previous section.

An arbitrary periodic transverse magnetic field can be described in terms of harmonics $n\omega_\perp$ ($n = 1, 2, 3\ldots$) of its fundamental evolution frequency $\omega_\perp$.

$$\vec{\mathcal{B}}_\perp(t) = \sum_{n=0}^{\infty} \mathcal{B}_{x,n}\cos(n\omega_\perp t + \phi_{x,n})\ \hat{x}\ +\ \sum_{n=0}^{\infty} \mathcal{B}_{y,n}\cos(n\omega_\perp t + \phi_{y,n})\ \hat{y} \tag{B.12}$$

For a spin $S = 1/2$ system, the geometric phase difference is $\Delta\phi_g = \Omega_s$ [Gri05]. We will evaluate the solid angle Ω_s enclosed by the tip of the magnetic field vector defined by Equation (B.12). The solid angle enclosed by a curve $\theta(\phi)$ on a sphere is given by

$$\Omega_s = \int (1 - \cos\theta)\ d\phi \tag{B.13}$$

where θ, ϕ are the usual spherical polar angles. We use the following definitions

$$\mathcal{B} = \sqrt{\mathcal{B}_z^2 + \mathcal{B}_\perp^2},\ \mathcal{B}_z = \mathcal{B}\cos\theta \tag{B.14}$$

and find that the solid angle is

$$\Omega_s \ = \ \int \frac{1}{2}\frac{\mathcal{B}_\perp^2}{\mathcal{B}_z^2}\ d\phi \ + \mathcal{O}\Big(\frac{\mathcal{B}_\perp^4}{\mathcal{B}_z^4}\Big) \approx \frac{\mathcal{A}}{\mathcal{B}_z^2} \tag{B.15}$$

where $\mathcal{A} = \int \frac{1}{2}\mathcal{B}_\perp^2\ d\phi$ is the area enclosed by the transverse field $\vec{\mathcal{B}}_\perp(t)$ in the xy-plane. For the purpose of comparison with second order perturbation theory the approximation above, where we retain terms up to second order in $\mathcal{B}_\perp$, is sufficiently accurate.

We can express the area $\mathcal{A}$ in terms of $\vec{\mathcal{B}}_\perp(t), \frac{d\vec{\mathcal{B}}_\perp}{dt}$ and evaluate it for the curve defined in Equation (B.12):

$$\begin{aligned}
\mathcal{A} \ &= \ \int \frac{1}{2}\mathcal{B}_\perp^2\ d\phi = \int_0^T \frac{1}{2}\left[\vec{\mathcal{B}}_\perp(t) \times \frac{d\vec{\mathcal{B}}_\perp}{dt}\right] \cdot \hat{z}\ dt \\
&= \ \frac{1}{2}\sum_{m,n=0}^{\infty}\int_0^T dt\ (-n\omega_\perp)\Big[\mathcal{B}_{x,m}\mathcal{B}_{y,n}\cos(m\omega_\perp t + \phi_{x,m})\sin(n\omega_\perp t + \phi_{y,n}) \\
&\qquad\qquad - \mathcal{B}_{y,m}\mathcal{B}_{x,n}\cos(m\omega_\perp t + \phi_{y,m})\sin(n\omega_\perp t + \phi_{x,n})\Big]
\end{aligned} \tag{B.16}$$

To evaluate the geometric phase for a closed path, we integrate this expression over a time $T = 2\pi/\omega$ and find

$$\begin{aligned}
\Omega_s \ &= \ \frac{1}{2\mathcal{B}_z^2}\sum_{n=0}^{\infty}\int_0^T dt\ (-n\omega_\perp)\ 2\mathcal{B}_{x,n}\mathcal{B}_{y,n}\Big[\cos^2(n\omega_\perp t)\cos\phi_{x,n}\sin\phi_{y,n} \\
&\qquad\qquad - \sin^2(n\omega_\perp t)\sin\phi_{x,n}\cos\phi_{y,n}\Big] \\
&= \ \frac{\pi}{\mathcal{B}_z^2}\sum_{n=0}^{\infty} n\ \mathcal{B}_{x,n}\mathcal{B}_{y,n}\sin(\phi_{x,n} - \phi_{y,n}).
\end{aligned} \tag{B.17}$$

Now we shall calculate the geometric phase independently using the energy-shift formalism. First we rewrite the transverse magnetic field in terms of the handed basis that is relevant for calculating the matrix elements of the Hamiltonian. In terms of the handed (spherical) basis vectors $\hat{r}_{\pm 1} = -\frac{\hat{x} \mp i\hat{y}}{\sqrt{2}}$ the transverse field can be written as

$$\begin{aligned}\vec{\mathcal{B}}_\perp(t) &= \sum_{n=0}^{\infty} \frac{\mathcal{B}_{R,n}\ e^{-in\omega_\perp t}\ \hat{r}_{+1} - \mathcal{B}^\dagger_{R,n}\ e^{+in\omega_\perp t}\ \hat{r}_{-1}}{\sqrt{2}} \\ &\quad + \sum_{n=0}^{\infty} \frac{\mathcal{B}_{L,n}\ e^{-in\omega_\perp t}\ \hat{r}_{-1} - \mathcal{B}^\dagger_{L,n}\ e^{+in\omega_\perp t}\ \hat{r}_{+1}}{\sqrt{2}}. \end{aligned} \tag{B.18}$$

The relation between the coefficients in the two bases is

$$\mathcal{B}_{R,n} = \frac{-\mathcal{B}_{x,n}e^{-i\phi_{x,n}} + i\mathcal{B}_{y,n}e^{-i\phi_{y,n}}}{2}, \mathcal{B}_{L,n} = \frac{\mathcal{B}_{x,n}e^{-i\phi_{x,n}} + i\mathcal{B}_{y,n}e^{-i\phi_{y,n}}}{2} \tag{B.19}$$

The extra energy difference between the ground and excited states due to the transverse field is

$$\begin{aligned}\Delta E &= \Delta E_{+1/2} - \Delta E_{-1/2} \\ &= \sum_{m,n=0}^{\infty} -\Big\{ \frac{\gamma}{4\mathcal{B}_z}\Big(e^{i(m-n)\omega_\perp t}(\mathcal{B}^\dagger_{L,m}\mathcal{B}_{L,n} + \mathcal{B}^\dagger_{R,m}\mathcal{B}_{R,n}) \\ &\qquad + e^{-i(m+n)\omega_\perp t}(\mathcal{B}_{R,m}\mathcal{B}_{L,n} + \mathcal{B}_{L,m}\mathcal{B}_{R,n})\Big) + c.c.\Big\} \\ &\quad + \sum_{m,n=0}^{\infty} \Big[\frac{n\hbar\omega_\perp}{2\mathcal{B}_z^2}\Big(e^{i(m-n)\omega_\perp t}(\mathcal{B}^\dagger_{L,m}\mathcal{B}_{L,n} - \mathcal{B}^\dagger_{R,m}\mathcal{B}_{R,n}) \\ &\qquad + e^{-i(m+n)\omega t}(\mathcal{B}_{R,m}\mathcal{B}_{L,n} - \mathcal{B}_{L,m}\mathcal{B}_{R,n})\Big) + c.c.\Big] \\ &= \{\Delta E_{QZ}\} + [\Delta E_g]. \end{aligned} \tag{B.20}$$

As before ΔE_{QZ} corresponds to the quadratic Zeeman shift. ΔE_g is the term linear in $n\omega_\perp$ and leads to the geometric phase. We have retained only terms up to first order in $\omega_\perp$ in order to make a connection with the $\omega_\perp \to 0$ limit in which the geometric method is defined, but we emphasize that phase shifts due to these finite-speed correction terms can be easily calculated by the energy shift method. Note that we have retained all the time-dependent terms appearing in the perturbative calculation of the energy shift. These terms are usually ignored in the expression for the energy shift since they average out to zero, but they can lead to measurable

physical consequences such as in this case.

Over a time duration T the geometric phase accumulated between $|m_S = \pm 1\rangle$ due to the energy shift is

$$\begin{aligned}\Delta\phi_g &= -\frac{1}{2\mathcal{B}_z^2}\sum_{m,n=0}^{\infty}\int_0^T dt\,\Big[\frac{(\mathcal{B}_{L,m}^{\dagger}\mathcal{B}_{L,n} - \mathcal{B}_{R,m}^{\dagger}\mathcal{B}_{R,n})\; e^{i(m-n)\omega_\perp t} + c.c.}{2} \\ &\qquad - \frac{(\mathcal{B}_{R,m}\mathcal{B}_{L,n} - \mathcal{B}_{L,m}\mathcal{B}_{R,n})\; e^{-i(m+n)\omega_\perp t} + c.c.}{2}\Big] \times n\omega_\perp \qquad \text{(B.21)}\end{aligned}$$

With the following quantities defined for ease of notation

$$\begin{aligned}\mathcal{B}_{m,n;A}^2 &= \mathrm{abs}(\mathcal{B}_{L,m}^{\dagger}\mathcal{B}_{L,n} - \mathcal{B}_{R,m}^{\dagger}\mathcal{B}_{R,n}) \\ \mathcal{B}_{m,n;B}^2 &= \mathrm{abs}(\mathcal{B}_{R,m}\mathcal{B}_{L,n} - \mathcal{B}_{L,m}\mathcal{B}_{R,n}) \\ \Phi_{m,n} &= \mathrm{Arg}(\mathcal{B}_{L,m}^{\dagger}\mathcal{B}_{L,n} - \mathcal{B}_{R,m}^{\dagger}\mathcal{B}_{R,n}) \\ \Psi_{m,n} &= \mathrm{Arg}(\mathcal{B}_{R,m}\mathcal{B}_{L,n} - \mathcal{B}_{L,m}\mathcal{B}_{R,n}) \qquad \text{(B.22)}\end{aligned}$$

the geometric phase simplifies to

$$\begin{aligned}\Delta\phi_g &= -\frac{1}{2\mathcal{B}_z^2}\sum_{m,n=0}^{\infty}\Big\{\mathcal{B}_{m,n;A}^2\frac{\sin[(m-n)\omega_\perp T + \Phi_{m,n}] - \sin[\Phi_{m,n}]}{(m-n)\omega_\perp} \\ &\qquad + \mathcal{B}_{m,n;B}^2\frac{\sin[(m+n)\omega_\perp T + \Psi_{m,n}] - \sin[\Psi_{m,n}]}{(m+n)\omega_\perp}\Big\} \times n\omega_\perp. \qquad \text{(B.23)}\end{aligned}$$

This is the full, general expression for the geometric phase acquired by the sublevels of a spin-1/2 particle in an arbitrary periodic transverse magnetic field.

For the special case of a closed loop ($T = 2\pi/\omega_\perp$), the above equation simplifies to

$$\begin{aligned}\Delta\phi_g &= -\frac{\pi}{\mathcal{B}_z^2}\sum_{n=0}^{\infty} n\;\mathcal{B}_{n,n;A}^2\cos\Phi_{n,n} \\ &= \frac{\pi}{\mathcal{B}_z^2}\sum_{n=0}^{\infty} n\;(\mathcal{B}_{R,n}^{\dagger}\mathcal{B}_{R,n} - \mathcal{B}_{L,n}^{\dagger}\mathcal{B}_{L,n}) \\ &= \frac{\pi}{\mathcal{B}_z^2}\sum_{n=0}^{\infty} n\;\mathcal{B}_{x,n}\mathcal{B}_{y,n}\sin(\phi_{x,n} - \phi_{y,n}) \qquad \text{(B.24)}\end{aligned}$$

and is identical to (B.17) which was derived using the geometric formalism. Note that the geometric phase shift is maximal when $\phi_{x,n} - \phi_{y,n} = (2s+1)\pi/2$ *i.e.* when

the fields are maximally handed. We also note that, due to the weighting by a factor of n in the sum, high harmonics $n\omega_\perp$ contained in the periodic evolution can have significant effects even if their amplitudes $\mathcal{B}_{x,n}, \mathcal{B}_{y,n}$ are small. This fact might be relevant for some precision experiments.

B.3 Hyperfine states of hydrogen

We can now calculate the geometric phase for a more realistic physical system. We consider the ground hyperfine states of hydrogen [Gri05]. The Hamiltonian of the system in a $\mathcal{B}$-field is

$$\begin{aligned} H &= A\vec{S}\cdot\vec{I} - (\gamma_S\vec{S} + \gamma_I\vec{I})\cdot\vec{\mathcal{B}} \\ &= A\vec{S}\cdot\vec{I} - (\gamma_S S_z + \gamma_I I_z)\mathcal{B}_z - \frac{\mathcal{B}_\perp}{2}\Big(\gamma_S S_- e^{-i\omega_\perp t} + \gamma_I I_- e^{-i\omega_\perp t} + c.c.\Big) \\ &= H_0 + H_\perp e^{-i\omega_\perp t} + c.c. \end{aligned} \tag{B.25}$$

The field-free eigenstates of the system are $|F, m_F\rangle$. The following matrix elements are useful.

$$\begin{aligned} P_{0,0} &= \langle 0,0|\gamma_S S_z + \gamma_I I_z|1,0\rangle = \frac{\gamma_S - \gamma_I}{2} \\ P_{1,1} &= \langle 1,1|\gamma_S S_z + \gamma_I I_z|1,0\rangle = \frac{\gamma_S + \gamma_I}{2} \\ N_{0,\pm1} &= \langle 0,0|\gamma_S S_- + \gamma_I I_-|1,\pm1\rangle = \mp\frac{\gamma_S - \gamma_I}{\sqrt{2}} \\ N_{1,\pm1} &= \langle 1,0|\gamma_S S_- + \gamma_I I_-|1,\pm1\rangle = \frac{\gamma_S + \gamma_I}{\sqrt{2}} \end{aligned} \tag{B.26}$$

In the presence of $\mathcal{B}_z$ the states $|0,0\rangle$ and $|1,0\rangle$ mix to become

$$\begin{aligned} |\widetilde{1,0}\rangle &= |1,0\rangle\cos\xi/2 + |0,0\rangle\sin\xi/2 \\ |\widetilde{0,0}\rangle &= |0,0\rangle\cos\xi/2 - |1,0\rangle\sin\xi/2 \end{aligned} \tag{B.27}$$

where we denote the field-mixed eigenstates with tildes, and the mixing angle is $\tan\xi = \frac{P_{0,0}\mathcal{B}_z}{A/2}$. We define the following energy denominators and matrix elements for

ease of notation

$$\begin{aligned}
\Delta_0 &= E_{|1,\pm1\rangle} - E_{|\widetilde{0,0}\rangle} = \frac{A}{2} + \sqrt{A^2/4 + (P_{0,0}B_z)^2} \\
\Delta_1 &= E_{|1,\pm1\rangle} - E_{|\widetilde{1,0}\rangle} = \frac{A}{2} + \sqrt{A^2/4 + (P_{0,0}B_z)^2} \\
M_{0,\pm1} &= \cos\xi/2\ N_{0,\pm1} - \sin\xi/2\ N_{1,\pm1} \\
M_{1,\pm1} &= \cos\xi/2\ N_{1,\pm1} + \sin\xi/2\ N_{0,\pm1}
\end{aligned} \tag{B.28}$$

Note that as defined, Δ_0 (Δ_1) is positive (negative). The energy shifts $\Delta E_{\pm1}$ for the $|1,\pm1\rangle$ states due to the transverse field $\mathcal{B}_\perp$ are given by

$$\Delta E_{\pm1} = \frac{\mathcal{B}_\perp}{4}\Big[\frac{M_{0,\pm1}^2}{\Delta_0 \pm P_{1,1}\mathcal{B}_z \pm \hbar\omega_\perp} + \frac{M_{1,\pm1}^2}{\Delta_1 \pm P_{1,1}\mathcal{B}_z \pm \hbar\omega_\perp}\Big]. \tag{B.29}$$

We consider the difference $\Delta E = \Delta E_{+1} - \Delta E_{-1}$ and as before, extract the 'geometric' term ΔE_g that is linear in $\hbar\omega_\perp$. After some algebra that can be readily done with symbolic algebra software, the result is

$$\Delta E_g = -\frac{\mathcal{B}_\perp^2}{\mathcal{B}_z^2}\ \hbar\omega_\perp \tag{B.30}$$

which yields, over a single cycle of evolution $T = 2\pi/\omega_\perp$, the geometric phase

$$\begin{aligned}
\Delta\phi_g &= -\Delta E_g T/\hbar \\
&= 2\pi\frac{\mathcal{B}_\perp^2}{\mathcal{B}_z^2} = 2\Omega_s.
\end{aligned} \tag{B.31}$$

The phase shift once again has an extremely simple form, in spite of the fact that the system contains a lot of parameters such as the hyperfine coupling constant A, different gyromagnetic ratios $\gamma_{S,I}$ for the electron spin and nuclear degrees of freedom.

B.4 An anisotropic system

Consider a system with spin $J = 1$ which is described by the following Hamiltonian in a magnetic field $\vec{\mathcal{B}}$.

$$\begin{aligned}
H &= -A\ J_z^2 - \gamma\vec{J}\cdot\vec{\mathcal{B}} \\
&= -A\ J_z^2 - \gamma J_z\mathcal{B}_z - \frac{\gamma\mathcal{B}_\perp}{2}(J_- e^{-i\omega_\perp t} + c.c.)
\end{aligned} \tag{B.32}$$

An atom inside a crystal is an example of a system with such an anisotropic Hamiltonian (as is a molecule in an Ω-doublet state polarized by an $\mathcal{E}$-field). We will calculate the response of the states $|m_J = \pm 1\rangle$ of this system to a magnetic field that has a static longitudinal component $\mathcal{B}_z$ and a rotating transverse magnetic field.

Using the same perturbative analysis used to illustrate the previous examples, we calculate the energy shifts $\Delta E_{\pm}1$ of the states $|m_J = \pm 1\rangle$. The energy shifts are

$$\Delta E_{\pm 1} = \frac{\gamma^2 \mathcal{B}_\perp^2/2}{A \pm \gamma \mathcal{B}_z \pm \hbar\omega_\perp} \tag{B.33}$$

Expanding the energy out to first order in $\omega_\perp$, we isolate the "geometric" term E_g that is linear in $\omega_\perp$

$$E_g(\pm 1) \approx \mp \frac{1}{2} \frac{\gamma^2 \mathcal{B}_\perp^2}{(A \pm \gamma \mathcal{B}_z)^2} \hbar\omega_\perp \tag{B.34}$$

Over one cycle of the evolution of the transverse field, $T = 2\pi/\omega_\perp$, this energy shift yields a phase

$$\phi_g(\pm 1) = \pi \frac{\gamma^2 \mathcal{B}_\perp^2}{(A \pm \gamma \mathcal{B}_z)^2} \tag{B.35}$$

for these states. In the limit that $\gamma \mathcal{B}_z \gg A$, $\phi_g(\pm 1) = \pm \Omega_s$.. In the opposite limit $\gamma \mathcal{B}_z \ll A$ though, the phase is $\phi_g(\pm 1) = \pi \frac{\gamma^2 \mathcal{B}_\perp^2}{A^2}$.

B.5 Spin-1 system in an electric field

Using the same formalism as above, the geometric phase can be calculated for a system with more complicated levels such as an atom or a molecule. In this section we will consider the geometric phase for a spin $J = 1$ system in an electric field whose direction changes with time. As the electric field vector traces out a loop, the system picks up a geometric phase $\Delta\phi_g = 2\Omega_s$ between the $|m_J = \pm 1\rangle$ states. We refer the reader to the calculation for this case using the geometric formalism in [BKD08], and calculate the same here using energy shifts.

Let the evolving electric field be written as

$$\begin{aligned}\vec{\mathcal{E}} &= \mathcal{E}_z\hat{z} + \vec{\mathcal{E}}_\perp(t) \\ \vec{\mathcal{E}}_\perp(t) &= \mathcal{E}_\perp(\hat{x}\ \cos\omega_\perp t + \hat{y}\ \sin\omega_\perp t) \\ &= \frac{\mathcal{E}_\perp}{\sqrt{2}}\Big(-\hat{r}_{+1}e^{-i\omega_\perp t} + \hat{r}_{-1}e^{+i\omega_\perp t}\Big). \end{aligned} \tag{B.36}$$

The Hamiltonian of the system in the electric field is

$$H_{int} = -\vec{D}\cdot\vec{\mathcal{E}} = -D_z\mathcal{E}_z - \frac{D_{-1}\mathcal{E}_\perp e^{-i\omega_\perp t} - D_{+1}\mathcal{E}_\perp e^{i\omega_\perp t}}{\sqrt{2}}. \tag{B.37}$$

Here we have defined the electric dipole moment operator $\vec{D}$. This operator only couples states of opposite parity, whereas the $|m_J = 0, \pm 1\rangle$ sublevels of a $J = 1$ level all have the same parity. To calculate the effect of electric fields, it is essential to enlarge the system and include an opposite parity state in addition to the spin-1 sublevels. For simplicity, we consider here the 4-state system consisting of the 3 sublevels of a $J^\pi = 1^-$ level: $|J = 1, m_J = 0\rangle, |J = 1, m_J = \pm 1\rangle$, and in addition a $J^\pi = 0^+$ state: $|J = 0, m_J = 0\rangle$. Here J denotes the angular momentum and π the parity of the state. We refer to states by their $|J, m_J\rangle$ labels from now on. Figure B.3(a) shows these states. We are interested in the phase that is picked up between the $|1, \pm 1\rangle$ states due to the evolving electric field. Choose the zero of energy halfway between $|1, 0\rangle$ and $|0, 0\rangle$, and let the zero-field separation between them be $2B$. The perturbative calculation requires matrix elements of $\vec{D}$, which we write as

$$\begin{aligned} d_z\hat{z} &= \langle 1, 0|\vec{D}|0, 0\rangle \\ -d_{\pm 1}\hat{r}_{\mp 1} &= \langle 1, \pm 1|\vec{D}|0, 0\rangle. \end{aligned} \tag{B.38}$$

Here we have used the Wigner-Eckart theorem to define only the nonzero matrix elements of $\vec{D}$; this can also be used to show that all three of the nonzero matrix elements have a common value: $d_0 \equiv d_z = d_{\pm 1}$.

First, we consider the effect of $\mathcal{E}_z$. This part of $\vec{\mathcal{E}}$ only mixes the two states $|1, 0\rangle$ and $|0, 0\rangle$. Under the interaction with this part of the field, the eigenstates are

$$\begin{aligned} \widetilde{|1, 0\rangle} &= |1, 0\rangle\cos\xi/2 + |0, 0\rangle\sin\xi/2 \\ \widetilde{|0, 0\rangle} &= |0, 0\rangle\cos\xi/2 - |1, 0\rangle\sin\xi/2 \end{aligned} \tag{B.39}$$

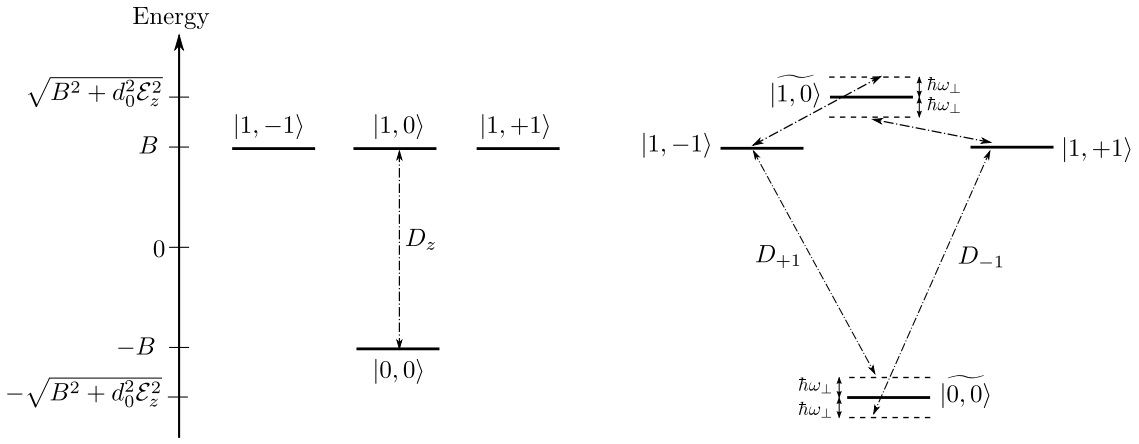

(a) Zero-field eigenstates

(b) Eigenstates under the longitudinal field $\mathcal{E}_z$

Figure B.3: Energy levels of a spin $J = 1$ system in an electric field. States are labelled by their angular momentum quantum numbers J, m_J. Dashed arrows and their labels indicate the states being coupled by the respective components of the dipole moment operator. Under the influence of a longitudinal electric field $\mathcal{E}_z$, the $|0,0\rangle$ and $|1,0\rangle$ states shown in (a) are perturbed into $|\widetilde{0,0}\rangle$ and $|\widetilde{1,0}\rangle$ as shown in (b). The rotating transverse electric field $\vec{\mathcal{E}}_\perp(t)$ induces virtual energy levels (dashed lines) $\hbar\omega_\perp$ above and below the static perturbed states. $\vec{\mathcal{E}}_\perp(t)$ couples these states with the $|1,\pm1\rangle$ states of interest, through the dipole moment operators $D_{\pm1}$.

where we denote the field-mixed eigenstates with tildes, and the mixing angle is $\tan\xi = \frac{d_0\mathcal{E}_z}{B}$ so that

$$\sin^2\xi/2 = \frac{\sqrt{B^2 + d_0^2\mathcal{E}_z^2} - B}{2\sqrt{B^2 + d_0^2\mathcal{E}_z^2}}, \quad \cos^2\xi/2 = \frac{\sqrt{B^2 + d_0^2\mathcal{E}_z^2} + B}{2\sqrt{B^2 + d_0^2\mathcal{E}_z^2}}. \tag{B.40}$$

The $|\widetilde{1,0}\rangle, |\widetilde{0,0}\rangle$ states have energies $\pm\sqrt{B^2 + d_0^2\mathcal{E}_z^2}$ respectively. The $|1,\pm1\rangle$ states remain at their zero-field location $E_{|1,+1\rangle} = E_{|1,-1\rangle} = +B$, as shown in Figure B.3(b). The splitting Δ_1 between the $|1,\pm1\rangle$ and $|\widetilde{1,0}\rangle$ levels is usually referred to in the literature as a *tensor Stark* shift [BKD08].

Next we consider the interaction with the rotating transverse field and calculate the effect to second order in perturbation theory. As indicated in Figure B.3(b) the transverse field only couples $|1,\pm1\rangle$ with $|\widetilde{1,0}\rangle$ or $|\widetilde{0,0}\rangle$. Define the following energy denominators for ease of notation

$$\begin{aligned}
\Delta_0 &= E_{|1,\pm1\rangle} - E_{|\widetilde{0,0}\rangle} = B + \sqrt{B^2 + d_0^2\mathcal{E}_z^2} \\
\Delta_1 &= E_{|1,\pm1\rangle} - E_{|\widetilde{1,0}\rangle} = B - \sqrt{B^2 + d_0^2\mathcal{E}_z^2}.
\end{aligned} \tag{B.41}$$

Note that as defined, Δ_0 (Δ_1) is positive (negative). The energy shifts $\Delta E_{\pm 1}$ for the $|1, \pm 1\rangle$ states due to the transverse electric field $\mathcal{E}_\perp$ are given by

$$\Delta E_{\pm 1} = \frac{1}{2}\Big[\frac{d_0^2 \mathcal{E}_\perp^2 \cos^2 \xi/2}{\Delta_0 \pm \hbar\omega_\perp} + \frac{d_0^2 \mathcal{E}_\perp^2 \sin^2 \xi/2}{\Delta_1 \pm \hbar\omega_\perp}\Big]. \tag{B.42}$$

Where the $|1, \pm 1\rangle$ states were degenerate before, they are now split by the energy $\Delta E = \Delta E_{+1} - \Delta E_{-1}$ given by

$$\Delta E = -\frac{d_0^2 \mathcal{E}_\perp^2 \cos^2 \xi/2}{\Delta_0^2}\hbar\omega_\perp - \frac{d_0^2 \mathcal{E}_\perp^2 \sin^2 \xi/2}{\Delta_1^2}\hbar\omega_\perp + \mathcal{O}(\omega_\perp^2). \tag{B.43}$$

We have again retained only the terms to least order in $\omega_\perp$ to extract the adiabatic part of the phase and make contact with the usual geometric result. Substituting the values of ξ, Δ_0, Δ_1 we get

$$\begin{aligned}
\Delta E &= -d_0^2 \mathcal{E}_\perp^2 \Bigg[\frac{\sqrt{B^2 + d_0^2 \mathcal{E}_z^2} + B}{2\sqrt{B^2 + d_0^2 \mathcal{E}_z^2}} \; \frac{1}{\Big(\sqrt{B^2 + d_0^2 \mathcal{E}_z^2} + B\Big)^2} + \\
&\qquad \frac{\sqrt{B^2 + d_0^2 \mathcal{E}_z^2} - B}{2\sqrt{B^2 + d_0^2 \mathcal{E}_z^2}} \; \frac{1}{\Big(\sqrt{B^2 + d_0^2 \mathcal{E}_z^2} - B\Big)^2} \Bigg] \hbar\omega_\perp \qquad \text{(B.44)} \\
&= -\frac{\mathcal{E}_\perp^2}{\mathcal{E}_z^2}\hbar\omega_\perp = \Delta E_g. \qquad \text{(B.45)}
\end{aligned}$$

Compared to the case with a magnetic field, in a pure electric field the only energy difference between $|1, \pm 1\rangle$ is the geometric contribution ΔE_g. The relative phase between $|1, \pm 1\rangle$ after a time duration corresponding to a single complete cycle of evolution, $T = 2\pi/\omega_\perp$, is

$$\begin{aligned}
\Delta\phi_g &= -\Delta E_g T/\hbar = \frac{\mathcal{E}_\perp^2}{\mathcal{E}_z^2}\omega_\perp T \\
&= 2\pi\frac{\mathcal{E}_\perp^2}{\mathcal{E}_z^2} = 2\Omega_s. \qquad \text{(B.46)}
\end{aligned}$$

This same case is worked out in [BKD08] by restricting the calculation to the $J = 1$ manifold and introducing the tensor Stark shift "by hand" (thereby implicitly including the $J = 0$ state). It is interesting that the explicit introduction of the $J = 0$ state from the start does not affect the result at the end.

B.6 Combined effect of electric and magnetic fields

The formalism developed in the previous section can be easily extended to a more complicated case, where the system interacts with both electric and magnetic fields. The standard geometric approach in this case requires us to calculate all instantaneous eigenvectors of the system, and their gradients with respect to the 6-dimensional parameter space that describes the Hamiltonian and its evolution (3 degrees of freedom each for the electric and magnetic fields). Energy shifts on the other hand can be calculated in a straightforward manner, as we shall see in the following two subsections. In the eEDM experiment with ThO, the molecules are affected by both $\mathcal{E}$ and $\mathcal{B}$-fields during their flight through the interaction region, rather than undergoing an idealized evolution under pure $\mathcal{E}$ or $\mathcal{B}$-fields alone. Therefore a simple way to estimate the size of geometric phases picked up in combined $\mathcal{E}$ and $\mathcal{B}$-fields is useful.

Rotating electric field, static magnetic field

We will first examine the same spin-1 system as in the previous section and understand what happens to it when a static magnetic field $\vec{\mathcal{B}} = \mathcal{B}_z\hat{z}$ is imposed along with the revolving electric field. The interaction Hamiltonian of the system is now

$$\begin{aligned} H_{int} &= -\vec{D}\cdot\vec{\mathcal{E}} - \vec{\mu}\cdot\vec{\mathcal{B}} \\ &= -D_z\mathcal{E}_z - \mu_z\mathcal{B}_z - \frac{D_{-1}\mathcal{E}_\perp e^{-i\omega_\perp t} - D_{+1}\mathcal{E}_\perp e^{i\omega_\perp t}}{\sqrt{2}}. \end{aligned} \tag{B.47}$$

with $\vec{\mu}$ the magnetic moment of the $J = 1$ state.

To illustrate the basic ideas we again use a perturbative approach, to study the influence of the transverse time-dependent components of $\mathcal{E}$ on the eigenstates in the presence of only $\mathcal{E}_z$ and $\mathcal{B}_z$. The eigenstates of the system are shown in Figure B.4. We will carry over the notation and definitions from the previous section.

The essential effect of the $\mathcal{B}_z$ field is in the energy denominators that appear in the AC Stark shift. The energy shifts of the $|1,\pm1\rangle$ states (in addition to their Zeeman shifts in the magnetic field) are given to lowest order in $\mathcal{E}_\perp$ by

$$\Delta E_{\pm1} = \frac{1}{2}\Big[\frac{d_0^2\mathcal{E}_\perp^2\cos^2\xi/2}{\Delta_0 \pm \mu_z\mathcal{B}_z \pm \hbar\omega_\perp} + \frac{d_0^2\mathcal{E}_\perp^2\sin^2\xi/2}{\Delta_1 \pm \mu_z\mathcal{B}_z \pm \hbar\omega_\perp}\Big]. \tag{B.48}$$

To make a connection with the geometric limit, we expand the energy shift ΔE

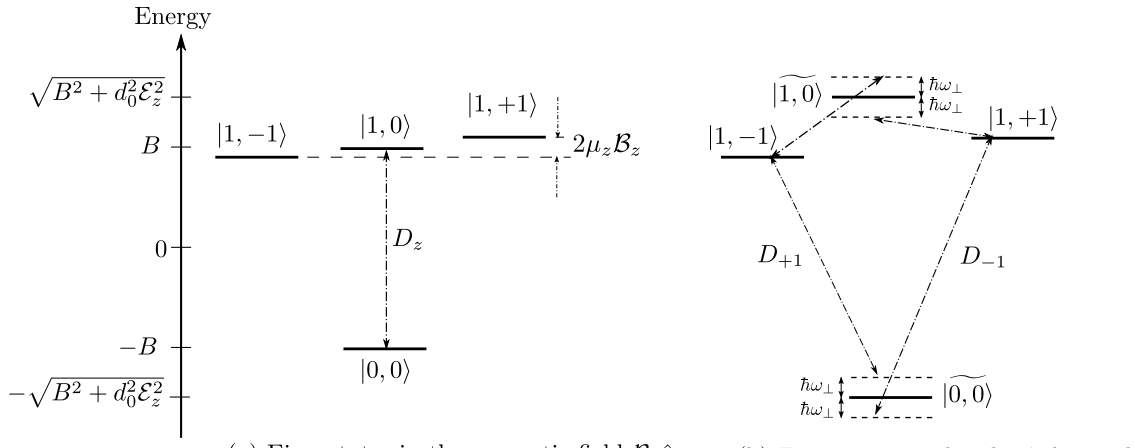

(a) Eigenstates in the magnetic field $\mathcal{B}_z\hat{z}$

(b) Eigenstates under the $\hat{z}$-directed static $\mathcal{E}$- and $\mathcal{B}$-fields

Figure B.4: Energy levels of a spin $J = 1$ system in a combination of electric and magnetic fields. The state labels and symbols are the same as in Figure B.3. In (b), the figure as shown corresponds to a case where the Zeeman shift is somewhat smaller than the tensor Stark shift: $\mu_z\mathcal{B}_z \lesssim \Delta_1$.

between $|1,\pm1\rangle$ up to first order in $\hbar\omega_\perp$, and write

$$\Delta E = \Delta E_{+1} - \Delta E_{-1} \approx \mathcal{C} + \mathcal{D}\ \hbar\omega_\perp. \tag{B.49}$$

We interpret $\mathcal{C}$ as the analog of a (static) quadratic Zeeman/Stark shift due to the inclusion of $\mathcal{E}_\perp$, and $\Delta E_g = \mathcal{D}\ \hbar\omega_\perp$ as the energy shift that leads to a geometric phase difference $\Delta\phi_g = -\mathcal{D}\omega_\perp T$. Table B.1 shows the values of the geometric phase $\Delta\phi_g$ in some limiting cases, corresponding to regimes where one of the various energy scales in the problem is dominant. The relevant energy scales are the Zeeman shift $\mu_z\mathcal{B}_z$, the Stark matrix element $d_0\mathcal{E}_z$, the Stark shift of the $|1,0\rangle$ state $|\Delta_1|$, and the zero-field energy splitting $2B$ between $J^\pi = 0^+$ and $J^\pi = 1^-$ levels.

The geometric phase in every case can be simply calculated from the energy shift between $|1,\pm1\rangle$. This energy shift can be computed perturbatively, or by numerically diagonalizing the Hamiltonian if necessary. An important feature to note in Table B.1 is that the zero-field energy splitting between $J^\pi = 0^+$ and $J^\pi = 1^-$ levels appears irreducibly in some of the limiting expressions. This shows that the inclusion of the opposite parity (*e.g.* $J^\pi = 0^+$) state is necessary to properly describe geometric phases in a combination of electric and magnetic fields.

Case	Limiting condition	Geometric phase difference, $\Delta\phi_g$
I	$\mu_z\mathcal{B}_z \ll \lvert\Delta_1\rvert, d_0\mathcal{E}_z$	$\left(\frac{\mathcal{E}_\perp}{\mathcal{E}_z}\right)^2\omega_\perp T$
II	$\lvert\Delta_1\rvert \ll \mu_z\mathcal{B}_z \ll d_0\mathcal{E}_z$	$\left(\frac{\mathcal{E}_\perp}{\mathcal{E}_z}\right)^2\left(\frac{\Delta_1}{\mu_z\mathcal{B}_z}\right)^2\omega_\perp T$
III	$d_0\mathcal{E}_z \ll \mu_z\mathcal{B}_z \ll 2B$	$\left(\frac{\mathcal{E}_\perp}{\mathcal{E}_z}\right)^2\left(\frac{d_0\mathcal{E}_z}{2B}\right)^2\omega_\perp T$
IV	$d_0\mathcal{E}_z, 2B \ll \mu_z\mathcal{B}_z$	$\left(\frac{\mathcal{E}_\perp}{\mathcal{E}_z}\right)^2\left(\frac{d_0\mathcal{E}_z}{\mu_z\mathcal{B}_z}\right)^2\omega_\perp T$

Table B.1: Analytical expressions in some limiting conditions, for the geometric phase in a static magnetic field $\mathcal{B}_z$ and electric field $\mathcal{E}_z$, along with a rotating transverse electric field component $\mathcal{E}_\perp$. In each case, the geometric phase between $|1,\pm1\rangle$ up to first order in $\omega_\perp$ is shown.

Rotating magnetic field, static electric field

As another illustration of the energy shift formalism in a case with combined electric and magnetic fields, consider the case where the system experiences a static $\hat{z}$-directed electric field, and a revolving magnetic field $\vec{\mathcal{B}} = \mathcal{B}_z\hat{z} + \mathcal{B}_\perp(\hat{x}\ \cos\omega_\perp t + \hat{y}\ \sin\omega_\perp t)$. The interaction Hamiltonian is

$$\begin{aligned} H_{int} &= -\vec{D}\cdot\vec{\mathcal{E}} - \vec{\mu}\cdot\vec{\mathcal{B}} \\ &= -D_z\mathcal{E}_z - \mu_z\mathcal{B}_z - \frac{\mu_{-1}\mathcal{B}_\perp e^{-i\omega_\perp t} - \mu_{+1}\mathcal{B}_\perp e^{i\omega_\perp t}}{\sqrt{2}}. \end{aligned} \tag{B.50}$$

where the spherical components of the magnetic moment $\vec{\mu}$ are defined as follows.

$$\begin{aligned} \mu_z\hat{z} &= \langle 1,1|\vec{\mu}|1,1\rangle \\ -\mu_{\pm1}\hat{r}_{\mp1} &= \langle 1,\pm1|\vec{\mu}|1,0\rangle. \end{aligned} \tag{B.51}$$

Once again, the Wigner-Eckart theorem has been used to define the non-zero matrix elements (which turn out to be identical): $\mu_0 \equiv \mu_z = \mu_{\pm1}$.

The energy shifts are

$$\Delta E_{\pm 1} = \frac{1}{2}\Big[\frac{\mu_0^2 \mathcal{B}_\perp^2 \sin^2\xi/2}{\Delta_0 \pm \mu_z \mathcal{B}_z \pm \hbar\omega_\perp} + \frac{\mu_0^2 \mathcal{B}_\perp^2 \cos^2\xi/2}{\Delta_1 \pm \mu_z \mathcal{B}_z \pm \hbar\omega_\perp}\Big]. \tag{B.52}$$

As in the previous section, we expand the energy shift ΔE between $|1,\pm 1\rangle$ up to first order in $\hbar\omega_\perp$

$$\Delta E = \Delta E_{+1} - \Delta E_{-1} \approx \mathcal{C} + \mathcal{D}\ \hbar\omega_\perp \tag{B.53}$$

and focus our attention on the relative energy shift $\Delta E_g = \mathcal{D}\ \hbar\omega_\perp$ that leads to a geometric phase $\Delta\phi_g$. The relevant energy scales in the problem are the same as in the previous section. We consider cases where $\Delta_1 \ll 2B$ *i.e.* the system is weakly electrically polarized by the $\mathcal{E}_z$-field. Table B.2 lists the geometric phase in some limiting cases where the analytic expression becomes simple.

As expected, when the Zeeman splitting is sufficiently large (Cases I and II) the geometric phase reduces to the result expected in the pure magnetic field scenario. Case III is interesting and quite relevant to real world experiments. Compared to the situation in a pure magnetic field, the geometric phase in the presence of a strong tensor Stark splitting is significantly suppressed, by a factor $\left(\frac{\mu_z \mathcal{B}_z}{\Delta_1}\right)^2$ which could be $\sim 10^{-6}$ in experiments using polar molecules to search for the electron electric dipole moment [THSH09, LBL+10, BHJD09].

The expressions listed in Table B.2 are special cases derived from the more general Equation (B.52) for the energy shift between $|1,\pm 1\rangle$. *A priori* it is not evident how (B.52) or the limiting cases in Table B.2 can be related to a solid angle in the parameter space of the Hamiltonian. But in terms of energy level shifts, they can be obtained by a simple algebraic calculation.

B.7 Energy shifts in the non-perturbative regime

All of the above examples have used perturbation theory to calculate the energy shift. However, perturbation theory is only a convenient way to calculate energy shifts; it is not essential to the fundamental point that is being made in this Chapter. Energy shifts can be calculated in any way desired, be it exact analytic, perturbative or numerical. The purpose of this section is to show that the energy shift formalism can be used to evaluate the "geometric" phase in all regimes, even when 2nd order

Case	Limiting condition	Geometric phase difference, $\Delta\phi_g$
I	$\lvert\Delta_1\rvert \ll 2B \ll \mu_z\mathcal{B}_z$	$\left(\frac{\mathcal{B}_\perp}{\mathcal{B}_z}\right)^2\omega_\perp T$
II	$\lvert\Delta_1\rvert \ll \mu_z\mathcal{B}_z \ll 2B$	$\left(\frac{\mathcal{B}_\perp}{\mathcal{B}_z}\right)^2\omega_\perp T$
II	$\mu_z\mathcal{B}_z \ll \lvert\Delta_1\rvert \ll 2B$	$\left(\frac{\mu_0\mathcal{B}_\perp}{\Delta_1}\right)^2\omega_\perp T$

Table B.2: Analytical expressions in some limiting conditions, for the geometric phase in a static electric field $\mathcal{E}_z$ with a rotating transverse magnetic field component $\mathcal{B}_\perp$. In each case, the geometric phase between $|1,\pm1\rangle$ up to first order in $\omega_\perp$ is shown.

perturbation theory is insufficient. As usual, in the limit when $\omega_\perp \to 0$, the result of the energy shift calculation gives exactly the standard "geometric" result. This is shown using two non-trivial examples, one analytical and the other numerical.

$J = 1$ in a $\mathcal{B}$-field

Consider a $J = 1$ system with a magnetic moment, in a $\mathcal{B}$-field. Let the field be tipped at an arbitrary angle θ. The time dependence of the magnetic field is the usual

$$\vec{\mathcal{B}} \;=\; \mathcal{B}_z\hat{z} + \vec{\mathcal{B}}_\perp(t) \tag{B.54}$$

where the rotating transverse component of the magnetic field is

$$\vec{\mathcal{B}}_\perp(t) \;=\; \mathcal{B}_\perp(\hat{x}\ \cos\omega_\perp t + \hat{y}\ \sin\omega_\perp t). \tag{B.55}$$

In terms of the tip angle θ, $\mathcal{B}_z = \mathcal{B}\ \cos\theta, \mathcal{B}_\perp = \mathcal{B}\ \sin\theta$. We set up the Hamiltonian matrix (in the basis $|-1\rangle, |0, |+1\rangle$) for a dressed-state calculation [CTGDR92]

$$H = \begin{pmatrix} -\gamma\mathcal{B}\cos\theta - \omega_\perp & \gamma\mathcal{B}\sin\theta/\sqrt{2} & 0 \\ \gamma\mathcal{B}\sin\theta/\sqrt{2} & 0 & \gamma\mathcal{B}\sin\theta/\sqrt{2} \\ 0 & \gamma\mathcal{B}\sin\theta/\sqrt{2} & \gamma\mathcal{B}\cos\theta + \omega_\perp \end{pmatrix} \tag{B.56}$$

and solve it by exact diagonalization instead of perturbation theory. The eigenvalues are easily evaluated by symbolic algebra packages. They are:

$$\lambda(H) = [0, \pm\sqrt{\gamma^2\mathcal{B}^2 + 2\gamma\mathcal{B}\cos\theta\ \omega_\perp + \omega_\perp^2}] \tag{B.57}$$

The 'geometric' contribution is given by the term in the energy shift that is first order in $\omega_\perp$ i.e. $\left.\frac{\partial\lambda}{\partial\omega_\perp}\right|_{\omega_\perp=0} \times \omega_\perp$. Evaluating this, the geometric contribution to the energy shift is

$$\Delta E_g = [0, \mp\cos\theta]\ \omega_\perp \equiv m_J\ \cos\theta\ \omega_\perp \tag{B.58}$$

This is exactly equal to the usual geometric result. One gets a little more information from this procedure, since there are $\mathcal{O}(\omega_\perp^2)$ and higher terms in the Taylor expansion of the real energy shift which are not captured by the geometric formulation.

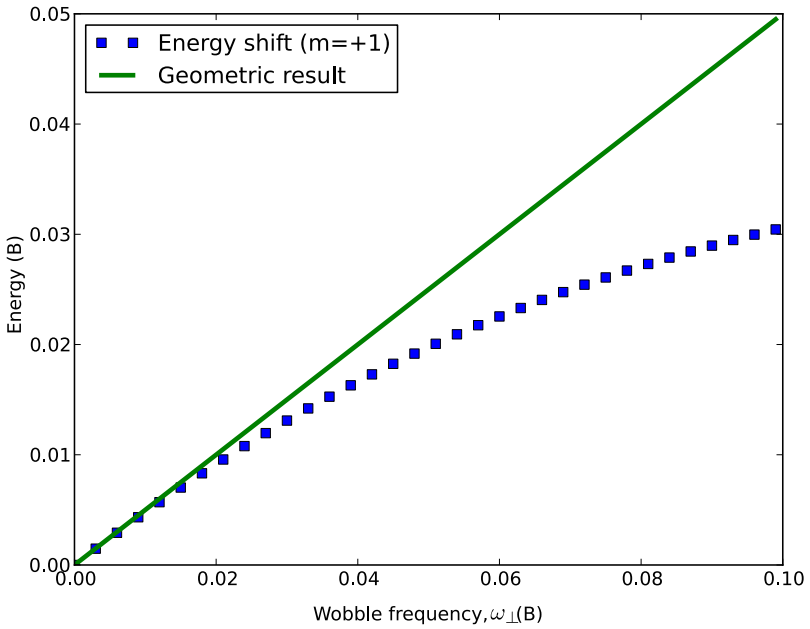

Figure B.5: $J = 1$ system in an $\mathcal{E}$-field. Comparison between the energy shift of the $|J = 1, m_J = 1\rangle$ state and the geometric result ($\Delta E_{+1} = \omega_\perp\ \cos\theta$) as a function of $\omega_\perp$, for a fixed tip angle ($\theta = \pi/3$) and interaction strength $D\mathcal{E} = 0.6\ B$. This is merely an illustration of the fact that the geometric formulation only works in the adiabatic limit.

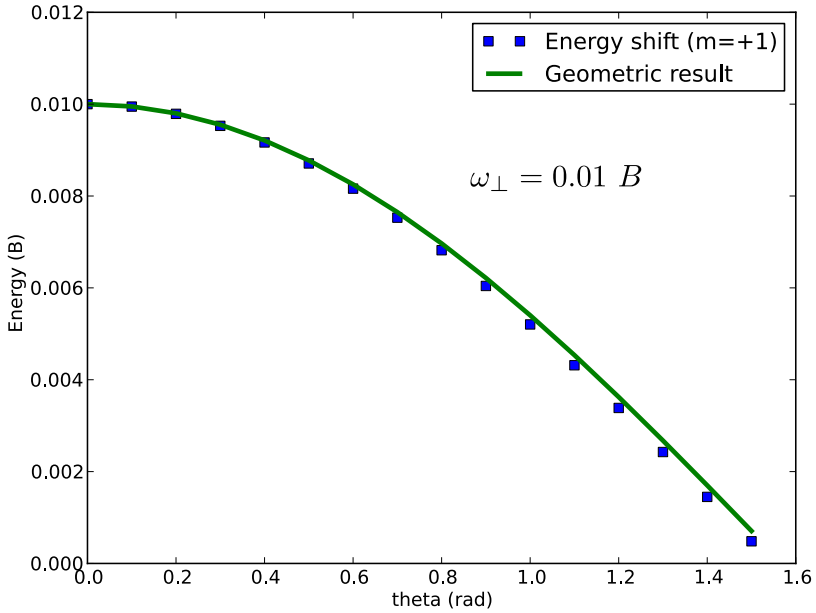

(a) w=0.01

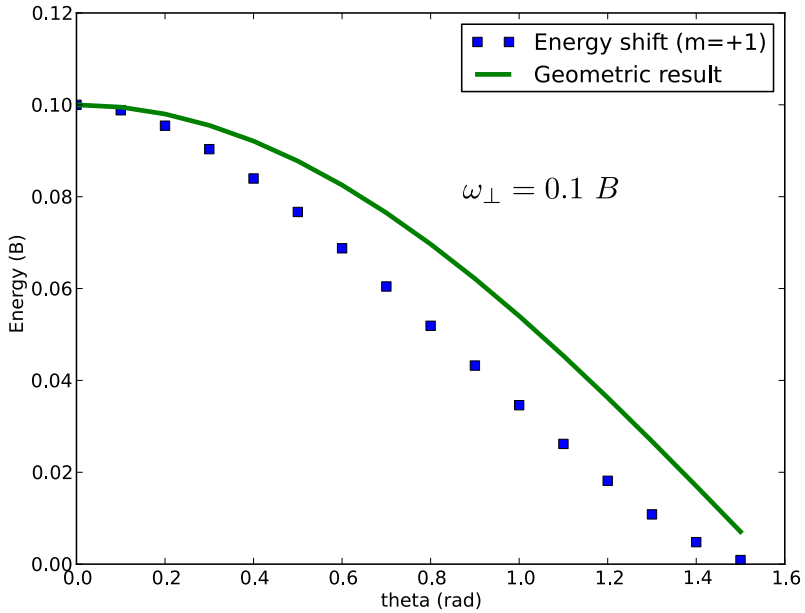

(b) w=0.1

Figure B.6: $J = 1$ system in an $\mathcal{E}$-field. Comparison between exact energy shift of the $|J = 1, m_J = 1\rangle$ state and the geometric result ($\Delta E_{+1} = \omega_\perp \cos\theta$) as a function of tip angle θ, for various values of $\omega_\perp$. The calculations are performed at a fixed interaction strength $D\mathcal{E} = 0.6\ B$.

$J = 1$ in an $\mathcal{E}$-field

Consider the 4-state system formed by a $J = 0$ state and a set of $J = 1$ sublevels. Using the same notation as before, we set up the Hamiltonian matrix used in Section B.5, except that we now allow arbitrary tip angles θ. The assumptions for applying perturbation theory break down in this case, but the basic notion (that energy shifts are really what give rise to the geometric phase) is still valid as we shall see. The Hamiltonian in the basis $|0,0\rangle, |1,0\rangle, |1,+1\rangle, |1,-1\rangle$ is written in the dressed-state basis as

$$H = B \times \begin{pmatrix} -1 & -s\cos\theta & -s\sin\theta/\sqrt{2} & s\sin\theta/\sqrt{2} \\ -s\cos\theta & 1 & 0 & 0 \\ -s\sin\theta/\sqrt{2} & 0 & 1+w & 0 \\ s\sin\theta/\sqrt{2} & 0 & 0 & 1-w \end{pmatrix} \tag{B.59}$$

written in terms of the dimensionless quantities $s = D\mathcal{E}/B, w = \omega_\perp/B$ for the sake of numerical computation. Results from numerical diagonalization of this matrix for various parameters are shown in Figs. B.5 and B.6.

The numerically calculated eigenvalue differences match the geometric result, with the agreement getting better as $\omega_\perp \to 0$ as expected. Note that the calculation only involves a simple evaluation of eigenvalues.

B.8 H state Ω-doublets

The purpose of this section is to evaluate the geometric phase picked up by ThO molecules in the $H, J = 1$ state while traversing the interaction region of the EDM experiment, assuming that there are small apparatus-fixed transverse components $\mathcal{E}_\perp, \mathcal{B}_\perp$ of the $\mathcal{E}$- and $\mathcal{B}$-fields. As the molecules traverse the field, these apparatus-fixed components result in a time-dependent transverse field experienced in the rest frame of the molecules. The geometric phase due to these field components can be evaluated using the same methods as above, even though a $J = 1$ Ω-doublet has a complicated state space consisting of number of interacting sublevels. The algebraic calculation that follows is restricted to a single fourier component (at a frequency $\omega_\perp^E, \omega_\perp^B$ for the $\mathcal{E}_\perp, \mathcal{B}_\perp$ fields respectively) and to 2^{nd} order in perturbation theory for $\mathcal{E}_\perp, \mathcal{B}_\perp$. The geometric phase induced by the transverse fields is evaluated in order to show the following: *geometric phases picked up by the two components*

of an Ω-doublet are equal in magnitude and opposite in sign. Hence, comparing the precession phases picked up in the upper and lower Ω-doublets allows for the rejection of systematic errors due to the geometric phase. This is one more feature that makes Ω-doublets advantageous for EDM experiments; it was first reported in [VCG+10].

The $H, J = 1$ state has a magnetic moment $\vec{\mu}$ and an (induced) electric dipole moment D, which interact with the laboratory $\mathcal{E}$- and $\mathcal{B}$-fields according to the Hamiltonian

$$\begin{aligned} H_{int} &= -\vec{D}\cdot\vec{\mathcal{E}} - \vec{\mu}\cdot\vec{\mathcal{B}} \\ &= -D_z\mathcal{E}_z - \mu_z\mathcal{B}_z - \frac{\mu_{-1}\mathcal{B}_\perp e^{-i\omega_\perp t} - \mu_{+1}\mathcal{B}_\perp e^{i\omega_\perp t}}{\sqrt{2}} \\ &\quad - \frac{D_{-1}\mathcal{E}_\perp e^{-i\omega_\perp t} - D_{+1}\mathcal{E}_\perp e^{i\omega_\perp t}}{\sqrt{2}}. \end{aligned} \tag{B.60}$$

As before, we calculate the effect of $\mathcal{E}_\perp, \mathcal{B}_\perp$ on the energy eigenstates in a static electric $\mathcal{E}_z$ and magnetic $\mathcal{B}_z$ field. Figure B.7 shows the structure of the eigenstates in a combination of $\hat{z}$-directed $\mathcal{E}$- and $\mathcal{B}$-fields, as is the case in the interaction region of the ThO eEDM experiment (see Chapter 2). The quantum number $\mathcal{N} = m_J\Omega$ is defined as in previous chapters. The two states $|m_J = \pm 1, \mathcal{N} = +1\rangle$ (which are lowered in energy in an $\mathcal{E}$-field) pick up a differential energy shift due to $\mathcal{E}_\perp, \mathcal{B}_\perp$, denoted by $\Delta E^+_{\pm 1}$. The two states $|m_J = \pm 1, \mathcal{N} = -1\rangle$ (which go up in energy in an $\mathcal{E}$-field) pick up a differential energy shift due to $\mathcal{E}_\perp, \mathcal{B}_\perp$, denoted by $\Delta E^-_{\pm 1}$. These energy shifts are identical in form for $\mathcal{N} = \pm 1$ states, and given by

$$\begin{aligned} \Delta E^{\mathcal{N}}_{\pm 1} &= \frac{1}{2}\Big[\frac{\mu_\perp^2\mathcal{B}_\perp^2}{\Delta_{st} + \mu_z\mathcal{B}_z - \omega^B_\perp} + \frac{d_\perp^2\mathcal{E}_\perp^2}{\Delta_{st} + \mu_z\mathcal{B}_z - \omega^E_\perp} \\ &\quad - \frac{\mu_\perp^2\mathcal{B}_\perp^2}{\Delta_{st} - \mu_z\mathcal{B}_z + \omega^B_\perp} - \frac{d_\perp^2\mathcal{E}_\perp^2}{\Delta_{st} - \mu_z\mathcal{B}_z + \omega^E_\perp}\Big]. \end{aligned} \tag{B.61}$$

Differences in the matrix elements for $\mathcal{N} = \pm 1$ states, such as due to the differences in g-factors for the Ω-doublet states (a consequence of $\mathcal{E}$-field induced mixing of the $H, J = 2$ state into the $H, J = 1$ state of interest) [BHJD09, Ham10], will cause small corrections to this result. Nevertheless, the key point remains, which is that the geometric phase (and more generally, the energy shifts to 2nd order in $\mathcal{E}_\perp, \mathcal{B}_\perp$ and all orders in the evolution frequency $\omega_\perp$) can be largely suppressed from appearing as an EDM-like systematic by comparing the Ω-doublets.

The above analytic calculations are useful for providing insight and estimates of

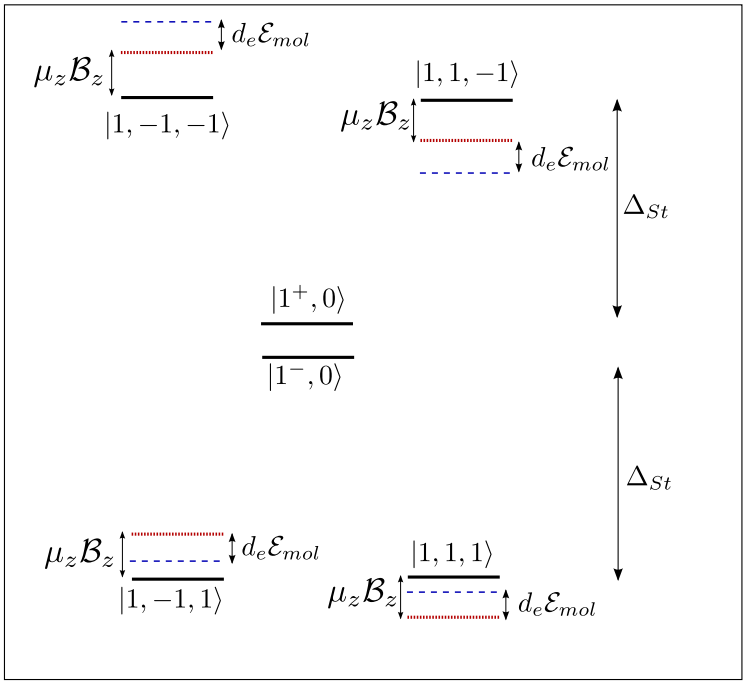

(a) eEDM energy shift, $d_e\mathcal{E}_{mol}$

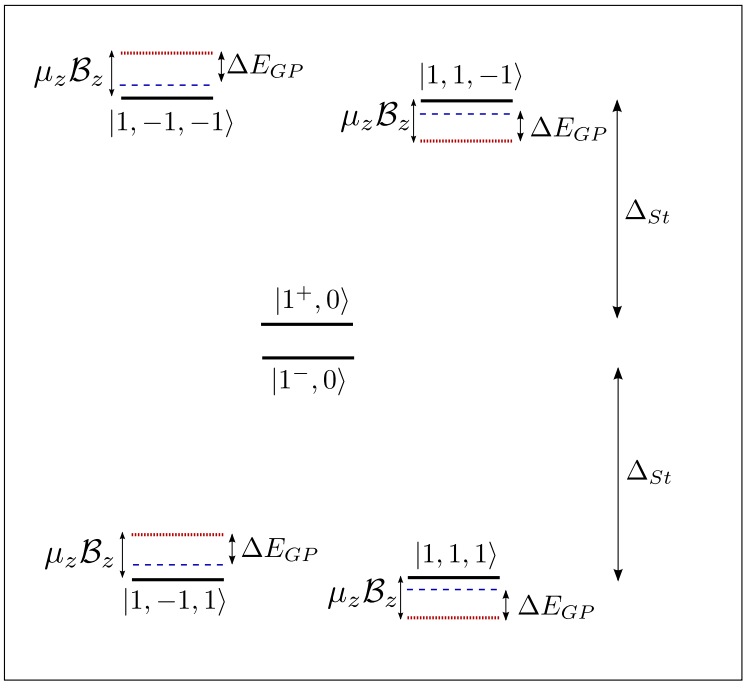

(b) Off-resonant energy shifts, ΔE_{GP}

Figure B.7: Energy shifts of the $H, J = 1$ state in $\mathcal{E}_z, \mathcal{B}_z$ fields. The $m_J = 0$ states are not perturbed (or only weakly polarized by mixing with $J = 2$ levels), and continue to be denoted by $|J^p, m_J\rangle$ labels. The $m_J = \pm 1$ states are shown in the strongly electrically polarized regime, and are labeled $|J, m_J, \mathcal{N} = m_J\Omega\rangle$. a) Energy shifts due to an eEDM. b) Energy shifts (that lead to geometric phases) due to $\mathcal{E}_\perp, \mathcal{B}_\perp$.

the size of the effects to expect, but when necessary, the eigenvalues of the full 16 x 16 Hamiltonian (6 levels in $J = 1$, 10 levels in $J = 2$) can be numerically calculated over the trajectory of the molecules through the known (or artificially distorted) $\mathcal{E}$- and $\mathcal{B}$-fields in the apparatus.

Summary

A number of simple examples have been worked out, where the geometric phase arises due to magnetic or electric fields whose direction changes over time. Identifying the geometric phase as the phase due to off-resonant energy shifts enables it to be calculated in every case without recourse to topology. Compared to the usual geometric approach, phase shifts due to fast evolution and/or non-cyclic paths in parameter space can be calculated in a straightforward way using energy shifts. Instead of tracking all the eigenstates as the Hamiltonian evolves along a path in its parameter space, the problem is reduced to a calculation of eigenvalues. This enables efficient numerical calculation of geometric phase effects in experimentally relevant situations, where the evolution of the fields experienced by atoms or molecules can be quite complicated, and where the assumptions of the geometric formulation (particularly, that of adiabatic evolution) are broken.

Bibliography

[AWM95] S. Appelt, G. Wackerle, and M. Mehring. Geometric phase in nonadiabatic figure-8 experiments. *Phys. Lett. A*, 204(3-4):210–216, 1995.

[BC03] John M. Brown and Alan Carrington. *Rotational spectroscopy of diatomic molecules*. Cambridge University Press, 2003.

[BD87] T. Bitter and D. Dubbers. Manifestation of Berry's topological phase in neutron spin rotation. *Phys. Rev. Lett.*, 59(3):251–254, 1987.

[BDS02] S. Y. Buhmann, V. A. Dzuba, and O. P. Sushkov. Enhancement of the electron electric dipole moment in Gd^{3+}. *Phys. Rev. A*, 66(4):042109, October 2002.

[Ber84] M. V. Berry. Quantal phase factors accompanying adiabatic changes. *Proc. Royal Soc. A*, 392:45–57, 1984.

[BHJD09] S. Bickman, P. Hamilton, Y. Jiang, and D. DeMille. Preparation and detection of states with simultaneous spin alignment and selectable molecular orientation in PbO. *Phys. Rev. A*, 80(2):023418, 2009.

[BKD08] Dmitry Budker, Derek F. J. Kimball, and David P. DeMille. *Atomic physics: an exploration through problems and solutions*. Oxford University Press, 2008.

[BSD11] J.F. Barry, E.S. Shuman, and D. DeMille. A Bright, Slow Cryogenic Molecular Beam Source for Free Radicals. *arXiv:1101.4229*, 2011.

[BVK+88] P. Balakrishna, B. P. Varma, T. S. Krishnan, T. R. R. Mohan, and P. Ramakrishnan. Low-temperature sintering of thoria. *J. Mat. Sci. Lett.*, 7:657–660, 1988.

[CD09] E. D. Commins and D. DeMille. *Lepton Dipole Moments*, chapter The electric dipole moment of the electron, pages 519–581. World Scientific, 2009.

[CJD07] Eugene D. Commins, J. David Jackson, and David P. DeMille. The electric dipole moment of the electron: An intuitive explanation for the evasion of Schiff's theorem. *Am. J. Phys.*, 75(6):532–536, 2007.

[Com91] Eugene D. Commins. Berry's geometric phase and motional fields. *Am. J. Phys.*, 59(12):1077–1080, 1991.

[Cra34] F. H. Crawford. Zeeman Effect in Diatomic Molecular Spectra. *Rev. Mod. Phys.*, 6(2):90, 1934.

[CS93] W. A. Campbell and J. J. Scialdone. Outgassing Data for Selecting Spacecraft Materials (Online). Technical report, Goddard Space Flight Center, 1993.

[CTGDR92] Claude Cohen-Tannoudji, Gilbert Grynberg, and Jacques Dupont-Roc. *Atom-photon interactions: Basic processes and applications*. Wiley Interscience, 1992.

[Dav76] A. S. Davydov. *Quantum Mechanics*. Pergamon, 1976.

[DBB+00] D. DeMille, F. Bay, S. Bickman, D. Kawall, D. Krause, S. E. Maxwell, and L. R. Hunter. Investigation of PbO as a system for measuring the electric dipole moment of the electron. *Phys. Rev. A*, 61(5):052507, April 2000.

[DDBT07] C. J. Dedman, R. G. Dall, L. J. Byron, and A. G. Truscott. Active cancellation of stray magnetic fields in a Bose-Einstein condensation experiment. *Rev. Sci. Inst.*, 78:024703, 2007.

[DK03] Michael Dine and Alexander Kusenko. Origin of the matter-antimatter asymmetry. *Rev. Mod. Phys.*, 76(1):1–30, December 2003.

[Dra06] G. W. F. Drake, editor. *Springer Handbook of Atomic, Molecular and Optical Physics*. Springer, 2006.

[EL84] G. Edvinsson and A. Lagerqvist. Rotational analysis of yellow and near infrared bands in ThO. *Physica Scripta*, 30(5):309–320, 1984.

[Far07] D. M. Farkas. *An Optical Reference and Frequency Comb for Improved Spectroscopy of Helium*. PhD thesis, Harvard University, 2007.

[FHLR05] Stefan Filipp, Yuji Hasegawa, Rudolf Loidl, and Helmut Rauch. Spatial non-cyclic geometric phase in neutron interferometry. *J. Res. Natl. Inst. Stand. Technol.*, 110:251–257, 2005.

[FSB03] Norval Fortson, Patrick Sandars, and Stephen Barr. The search for a permanent electric dipole moment. *Phys. Today*, 56:33–39, 2003.

[Fur81] J E Furse. Kinematic design of fine mechanisms in instruments. *J. Phys. E: Scientific Instruments*, 14(3):264, 1981.

[GHKH05] Vasiliy Goncharov, Jiande Han, Leonid A. Kaledin, and Michael C. Heaven. Ionization energy measurements and electronic spectra for ThO. *J. Chem. Phys.*, 122(20):204311, 2005.

[GHO+94] M. B. Gavela, P. Hernandez, J. Orloff, O. Pne, and C. Quimbay. Standard model CP-violation and baryon asymmetry (II). Finite temperature. *Nuclear Physics B*, 430(2):382 – 426, 1994.

[GR06] G. F. Giudice and A. Romanino. Electric dipole moments in split supersymmetry. *Phys. Lett. B*, 634(2-3):307–314, 2006.

[Gri05] David J Griffiths. *Introduction to quantum mechanics*. Benjamin Cummings, 2005.

[Gur11] Y. V. Gurevich. PhD thesis, Harvard University, 2011.

[Ham10] Paul Hamilton. *Preliminary results in the search for the electron electric dipole moment in lead oxide**. PhD thesis, Yale University, 2010.

[HH79] K. P. Huber and G. Herzberg. *Constants of Diatomic Molecules*. Van Nostrand Reinhold, 1979.

[HKS+11] J. J. Hudson, D. M. Kara, I. J. Smallman, B. E. Sauer, M. R. Tarbutt, and E. A. Hinds. Improved measurement of the shape of the electron. *Nature*, 473:493496, 2011.

[Hol89] B. R. Holstein. The adiabatic theorem and Berry's phase. *Am. J. Phys.*, 57(12):1079–1084, 1989.

[Hou01] Jon T. Hougen. The Calculation of Rotational Energy Levels and Rotational Line Intensities in Diatomic Molecules. *NBS Monograph 115*, 2001.

[HPG+11] Nicholas R. Hutzler, Maxwell Parsons, Yulia V. Gurevich, Paul W. Hess, Elizabeth Petrik, Ben Spaun, Amar C. Vutha, David DeMille, Gerald Gabrielse, and John M. Doyle. A cryogenic beam of refractory, chemically reactive molecules with expansion cooling. *arXiv:1101.4217*, 2011.

[IBB+93] W. M. Itano, J. C. Bergquist, J. J. Bollinger, J. M. Gilligan, D. J. Heinzen, F. L. Moore, M. G. Raizen, and D. J. Wineland. Quantum projection noise: Population fluctuations in two-level systems. *Phys. Rev. A*, 47(5):3554–3570, 1993.

[KBB+04] D. Kawall, F. Bay, S. Bickman, Y. Jiang, and D. DeMille. Precision Zeeman-Stark spectroscopy of the metastable $a(1)[^3\Sigma^+]$ state of PbO. *Phys. Rev. Lett.*, 92(13):133007, April 2004.

[KBC+65] D. Kleppner, H. C. Berg, S. B. Crampton, N. F. Ramsey, R. F. C. Vessot, H. E. Peters, and J. Vanier. Hydrogen-Maser Principles and Techniques. *Phys. Rev.*, 138(4A):A972–A983, May 1965.

[KD02] M. G. Kozlov and D. DeMille. Enhancement of the Electric Dipole Moment of the Electron in PbO. *Phys. Rev. Lett.*, 89(13):133001, September 2002.

[KDSP94] W. Kuchle, M. Dolg, H. Stoll, and H. Preuss. Energy-adjusted pseudopotentials for the actinides. Parameter sets and test calculations for thorium and thorium monoxide. *J. Chem. Phys.*, 100(10):7535–7542, 1994.

[KE94] M. G. Kozlov and V. F. Ezhov. Enhancement of the electric dipole moment of the electron in the YbF molecule. *Phys. Rev. A*, 49(6):4502–4507, June 1994.

[KL97] Iosif B. Khriplovich and Steve K. Lamoreaux. *CP-violation without strangeness : electric dipole moments of particles, atoms, and molecules*. Springer-Verlag, 1997.

[Lam99] S. K. Lamoreaux. Feeble magnetic fields generated by thermal charge fluctuations in extended metallic conductors: Implications for electric-dipole moment experiments. *Phys. Rev. A*, 60(2):1717–1720, August 1999.

[Lam02] S. K. Lamoreaux. Solid-state systems for the electron electric dipole moment and other fundamental measurements. *Phys. Rev. A*, 66(2):022109, August 2002.

[LBL+10] Aaron E. Leanhardt, John L. Bohn, Huanqian Loh, Patrick Maletinsky, Edmund R. Meyer, Laura C. Sinclair, Russell P. Stutz, and Eric A. Cornell. On measuring the electron electric dipole moment in trapped molecular ions. *arXiv:1008.2997v2 [physics.atom-ph]*, 2010.

[LG05] S. K. Lamoreaux and R. Golub. Detailed discussion of a linear electric field frequency shift induced in confined gases by a magnetic field gradient: Implications for neutron electric-dipole-moment experiments. *Phys. Rev. A*, 71(3):032104, 2005.

[LL81] L. D. Landau and E. M. Lifshitz. *Quantum Mechanics: Non-relativistic Theory*. Butterworth-Heinemann, 1981.

[LL87] L. D. Landau and E. M. Lifshitz. *Fluid Mechanics*. Butterworth-Heinemann;, 1987.

[LMP+09] J. Lee, E. R. Meyer, R. Paudel, J. L. Bohn, and A. E. Leanhardt. An electron electric dipole moment search in the X3Δ1 ground state of tungsten carbide molecules. *J. Mod. Opt.*, 56:2005–2012, October 2009.

[MB08] Edmund R. Meyer and John L. Bohn. Prospects for an electron electric-dipole moment search in metastable ThO and ThF[sup +]. *Phys. Rev. A*, 78(1):010502, 2008.

[MBD06] Edmund R. Meyer, John L. Bohn, and Michael P. Deskevich. Candidate molecular ions for an electron electric dipole moment experiment. *Phys. Rev. A*, 73(6):062108, 2006.

[Mey10] Edmund R. Meyer. *Structure and spectroscopy of candidates for an electron electric dipole moment experiment*. PhD thesis, University of Colorado, 2010.

[Mun05] Charles T. Munger. Magnetic Johnson noise constraints on electron electric dipole moment experiments. *Phys. Rev. A*, 72(1):012506, 2005.

[MWGP87] Christel M. Marian, Ulf Wahlgren, Odd Gropen, and Pekka Pyykko. Bonding and electronic structure in diatomic ThO: quasirelativistic effective core potential calculations. *J. Mol. Struct.*, 169:339, 1987.

[Nat09] H. S. Nataraj. *Electric Dipole Moment of the Electron and its Implications on Matter-Antimatter Asymmetry in the Universe*. PhD thesis, Mangalore University, 2009.

[OPRS05] Keith A. Olive, Maxim Pospelov, Adam Ritz, and Yudi Santoso. CP-odd phase correlations and electric dipole moments. *Phys. Rev. D.*, 72(7):075001, 2005.

[Pat71] R. A. Patten. Michelson Interferometer as a Remote Gauge. *Appl. Opt.*, 10(12):2717–2721, Dec 1971.

[PD07] David Patterson and John M. Doyle. Bright, guided molecular beam with hydrodynamic enhancement. *J. Chem. Phys.*, 126(15), 2007.

[PHS+04] J. M. Pendlebury, W. Heil, Yu. Sobolev, P. G. Harris, J. D. Richardson, R. J. Baskin, D. D. Doyle, P. Geltenbort, K. Green, M. G. D. van der Grinten, P. S. Iaydjiev, S. N. Ivanov, D. J. R. May, and K. F. Smith. Geometric-phase-induced false electric dipole moment signals for particles in traps. *Phys. Rev. A*, 70(3):032102, 2004.

[PNH02] Jozef Paulovic, Takahito Nakajima, and Kimihiko Hirao. Third-order Douglas–Kroll ab initio model potential for actinide elements. *J. Chem. Phys.*, 117:3597, 2002.

[PNH+03] Jozef Paulovic, Takahito Nakajima, Kimihiko Hirao, Roland Lindh, and Per Ake Malmqvist. Relativistic and correlated calculations on the ground and excited states of ThO. *J. Chem. Phys.*, 119(2):798–805, 2003.

[PR50] E. M. Purcell and N. F. Ramsey. On the possibility of electric dipole moments for elementary particles and nuclei. *Phys. Rev.*, 78(6):807, June 1950.

[PR09] M. Pospelov and A. Ritz. *Lepton Dipole Moments*, chapter Probing CP violation with electric dipole moments, pages 439–518. World Scientific, 2009.

[PS70] M. A. Player and P. G. H. Sandars. An experiment to search for an electric dipole moment in the 3P2 metastable state of xenon. *J. Phys. B*, 3(12):1620–1635, 1970.

[PS00] E. Paperno and I. Sasada. Magnetic circuit approach to magnetic shielding. *J. Magn. Soc. Japan*, 24:40–44, 2000.

[Pur84] E. M. Purcell. *Electricity and Magnetism (Berkeley Physics Course, Vol. 2)*. McGraw-Hill, 1984.

[Ram55] Norman F. Ramsey. Resonance transitions induced by perturbations at two or more different frequencies. *Phys. Rev.*, 100:1191, 1955.

[Ram85] Norman F. Ramsey. *Molecular beams*. Oxford University Press, 1985.

[RBB+06] N A Robertson, J R Blackwood, S Buchman, R L Byer, J Camp, D Gill, J Hanson, S Williams, and P Zhou. Kelvin probe measurements: investigations of the patch effect with applications to ST-7 and LISA. *Classical and Quantum Gravity*, 23(7):2665, 2006.

[RCSD02] B. C. Regan, Eugene D. Commins, Christian J. Schmidt, and David DeMille. New Limit on the Electron Electric Dipole Moment. *Phys. Rev. Lett.*, 88(7):071805, February 2002.

[RFG+08] M. Rand, J. Fuger, I. Grenthe, V. Neck, and D. Rai. *Chemical Thermodynamics of Thorium*. OECD, 2008.

[RKGL88] D. J. Richardson, A. I. Kilvington, K. Green, and S. K. Lamoreaux. Demonstration of Berry's Phase Using Stored Ultracold Neutrons. *Phys. Rev. Lett.*, 61(18):2030–2033, 1988.

[RM09] B. Lee Roberts and William J. Marciano, editors. *Lepton Dipole Moments*. World Scientific, December 2009.

[Sak64] J. J. Sakurai. *Invariance Principles and Elementary Particles*. Princeton, 1964.

[Sak67] A. D. Sakharov. Violation of CP invariance, asymmetry, and baryon asymmetry of the universe. *JETP Lett.*, 6:24, 1967.

[Sak85] J. J. Sakurai. *Modern Quantum Mechanics*. Benjamin Cummings, 1985.

[Sal58] E. E. Salpeter. Some Atomic Effects of an Electronic Electric Dipole Moment. *Phys. Rev.*, 112(5):1642–1648, December 1958.

[San65] P. G. H. Sandars. The electric dipole moment of an atom. *Phys. Lett.*, 14(3):194–196, 1965.

[San66] P.G.H. Sandars. Enhancement factor for the electric dipole moment of the valence electron in an alkali atom. *Physics Letters*, 22(3):290 – 291, 1966.

[San67] P. G. H. Sandars. Measurability of the Proton Electric Dipole Moment. *Phys. Rev. Lett.*, 19(24):1396–1398, December 1967.

[San68a] P G H Sandars. The electric-dipole moments of an atom I. Some general considerations. *Journal of Physics B: Atomic and Molecular Physics*, 1(3):499, 1968.

[San68b] P G H Sandars. The electric-dipole moments of an atom II. The contribution from an electric-dipole moment on the electron with particular reference to the hydrogen atom. *Journal of Physics B: Atomic and Molecular Physics*, 1(3):511, 1968.

[Sch63] L. I. Schiff. Measurability of Nuclear Electric Dipole Moments. *Phys. Rev.*, 132(5):2194–2200, Dec 1963.

[SPS87] T. J. Sumner, J. M. Pendlebury, and K. F. Smith. Conventional magnetic shielding. *J. Phys. D: Appl. Phys.*, 20:1095–1101, 1987.

[SR06] Neil E. Shafer-Ray. Possibility of 0- g -factor paramagnetic molecules for measurement of the electron's electric dipole moment. *Phys. Rev. A*, 73(3):034102, Mar 2006.

[SSM86] R. Simon, E. C. G. Sudarshan, and N. Mukunda. Gaussian-Maxwell beams. *J. Opt. Soc. Am. A*, 3(4):536–540, 1986.

[SSM87] R. Simon, E. C. G. Sudarshan, and N. Mukunda. Cross polarization in laser beams. *Appl. Opt.*, 26(9):1589–1593, 1987.

[Str38] John Strong. *Procedures in experimental physics*. Prentice-Hall, 1938.

[SZ74] F. Stepanov and B. I. Zhilinskii. When and Why Hunds Cases Arise. *J. Mol. Spectrosc.*, 52:277–286, 1974.

[THSH09] M. R. Tarbutt, J. J. Hudson, B. E. Sauer, and E. A. Hinds. Prospects for measuring the electric dipole moment of the electron using electrically trapped polar molecules. *Faraday Discuss.*, 142:37, 2009.

[VCG+10] A. C. Vutha, W. C. Campbell, Y. V. Gurevich, N. R. Hutzler, M. Parsons, D. Patterson, E. Petrik, B. Spaun, J. M. Doyle, G. Gabrielse, and D. DeMille. Search for the electric dipole moment of the electron with thorium monoxide. *J. Phys. B*, 43(7):074007, 2010.

[VD09] Amar Vutha and David DeMille. Geometric phases without geometry. *arXiv:0907.5116v2 [quant-ph]*, 2009.

[VSG+11] A. C. Vutha, B. Spaun, Y. V. Gurevich, N. R. Hutzler, E. Kirilov, J. M. Doyle, G. Gabrielse, and D. DeMille. Magnetic and electric dipole moments of the H 3 Delta 1 state in ThO. *arXiv:1107.2287 [physics.atom-ph]*, 2011.

[WFC03] D. S. Weiss, F. Fang, and J. Chen. Measuring the electric dipole moment of Cs and Rb in an optical lattice. *Bull. Am. Phys. Soc.*, APR03(J1.008), 2003.

[WM97] Yoshihiro Watanabe and Osamu Matsuoka. All-electron Dirac–Fock–Roothaan calculations for the ThO molecule. *J. Chem. Phys.*, 107(9):3738–3739, 1997.

[WS72] Tunis Wentink and Robert J. Spindler. The isoelectronic series ScF through ThO–I notes on the band spectra of TiO, HfO and ThO. *Journal of Quantitative Spectroscopy and Radiative Transfer*, 12(11):1569 – 1590, 1972.

[YoPDG06] W. M. Yao and others (Particle Data Group). Review of Particle Physics. *J. Phys. G*, 33(1):1–1232, 2006.